Title	The Study of Varying Weights in Rational Basis Functions in Isogeometric Large-Displacement Analysis of Beams
Author(s)	Duong, Nghi Huu
Degree Grantor	北海道大学
Degree Name	博士(工学)
Dissertation Number	甲第16344号
Issue Date	2025-03-25
DOI	https://doi.org/10.14943/doctoral.k16344
Doc URL	https://hdl.handle.net/2115/95023
Type	doctoral thesis
File Information	Nghi_Huu_Duong.pdf

The Study of Varying Weights in Rational Basis Functions in Isogeometric Large-Displacement Analysis of Beams

BY

Mr. NGHI HUU DUONG

A DISSERTATION SUBMITTED IN PARTIAL FULFILLMENT OF THE REQUIREMENTS FOR THE DEGREE OF DOCTOR OF PHILOSOPHY (ENGINEERING AND TECHNOLOGY)

SIRINDHORN INTERNATIONAL INSTITUTE OF TECHNOLOGY

THAMMASAT UNIVERSITY

AND

GRADUATE SCHOOL OF ENGINEERING

HOKKAIDO UNIVERSITY

ACADEMIC YEAR 2024

THAMMASAT UNIVERSITY
SIRINDHORN INTERNATIONAL INSTITUTE OF TECHNOLOGY
AND
HOKKAIDO UNIVERSITY, GRADUATE SCHOOL OF ENGINEERING

DISSERTATION

BY

MR. NGHI HUU DUONG

ENTITLED

The Study of Varying Weights in Rational Basis Functions in Isogeometric Large-Displacement Analysis of Beams

was approved as partial fulfillment of the requirements for
the degree of Doctor of Philosophy (Engineering and Technology)

on January 9, 2025

DISSERTATION COMMITTEE AT SIRINDHORN INTERNATIONAL INSTITUTE OF TECHNOLOGY, THAMMASAT UNIVERSITY

Chairperson

(Professor Teerapong Senjuntichai, Ph.D.)

Member and Advisor

(Professor Pruettha Nanakorn, D.Eng.)

Member

(Professor Takashi Matsumoto, Ph.D.)

Member

(Associate Professor Kriengsak Panuwatwanich, Ph.D.)

Member

(Associate Professor Ganchai Tanapornraweekit, Ph.D.)

Director

(Professor Pruettha Nanakorn, D.Eng.)

DISSERTATION COMMITTEE AT GRADUATE SCHOOL OF ENGINEERING, HOKKAIDO UNIVERSITY

Member and Advisor

(Professor Takashi Matsumoto, Ph.D.)

Member

(Professor Pruettha Nanakorn, D.Eng.)

Member

(Professor Yasunori Miyamori, Ph.D.)

Member

(Professor Motohiro Sato, Ph.D.

Member

(Associate Professor Akira Furukawa, Ph.D.)

Thesis Title	The Study of Varying Weights in Rational Basis Functions in Isogeometric Large-Displacement Analysis of Beams
Author	Mr. Nghi Huu Duong
Degrees	Doctor of Philosophy (Engineering and Technology)
Faculties/Universities	Sirindhorn International Institute of Technology/ Thammasat University and Graduate School of Engineering/Hokkaido University
Dissertation Advisors	Professor Pruettha Nanakorn, D.Eng. Professor Takashi Matsumoto, Ph.D.
Dissertation Co-Advisor	–
Academic Year	2024

ABSTRACT

This study presents novel planar curved Euler-Bernoulli and Timoshenko-Ehrenfest beam elements for analyzing beam structures subjected to large displacements but small strains. As the total Lagrangian description is employed, the initial configuration is the reference for the kinematics. By assuming small strains and thin beams, higher-order terms of the Green-Lagrange strains are discarded, leading to the simplification of formulations. The equilibrium is then stated through the principle of virtual works. Subsequently, the proposed elements are derived using the isogeometric analysis approach. Cubic non-uniform rational B-spline (NURBS) representations are employed for the Euler-Bernoulli beam element, while quadratic and cubic NURBS representations are used for the Timoshenko-Ehrenfest beam elements. However, in contrast to the traditional isogeometric analysis concept, the isoparameterization between the reference geometry and kinematic unknowns is relaxed by treating specific weights in the NURBS basis functions as degrees of freedom (DOFs). The obtained equation systems are inherently nonlinear in terms of

DOFs. As this study employs the Newton-Raphson method to solve these nonlinear-equation systems, linearization is required. For this purpose, the symbolic computing capability of MATLAB is used.

The efficiency of the proposed elements and the superiority of the proposed elements over those with constant weights are demonstrated by solving several beam problems. The obtained solutions underscore the efficiency of the proposed elements in analyzing beam structures experiencing large displacements with complex behaviors, such as buckling and snap responses. Additionally, the varying-weight elements consistently outperform the constant-weight counterparts in providing highly accurate solutions. In this regard, the constant-weight elements always require significantly more DOFs than the varying-weight counterparts. The accuracy superiority of the varying-weight elements becomes more apparent in extreme regions such as regions of buckling points, limit points, or substantial displacements.

For Euler-Bernoulli beams, the superiority of the varying-weight element is also evident in terms of accurate recovery of strain measures. While the cubic varying-weight element exhibits no locking phenomena, the cubic constant-weight element slightly shows locking effects in some problems. For Timoshenko-Ehrenfest beams, the varying-weight elements effectively mitigate locking effects, confirming their reliability for solving thin-beam problems. Furthermore, while exhibiting the locking-free characteristic, varying-weight elements yield comparable accuracy to that of the locking-free $\overline{\mathrm{B}}$ elements in a literature, but demand significantly less computational effort. This solves the trade-off challenge of these $\overline{\mathrm{B}}$ elements, between mitigating locking effects and computational efficiency.

Keywords: Geometrically nonlinear analysis, large displacements, small strains, non-uniform rational B-spline, Euler-Bernoulli beams, Timoshenko-Ehrenfest beams, constant-weight elements, varying-weight elements.

ACKNOWLEDGMENTS

A journey is filled with pride and gratitude. I am deeply grateful to the Collaborative Education Program (CEP) of AUN/SEED-Net, Sirindhorn International Institute of Technology (SIIT) at Thammasat University, and Hokkaido University for providing me with incredible opportunities to pursue my doctoral studies.

Being affiliated with SIIT and Hokkaido University was such a tremendous honor. These world-class educational environments not only enriched my academic pursuits but also fostered my personal growth in a diverse setting, particularly amidst the challenges posed by the COVID-19 pandemic. Therein, the advisories of Professor Pruettha Nanakorn at SIIT and Professor Matsumoto Takashi at Hokkaido University were indispensable. The guidance, though strict, consistently pushed me to strive for excellence. The knowledge and experience acquired are undoubtedly treasures that will serve as key fundamentals for my future.

Additionally, I would like to express my gratitude to Associate Professor Kriengsak Panuwatwanich for his exceptional coordination of the CEP program, as well as his timely assistance. I am also thankful to Professor Teerapong Senjuntichai, Associate Professor Ganchai Tanapornraweekit, and Associate Professor Kriengsak Panuwatwanich for their contributions as committee members at SIIT, and to Professor Motohiro Sato, Professor Yasunori Miyamori and Associate Professor Akira Furukawa for their contributions as committee members at Hokkaido University. Furthermore, I truly appreciate the unwavering support and collaboration of Dr. Duy Vo. His professional contributions and shared knowledge are always helpful and valuable. Moreover, I cannot forget my lab mates at both SIIT and Hokkaido University, as well as the CEP student team for accompanying me through the challenging times. Last, but certainly not least, is my appreciation to all the professors, staffs, and friends who were there for me.

Each factor plays an irreplaceable role, not only in my academic path but also in my whole life journey. I am sincerely grateful for each and every contribution.

Warm regards,

Mr. Nghi Huu Duong

TABLE OF CONTENTS

LIST OF TABLES

Table Page

LIST OF FIGURES

LIST OF SYMBOLS/ABBREVIATIONS

Symbols/Abbreviations	Terms
AUN/SEED-Net	ASEAN University Network/Southeast Asia Engineering Education Development Network
CEP	Collaborative Education Program
TU	Thammasat University
SIIT	Sirindhorn International Institute of Technology
HU	Hokkaido University
FE	Finite Element
FEM	Finite Element Method
FEA	Finite Element Analysis
IGA	Isogeometric Analysis
CAD	Computer-Aided Design
NURBS	Non-uniform Rational B-spline
GNURBS	Generalized Non-uniform Rational B-spline
2D	Two-Dimensional
3D	Three-Dimensional
DOFs	Degrees of freedom

CHAPTER 1
INTRODUCTION

1.1 General

Numerical analysis of beam structures has a long and rich history (Timoshenko, 1958). However, ongoing progress continues today, driven by the demands of emerging unconventional modern beam structures (Cesnik & Shin, 2001; Hodges, 2006; Júnior, Cardozo, Júnior & Neto, 2019; Sabale & Gopal, 2019). These modern structures often feature complex geometries, and in typical applications, may undergo large displacements. When performing numerical analysis, an appropriate beam model and numerical method need to be selected. Among various beam models, the Euler-Bernoulli and Timoshenko-Ehrenfest beam models are common choices. In the Euler-Bernoulli beam model, a plane cross-section initially orthogonal to the beam axis is assumed to remain plane and orthogonal to the beam axis during deformation. In contrast, in the Timoshenko-Ehrenfest beam model, a plane cross-section initially orthogonal to the beam axis is assumed to remain plane but not necessarily orthogonal to the beam axis during deformation. For beams experiencing large displacements, these kinematic assumptions in the Euler-Bernoulli or Timoshenko-Ehrenfest beam model generally remain applicable. However, formulations designed for small displacements must be revised to accommodate large displacements and potentially large strains (Reissner, 1972; Simo & Vu-Quoc, 1986, 1986). Regarding numerical methods, finite element methods (FEMs) are widely used owing to their versatility.

In conventional FEM, interpolations of kinematic unknowns are mainly constructed using polynomials. With the isoparametric concept, a finite element model's reference geometry and kinematic unknowns are interpolated using the same set of interpolation functions. This concept, therefore, necessitates the use of polynomials to interpolate the model's reference geometry, resulting in the mesh used for analysis. Unfortunately, objects with complex reference geometries often require fine meshes for accurate analysis, making mesh generation both costly and challenging, especially since, in practice, these geometries are not initially created using polynomials. To address this issue, isogeometric analysis (IGA) (Hughes, Cottrell & Bazilevs, 2005) was introduced.

In engineering modeling, the geometries of objects are mostly built using computer-aided design (CAD) programs, in which CAD basis functions are used to model the geometry. The IGA concept argues that CAD basis functions (Hughes, Cottrell & Bazilevs, 2005; Li & Sederberg, 2019; Piegl & Tiller, 1996; Sederberg, Zheng, Bakenov & Nasri, 2003; Warren & Weimer, 2001) can be directly and effectively used in analysis instead of polynomials. This elegant approach lessens the effort required for mesh generation, allowing a complex geometrical model to be represented in analysis unaltered, regardless of mesh density. Furthermore, the quality of interpolations is enhanced due to the high continuity of CAD basis functions.

Analytical proofs of the stability of the IGA approach in the context of mesh refinements, along with pertinent numerical investigations, are available (Bazilevs, Beirao da Veiga, Cottrell, Hughes & Sangalli, 2006; Da Veiga, Buffa, Sangalli & Vázquez, 2014; Hughes, Cottrell & Bazilevs, 2005). The IGA approach also passes standard patch tests (Hughes, Cottrell & Bazilevs, 2005). The advantages of the IGA approach for analysis of beams have also been confirmed (Bauer, Breitenberger, Philipp, Wüchner & Bletzinger, 2016; Bauer, Wüchner & Bletzinger, 2020; Borković, Kovačević, Radenković, Milovanović & Guzijan-Dilber, 2018; Borković, Kovačević, Radenković, Milovanović & Majstorović, 2019; Borković, Marussig & Radenković, 2022, 2022; Choi & Cho, 2019, 2020; Choi, Kang, Oh & Cho, 2019; Choi, Kim, Koo & Cho, 2021; Choi, Sauer & Klinkel, 2021; Chorn, Vo & Nanakorn, 2021; Greco, 2020; Greco & Cuomo, 2013, 2014; Greco, Cuomo, Contrafatto & Gazzo, 2017; Greco, Scrofani & Cuomo, 2021; Magisano, Leonetti & Garcea, 2021; Magisano, Leonetti, Madeo & Garcea, 2020; Marino, 2016, 2017; Radenković & Borković, 2018; Vo, Borković, Nanakorn & Bui, 2020; Vo, Li, Nanakorn & Bui, 2021; Vo & Nanakorn, 2019; Vo & Nanakorn, 2020, 2020; Vo, Nanakorn & Bui, 2019, 2020, 2021; Weeger, Yeung & Dunn, 2017, 2018).

1.2 Problem statement

Although various CAD basis functions are available, non-uniform rational B-spline (NURBS) basis functions (Piegl & Tiller, 1996) are widely used in IGA. In structural shape optimization employing NURBS basis functions, it has been observed that incorporating the weights in these basis functions as design variables significantly enhances the flexibility and accuracy of solutions (Fußeder, Simeon & Vuong, 2015; Nagy, Abdalla & Gürdal, 2010, 2010, 2011; Nagy, IJsselmuiden & Abdalla, 2013; Qian, 2010; Wall, Frenzel & Cyron, 2008). IGA formulations based on the isoparametric concept require the same basis functions for both the reference geometry and the interpolation of kinematic unknowns. Consequently, the weights in these basis functions are typically kept constant, optimized for the most accurate representation of the reference geometry.

In geometrically nonlinear analysis, large deformations of domains can occur, leading to significant shape differences between the initial and deformed configurations. As a result, a set of weights that is optimal for representing an initial domain may not be suitable for representing its deformed configuration. This issue is illustrated by the deformation of a cantilever beam subjected to an end moment in Figure 1.1a. Under a specific applied moment, the beam is bent into a semicircular shape. The initial and deformed beam axes can be exactly represented using cubic NURBS basis functions. However, the exact representations of the initial and deformed beam axes require different sets of weights in their NURBS basis functions, as indicated by the bracketed numbers in Figure 1.1a. In other words, the initial and deformed beam axes can be described exactly by using different basis functions, as shown in Figure 1.1b-c. This observation in geometrically nonlinear analysis suggests relaxing the isoparametric concept by treating weights in CAD basis functions as degrees of freedom (DOFs). Given the superior properties reported in shape optimization, this relaxation is expected to enhance the effectiveness and efficiency of IGA.

As various real-life beam structures are designed to undergo significant displacements during normal usage, analyzing these structures can effectively highlight the advantages of novel methods over traditional approaches. In this study, novel planar IGA curved Euler-Bernoulli and Timoshenko-Ehrenfest beam elements for large-displacement and small-strain analyses are introduced. The kinematic approximations are achieved using NURBS-based representations. Additionally, the isoparametric concept is relaxed by treating certain weights in NURBS basis functions as DOFs. This varying-weight concept allows for enhanced accuracy in approximating deformed geometries, thereby improving overall performance. The objectives and scope of this study are outlined below.

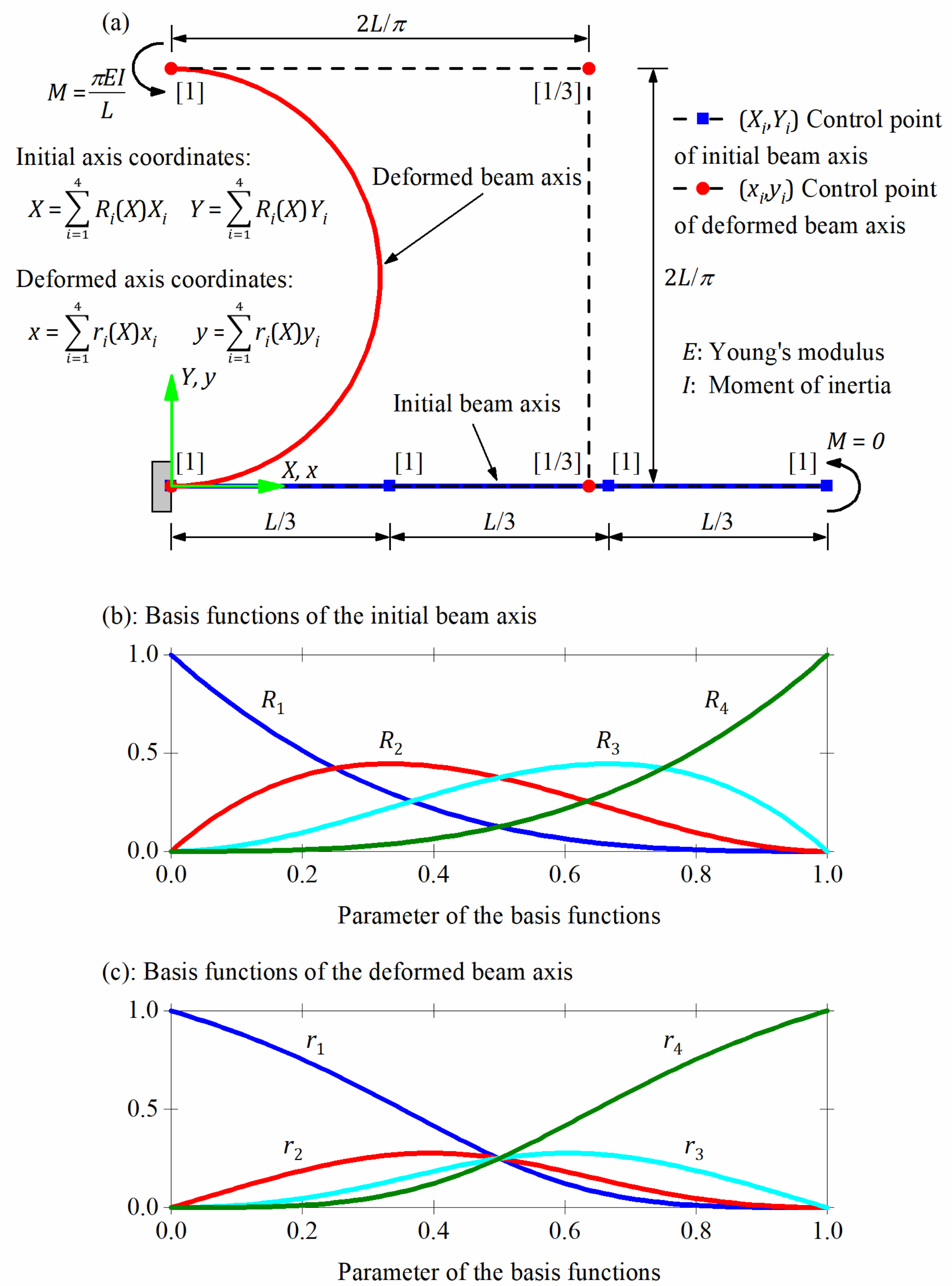

Figure 1.1 Pure bending of a cantilever beam.

1.3 The objectives of the study

The objectives of this study are as follows:

- To develop effective isogeometric finite element formulations for analyzing two-dimensional (2D) curved beams subjected to large displacements and small strains using NURBS.
- To investigate the impact of varying weights in rational basis functions on the performance of isogeometric beam analysis, specifically in terms of accuracy, convergence with respect to the number of DOFs, strain recovery, and the mitigation of locking phenomena.

1.4 The scope of the study

The scope of this study is as follows:

- Only static problems are considered.
- Only linear elastic isotropic materials are considered.

CHAPTER 2
REVIEW OF LITERATURE

In analysis of large displacements, there are three popular kinematic descriptions, i.e., total Lagrangian formulation (Chorn, Vo & Nanakorn, 2021; Pai, Anderson & Wheater, 2000), updated Lagrangian formulation (Bergel & Li, 2016; Noguchi & Hisada, 1995; Ten Thije, Akkerman & Huétink, 2007), and corotational formulation (Elkaranshawy, Elerian & Hussien, 2018; Urthaler & Reddy, 2005). Each description offers a distinct perspective on modeling. The total Lagrangian approach relies on integrations based on the initial configuration, leading to a fixed reference throughout the analysis. In contrast, the updated Lagrangian approach employs the latest configuration as the reference, enabling adaptive responses to evolving states. The corotational approach differs from the two Lagrangian formulations by decomposing displacements into two fundamental components, i.e., one from pure deformation and one from rigid body motion. This distinction facilitates a nuanced understanding of structural behavior, particularly when the relations between deformations and rigid body motions are complex.

IGA (Cottrell, Hughes & Bazilevs, 2009; Hughes, Cottrell & Bazilevs, 2005; Nguyen, Anitescu, Bordas & Rabczuk, 2015) emerged from the concept of integrating CAD utilities into finite element analysis (FEA). The use of CAD interpolations in IGA enables highly accurate representations of geometries and displacements, significantly enhancing the accuracy of numerical results (Han, Ma & Huang, 2008; Hartley & Judd, 1980; Hongsen, 2020; Kacprzyk & Ostapska-Łuczkowska, 2014; Li & Sederberg, 2019; Lian, Kerfriden & Bordas, 2017; Thomas, Engvall, Schmidt, Tew & Scott, 2022; Voruganti & Gondegaon, 2016). Consequently, IGA has been applied to various problems in computational mechanics (Bazilevs, Beirao da Veiga, Cottrell, Hughes & Sangalli, 2006; Hughes, Cottrell & Bazilevs, 2005), including those related to beam structures (Bauer, Breitenberger, Philipp, Wüchner & Bletzinger, 2016; Bauer, Wüchner & Bletzinger, 2020; Dimas & Briassoulis, 1999; Jočković, 2021; Vo, Borković, Nanakorn & Bui, 2020; Vo, Duong, Rungamornrat & Nanakorn, 2022; Vo, Li, Nanakorn & Bui, 2021; Vo & Nanakorn, 2020, 2020; Vo, Nanakorn & Bui, 2020, 2020, 2021; Vo, Nanakorn, Bui & Rungamornrat, 2022). Various CAD splines can be employed in IGA, such as U-splines, T-splines, S-splines, B-splines, and Bézier curves (Dimitri et al., 2014; Han, Ma & Huang, 2008; Hartley & Judd, 1980; Li & Sederberg, 2019; Lian, Kerfriden & Bordas, 2017; Prautzsch, Boehm & Paluszny, 2002; Ren, Shou & Lin, 2022; Sederberg, Zheng, Bakenov & Nasri, 2003; Thomas, Engvall, Schmidt, Tew & Scott, 2022). Additionally, rational forms of these CAD splines are favored due to their capability to capture complex and arbitrary shapes such as conic sections (Farin, 1992; Kim & Kang, 2011). Among these CAD interpolations, NURBS functions have gained popularity (Rogers, 2001). The works of Piegl (1991), Piegl and Tiller (1996), and Dimas and Briassoulis (1999) provide comprehensive overviews of NURBS, covering basic formulations and properties such as non-negativity, partition of unity, local support, differentiability. Moreover, each of these works presents specific applications and insights derived from their investigations into NURBS.

Typically, weights employed in NURBS basis functions are optimized to best represent the considered geometry. For instance, in the studies of Ma and Kruth (1998) and Carlson (2009), weights in NURBS basis functions are adjusted to fit curves and surfaces in reverse engineering. Meanwhile, in the study of Zhang, Zhu and Guo (2017), weights are manipulated to define the regular control surface for NURBS surfaces. This study elucidates the geometric meaning of weights and states that a regular control surface represents the limit of a NURBS surface when all control points are fixed but their weights approach infinity. Additionally, in shape optimization using NURBS basis functions, the flexibility and accuracy of solutions are significantly improved by including weights as design variables (Fußeder, Simeon & Vuong, 2015; Nagy, Abdalla & Gürdal, 2010, 2010, 2011; Nagy, IJsselmuiden & Abdalla, 2013; Qian, 2010; Wall, Frenzel & Cyron, 2008). Furthermore, an extended form of NURBS, known as generalized non-uniform rational B-splines (GNURBS), introduced by Taheri, Abolghasemi and Suresh (2020), uses different sets of weights for different coordinates in the employed coordinate system. As GNURBS is shown to be a disguised form of higher-order classic NURBS, it inherits all properties of NURBS that ensures a strong theoretical foundation. GNURBS offers better approximations than traditional NURBS for both smooth and rapidly varying fields. To illustrate the behavior of GNURBS compared to NURBS, a MATLAB toolbox called GNURBS Lab can be used. Building on this concept, Taheri and Suresh (2020) applied GNURBS to devise an adaptive w-refinement technique, where weights are decoupled for the geometry and solution space. Weights in the solution space are treated as design variables, enriching the solution space while preserving the underlying geometry and its parameterization. This technique achieves convergence rates that are one order higher than conventional IGA in smooth problems, and significantly improves the solution accuracy in problems with sharply varying solutions. Moreover, Taheri and Suresh (2022) extended the concept to bivariate parametric surfaces, improving the approximation of certain classes of surfaces, such as helicoids, revolved surfaces, and minimal surfaces. A MATLAB toolbox called GNURBS3D-Lab is available for illustrating the behavior and properties of GNURBS surfaces compared to classic NURBS surfaces.

Beams, the focal case studies of this research, have been extensively investigated, with their theories well-established and documented in various sources. Notably, Euler-Bernoulli and Timoshenko-Ehrenfest beams are the two most recognized models (Bauchau & Craig, 2009; Biondi & Caddemi, 2007; Davis, Henshell & Warburton, 1972; Elishakoff, 2020; Hutchinson, 2001; Kopmaz & Gündoğdu, 2003; Labuschagne, van Rensburg & Van der Merwe, 2009; Thomas, Wilson & Wilson, 1973; Wang, 1995). The primary distinction between these two beam models is that Timoshenko-Ehrenfest beams account for shear effects, while Euler-Bernoulli beams do not. During deformation, a plane cross-section initially orthogonal to the beam axis is assumed to remain plane and orthogonal to the beam axis in Euler-Bernoulli beams, while in Timoshenko-Ehrenfest beams, it is assumed to remain plane but not necessarily orthogonal to the beam axis. In practice, many beam structures are designed to be used under significant displacements during normal usage, necessitating reliable analysis methods to ensure accurate designs. As a result, various beam elements, from straight to curved, have been developed to meet specific demands and scenarios. Formulating beam elements requires a thorough understanding of these beam theories, along with a solid foundation in calculus (Lebedev, Cloud & Eremeyev, 2010), nonlinear continuum mechanics of solids (Basar & Weichert, 2000), applied mechanics (Reddy, 2017), and nonlinear FEA in structural mechanics (Rust, 2015).

In the context of straight beam elements, derivations are typically performed within Cartesian coordinate systems (Caillerie, Kotronis & Cybulski, 2015; Chad E &

Alex J, 2010; Irschik & Gerstmayr, 2009; Nanakorn & Vu, 2006; Vo, Duong, Rungamornrat & Nanakorn, 2022). In the study by Simo (1985), a clear and concise deformation map for three-dimensional (3D) geometrically nonlinear beams was introduced by incorporating a rotation tensor to represent cross-sectional finite rotation, offering a versatile approach applicable to both Euler-Bernoulli and Timoshenko-Ehrenfest beams. Building on this, Auricchio, Carotenuto and Reali (2008) highlighted the intrinsic characteristics of this 3D beam model by applying the small-strain assumption, which neglects higher-order terms of the Green-Lagrange strains. This approach simplifies the model equations, making them suitable for finite deformations with small strains. Additionally, Nanakorn and Vu (2006) developed a 2D straight Euler-Bernoulli beam element, designed for large-displacement and small-strain problems. Their model incorporates both the cross-sectional rotation tensor and the small-strain assumption, truncating higher-order terms of Green-Lagrange strains to yield simpler formulations. Furthermore, Chorn, Vo and Nanakorn (2021) effectively applied these concepts to develop 2D IGA straight Timoshenko-Ehrenfest beams using B-spline approximations.

Nonetheless, many beam structures designed for large displacements are not straight. Additionally, regardless of their initial configurations, the deformations always involve curved configurations. Accurately representing these initially curved beams and their deformed states requires a greater number of straight beam elements, making the computations expensive. As a result, using curved beam elements, which are derived with curved configurations from the outset, is preferable as it can reduce the number of required elements. Moreover, unlike straight beam elements, curved beam elements are commonly formulated in curvilinear coordinate systems (Auricchio, Carotenuto & Reali, 2008; Thompson, 1982; Vo & Nanakorn, 2020, 2020). Using curvilinear coordinate systems eliminates the need for coordinate transformations between local and global coordinates, simplifying implementation and reducing computational cost. In the studies by Vo and Nanakorn (2020, 2020), planar NURBS-based curved Euler-Bernoulli and Timoshenko-Ehrenfest beam elements are introduced for analyses of thin and curved beam structures, undergoing large displacements and finite strains. The formulations are developed within curvilinear coordinate systems, consisting of contravariant and covariant coordinate systems. The Green-Lagrange strain tensor is expressed in the contravariant system, while its energy conjugate, the second Polia-Kirchoff stress tensor, is written in the covariant system. These elements demonstrate high accuracy and convergence with increasing DOFs. Additionally, Vo, Nanakorn and Bui (2020, 2021) extended their studies to build 3D NURBS-based curved Euler-Bernoulli and Timoshenko-Ehrenfest beams.

As previously mentioned, weights employed in NURBS basis functions are typically optimized to best represent the geometry under consideration. In most IGA studies, these weights are optimized for the initial configurations, and remain unchanged throughout deformation. However, with large displacements, deformed configurations can deviate significantly from the initial state. Using fixed weights throughout the deformation can obviously reduce performance. To fully leverage the advantages of NURBS basis functions, weights should be varied to better adapt to deformed configurations. Applying this concept to IGA beams, Vo, Duong, Rungamornrat and Nanakorn (2022) treated weights in rational cubic Bézier basis functions as additional DOFs in their 2D IGA Euler-Bernoulli beam element. Their findings show that the presented element with varying weights outperforms the fixed-weight element in terms of solution accuracy and convergences with increasing DOFs. However, despite the clear reasoning for using varying weights during deformation, the application of this concept in IGA remains notably limited.

The success of beam elements in simulating flexible structures largely depends on addressing locking phenomena (Belytschko, Liu, Moran & Elkhodary, 2014; Hughes, 2012), i.e., membrane and shear locking. In conventional FEM, several techniques have been devised to address these locking problems. Examples include increasing the order of interpolations (Ashwell & Gallagher, 1976; Meck, 1980), using different interpolations for different kinematic unknowns (Babu & Prathap, 1986; Babu, Subramanian & Prathap, 1987; Ishaquddin, Raveendranath & Reddy, 2012, 2013), reduced and selective integration techniques (Noor & Peters, 1981; Prathap, 1985; Prathap & Bhashyam, 1982; Prathap & Naganarayana, 1990; Stolarski & Belytschko, 1982), mixed methods (Aköz, Omurtag & Doğruoğlu, 1991; Benlemlih & El Ferricha, 2002; Doğruoğlu & Kömürcü, 2019; Kim & Kim, 1998; Nukala & White, 2004), assumed natural strain and $\overline{\mathrm{B}}$-projection methods (Choit & Lim, 1995; Hughes, 1980; Karamanlidis & Jasti, 1987; Kim, 2010; Simo & Hughes, 1986), and discrete strain gap methods (Bletzinger, Bischoff & Ramm, 2000; Koschnick, Bischoff, Camprubí & Bletzinger, 2005). However, implementing these strategies often increases computational costs and can introduce numerical instabilities, such as hourglass modes in reduced and selective integration techniques (Flanagan & Belytschko, 1981). As a result, there is a continuous demand for intrinsically locking-free beam elements (Kiendl, Auricchio, Hughes & Reali, 2015; Kiendl, Auricchio & Reali, 2018). Unfortunately, locking effects are not automatically eliminated with NURBS-based discretization, and some strategies of FEM have been extended to the IGA approach. Examples include increasing the order of interpolations (Bouclier, Elguedj & Combescure, 2012; Vo & Nanakorn, 2020; Vo, Nanakorn & Bui, 2020), reduced and selective integration techniques (Adam, Bouabdallah, Zarroug & Maitournam, 2014; Bouclier, Elguedj & Combescure, 2012), assumed natural strain and $\overline{\mathrm{B}}$-projection methods (Bouclier, Elguedj & Combescure, 2012; Greco, Cuomo, Contrafatto & Gazzo, 2017; Hu, Hu & Xia, 2016), and discrete strain gap methods (Echter & Bischoff, 2010). While achieve varying degrees of success, concerns about generalization and cost efficiency remain.

The significance of computer implementation cannot be overstated, as computer science is one of the three fundamental pillars of computational mechanics, alongside mathematics and mechanics. Various programming languages are available for computer implementation. In this study, MATLAB (Higham & Higham, 2016; Routh, 2016) is employed due to its robust graphical capabilities and symbolic engine. Additionally, a range of solution techniques (Torkamani & Sonmez, 2008), including Linear Incremental, Incremental-Iterative, Newton-Raphson, Displacement Control, and Generalized Displacement Control methods, can be used to solve nonlinear finite element equation systems.

CHAPTER 3

PLANAR NON-UNIFORM RATIONAL B-SPLINE CURVES

IGA is a computational approach that integrates FEA and CAD tools to produce highly accurate models. In the IGA framework, various CAD splines can be employed, including Bézier functions, B-splines, T-splines, U-splines, and S-splines. Rational splines are also favored, with non-uniform rational B-splines (NURBS) being prevalent. In this study, planar NURBS representations are employed.

Generally, a planar NURBS curve can be expressed as (Hughes, Cottrell & Bazilevs, 2005; Piegl & Tiller, 1996; Prautzsch, Boehm & Paluszny, 2002)

$$\mathbf{C}(\xi) = \sum_{i=1}^{n} r_{i,p}(\xi)\mathbf{c}_i \tag{3.1}$$

where n is the number of control points and $\mathbf{c}_i \in \mathbb{R}^2$ represents the i-th control point. Additionally, $r_{i,p}(\xi)$ is a NURBS basis function expressed in terms of a parametric variable ξ as

$$r_{i,p}(\xi) = \frac{N_{i,p}(\xi)w_i}{\sum_{j=1}^{n} N_{j,p}(\xi)w_j} \tag{3.2}$$

where $N_{i,p}(\xi)$ denotes a B-spline basis function defined over a knot vector $\Xi = \{\xi_1, \xi_2, \dots, \xi_{n+p+1}\}$, with $\xi_i \leq \xi_{i+1}$ representing a knot value and p indicating the degree of the basis function. Moreover, w_i is a non-negative weight. The term "non-uniform" in NURBS refers to the flexible distribution of knot values, meaning that the spacing between adjacent knot values can vary.

In this study, cubic NURBS representations are employed for Euler-Bernoulli beams, while quadratic and cubic NURBS representations are used for Timoshenko-Ehrenfest beams. The parametric variable ξ is set in the range from 0 to 1, i.e., $\xi \in [0, 1]$.

For quadratic NURBS ($p = 2$), the knot vector $\Xi_{\mathrm{q}} = \{0, 0, 0, 1, 1, 1\}$ is used. In this case, there are three control points ($n = 3$) and three quadratic B-spline basis functions, explicitly defined as

$$N_{1,2}(\xi) = (1 - \xi)^2 \qquad N_{2,2}(\xi) = 2\xi(1 - \xi) \qquad N_{3,2}(\xi) = \xi^2 \,. \tag{3.3}$$

For cubic NURBS ($p = 3$), the knot vector $\Xi_{\mathrm{c}} = \{0, 0, 0, 0, 1, 1, 1, 1\}$ is employed. There are four control points ($n = 4$) and four cubic B-spline basis functions, i.e.,

$$N_{1,3}(\xi) = (1 - \xi)^3 \qquad N_{2,3}(\xi) = 3\xi(1 - \xi)^2 \tag{3.4}$$

$$N_{3,3}(\xi) = 3\xi^2(1 - \xi) \qquad N_{4,3}(\xi) = \xi^3 \,. \tag{3.5}$$

Illustrations of these quadratic and cubic B-spline basis functions are shown in Figure 3.1a and Figure 3.2a, respectively. For demonstration, quadratic NURBS basis functions are constructed using these quadratic B-spline basis functions with $w_1 = 1$, $w_2 = 2$, $w_3 = 1$, as shown in Figure 3.1a. Meanwhile, cubic NURBS basis functions are constructed using these cubic B-spline basis functions with $w_1 = 1$, $w_2 = 4$, $w_3 = 3$, and $w_4 = 1$, as shown in Figure 3.2b. Note that, if uniform weights are used, NURBS basis functions transform into B-spline basis functions, making B-spline basis functions special cases of NURBS basis functions.

In Figure 3.1b, two different quadratic NURBS curves with the same three control points are shown. Similarly, two different cubic NURBS curves with the same four control points are shown in Figure 3.2c. In these figures, the solid NURBS curves are constructed using uniform weights, meaning that their NURBS basis functions are simply the B-spline basis functions shown in Figure 3.1a and Figure 3.2a. Consequently, the solid NURBS curves are in fact B-spline curves. The dashed curves are NURBS curves constructed using the NURBS basis functions shown in Figure 3.1a and Figure 3.2b. Increasing the weight associated with a control point increases the proximity of the NURBS curve to that specific control point, as demonstrated by the dashed NURBS curves. Conversely, reducing the weight induces a deviation away from the respective control point. For more details on NURBS, refer to the work of Piegl and Tiller (1996).

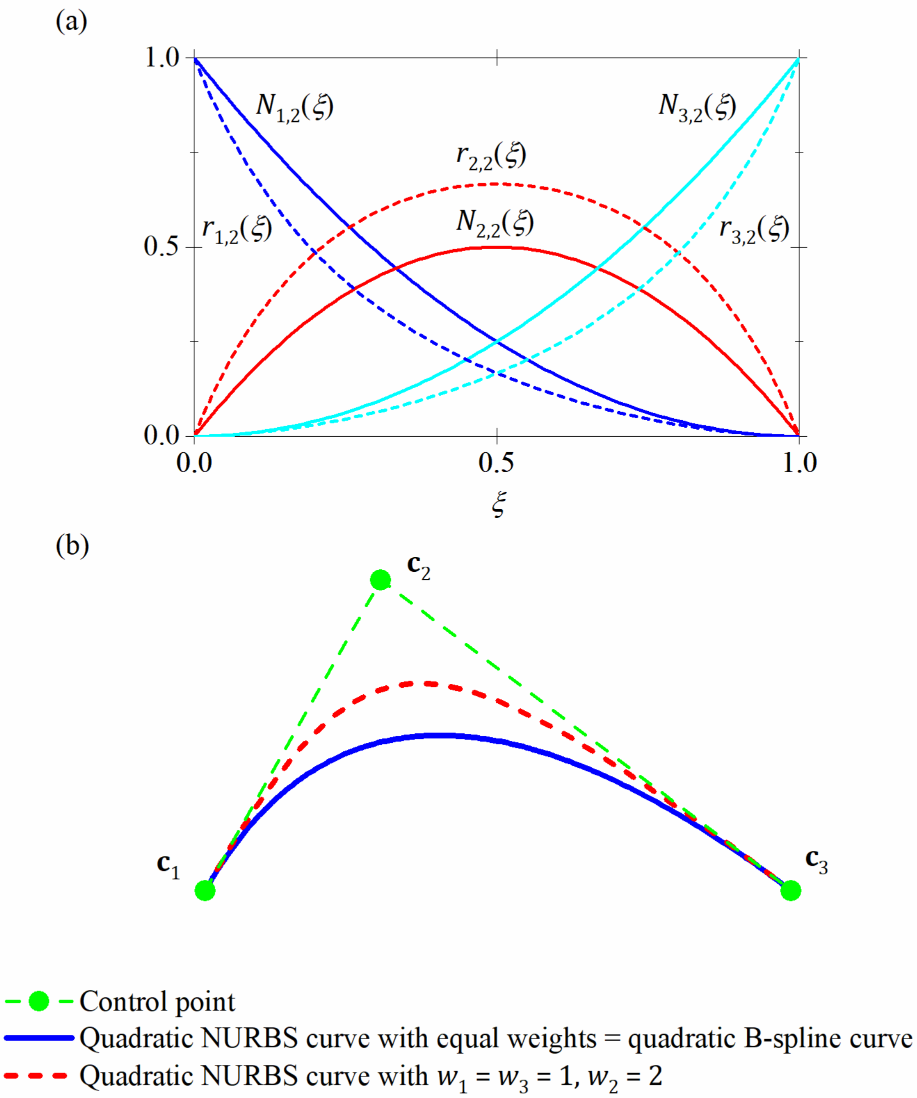

Figure 3.1 (a) quadratic B-spline and NURBS basis functions with $w_1 = w_3 = 1$, $w_2 = 2$, (b) quadratic NURBS curves, with knot vector $\Xi_q = \{0, 0, 0, 1, 1, 1\}$.

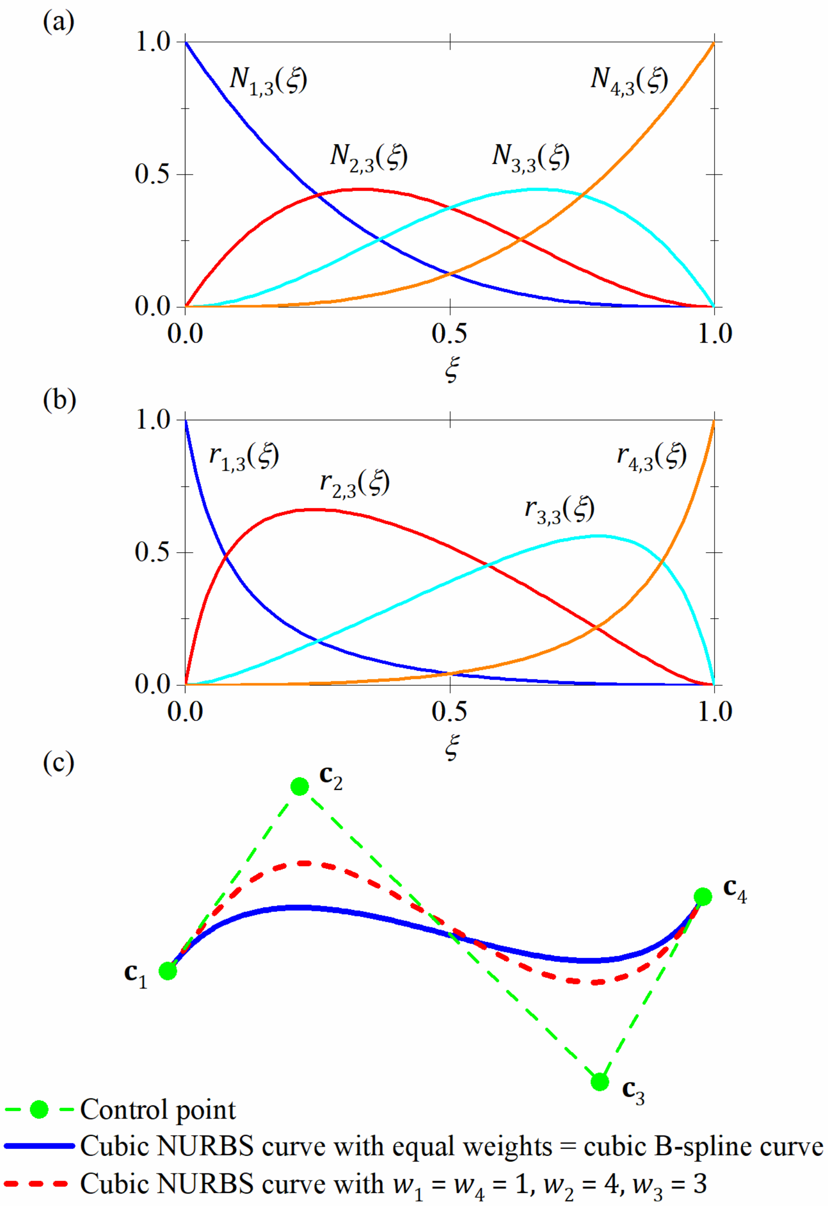

Figure 3.2 (a) Cubic B-spline basis functions, (b) cubic NURBS basis functions with $w_1 = w_4 = 1$, $w_2 = 4$, $w_3 = 3$, (c) cubic NURBS curves, with knot vector $\Xi_c = \{0, 0, 0, 0, 1, 1, 1, 1\}$.

CHAPTER 4

A PLANAR CURVED EULER-BERNOULLI BEAM ELEMENT FOR LARGE-DISPLACEMENT AND SMALL-STRAIN ANALYSIS USING NURBS CURVES WITH VARYING WEIGHTS

In this chapter, a novel planar curved Euler-Bernoulli beam element is developed for large-displacement and small-strain analysis, incorporating NURBS-based representations, the varying-weight concept, the small-strain assumption, and the thin-beam assumption. Curvilinear coordinate systems are employed to formulate the curved beam element, eliminating the need to transform finite element equations between local and global coordinates. The physical meanings of the derived strain components are clearly articulated. The performance of the proposed varying-weight element is validated through comparisons with a constant-weight element in five beam problems, considering factors such as accuracy, convergence with increasing DOFs, recovery of strain measures, and mitigation of locking effects.

4.1 Kinematics of planar curved Euler-Bernoulli beams

4.1.1 Beam configurations, basis vectors, and curvilinear coordinate systems

The total Lagrangian description is used to describe different configurations of a planar curved Euler-Bernoulli beam. This approach involves describing the beam's deformation through its two configurations, i.e., the initial and deformed configurations, as depicted in Figure 4.1. In the total Lagrangian description, the initial configuration serves as the reference configuration. Let S be the arc-length variable of the undeformed beam axis in the initial configuration. Let Q_0 denote a material point on the undeformed beam axis, located at S. After deformation, Q_0 undergoes a displacement to a new position q_0, as shown in Figure 4.1. The relationship between the coordinates of Q_0 and q_0 is expressed as follows:

$$\mathbf{u}_0(S) = \mathbf{r}_0(S) - \mathbf{R}_0(S) \tag{4.1}$$

where $\mathbf{R}_0(S)$ and $\mathbf{r}_0(S)$ represent, respectively, the coordinates of Q_0 and q_0 in the XY coordinate system. Moreover, $\mathbf{u}_0(S) = [u_{0X} \quad u_{0Y}]^{\mathrm{T}}$ denotes the vector of translational displacements from Q_0 to q_0.

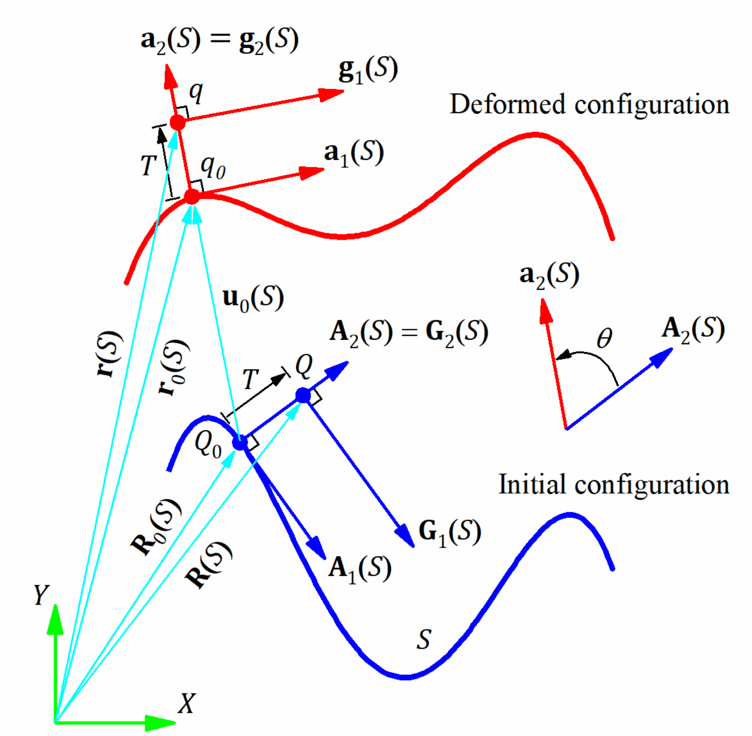

Figure 4.1 Initial and deformed configurations of a planar curved Euler-Bernoulli beam.

The tangent vectors of the reference and deformed beam axes, denoted by $\mathbf{A}_1(S)$ and $\mathbf{a}_1(S)$ respectively and shown in Figure 4.1, are determined as

$$\mathbf{A}_1(S) = \frac{\mathrm{d}\mathbf{R}_0(S)}{\mathrm{d}S} = \mathbf{R}_0'(S) \qquad \mathbf{a}_1(S) = \frac{\mathrm{d}\mathbf{r}_0(S)}{\mathrm{d}S} = \mathbf{r}_0'(S). \tag{4.2}$$

The use of primes indicates differentiations with respect to the arc-length S. Using the obtained tangent vectors, the director vectors of the reference and deformed beam axes, denoted, respectively, by $\mathbf{A}_2$ and $\mathbf{a}_2$ are written as

$$\mathbf{A}_2 = \mathbf{\Lambda}\left(\frac{\pi}{2}\right)\mathbf{A}_1 \qquad \mathbf{a}_2 = \mathbf{\Lambda}\left(\frac{\pi}{2}\right)\frac{\mathbf{a}_1}{\|\mathbf{a}_1\|} = \mathbf{\Lambda}\left(\frac{\pi}{2}\right)\frac{\mathbf{a}_1}{a_1} \tag{4.3}$$

where $\mathbf{\Lambda}(\varphi)$ is the rotation tensor, written in matrix form as $\mathbf{\Lambda}(\varphi) = \begin{bmatrix} \cos\varphi & -\sin\varphi \\ \sin\varphi & \cos\varphi \end{bmatrix}$. Note that $\mathbf{A}_1$, $\mathbf{A}_2$ and $\mathbf{a}_2$ are unit vectors. In addition, a_1 denotes the length of $\mathbf{a}_1$.

In the reference configuration, let Q denote a material point located on the same cross-section as Q_0. As shown in Figure 4.1, the coordinates of Q, denoted by $\mathbf{R}$, can be written as

$$\mathbf{R} = \mathbf{R}_0 + T\mathbf{A}_2. \tag{4.4}$$

After deformation, Q moves to a new position q, situated on the same cross-section but now in the deformed configuration. Subsequently, the coordinates of q, denoted by $\mathbf{r}$, are determined as

$$\mathbf{r} = \mathbf{r}_0 + T\mathbf{a}_2. \tag{4.5}$$

From the above expressions of $\mathbf{R}$ and $\mathbf{r}$, the following basis vectors are defined (Vo & Nanakorn, 2020)

$$\mathbf{G}_1 = \frac{\partial \mathbf{R}}{\partial S} = \mathbf{A}_1 + T\mathbf{A}_2' \qquad \mathbf{g}_1 = \frac{\partial \mathbf{r}}{\partial S} = \mathbf{a}_1 + T\mathbf{a}_2' \tag{4.6}$$

$$\mathbf{G}_2 = \frac{\partial \mathbf{R}}{\partial T} = \mathbf{A}_2 \qquad \mathbf{g}_2 = \frac{\partial \mathbf{r}}{\partial T} = \mathbf{a}_2. \tag{4.7}$$

It is evident from their expressions that $\mathbf{G}_1$ and $\mathbf{g}_1$ are tangent to their corresponding beam axes, while $\mathbf{G}_2$ and $\mathbf{g}_2$ are tangent to their corresponding cross-sections. For Euler-Bernoulli beams, a cross-section always remains perpendicular to the beam axis. Note that the derivatives of $\mathbf{A}_2$ and $\mathbf{a}_2$, which are unit vectors normal to their respective beam axes, with respect to S are tangent to their respective beam axes.

The basis vectors $\mathbf{G}_1$ and $\mathbf{G}_2$ are ultilized to form the covariant curvilinear coordinate system employed in the derivation. For the expression of the virtual work equation using the Green-Lagrange strain and second Piola-Kirchhoff stress tensors in this study, the reciprocal contravariant coordinate system is also introduced. The contravariant coordinate system is formed by the reciprocal basis vectors of $\mathbf{G}_1$ and $\mathbf{G}_2$, denoted by $\mathbf{G}^1$ and $\mathbf{G}^2$, respectively. The vectors $\mathbf{G}^1$ and $\mathbf{G}^2$ are defined by the following relation:

$$\mathbf{G}_\alpha \cdot \mathbf{G}^\beta = \begin{cases} 0 & \alpha \neq \beta \\ 1 & \alpha = \beta \end{cases} \tag{4.8}$$

where $\alpha, \beta = 1{,}2$. This definition yields

$$\mathbf{G}^1 = \frac{\mathbf{G}_1}{\mathbf{G}_1 \cdot \mathbf{G}_1} \qquad \mathbf{G}^2 = \mathbf{G}_2. \tag{4.9}$$

For more details about curvilinear coordinate systems, please refer to the studies of Vo and Nanakorn (2020, 2020).

4.1.2 The Green-Lagrange strain and second Piola-Kirchhoff stress tensors

The Green-Lagrange strain tensor **E** is written as (Vo & Nanakorn, 2020)

$$\mathbf{E} = E_{\alpha\beta}\mathbf{G}^\alpha \otimes \mathbf{G}^\beta = \frac{1}{2}(\mathbf{F}^{\mathrm{T}}\mathbf{F} - \mathbf{G}) \tag{4.10}$$

where **F** is the deformation gradient tensor and **G** is the metric tensor, defined in the reference configuration. Explicitly, **F** and **G**, are given as (Basar & Weichert, 2000)

$$\mathbf{F} = \mathbf{g}_\alpha \otimes \mathbf{G}^\alpha = \mathbf{g}_1 \otimes \mathbf{G}^1 + \mathbf{g}_2 \otimes \mathbf{G}^2 \tag{4.11}$$

$$\mathbf{G} = G_{\alpha\beta}\mathbf{G}^\alpha \otimes \mathbf{G}^\beta = (\mathbf{G}_1 \cdot \mathbf{G}_1)\mathbf{G}^1 \otimes \mathbf{G}^1 + \mathbf{G}^2 \otimes \mathbf{G}^2. \tag{4.12}$$

Note that the following relationship holds:

$$G_{12} = \mathbf{G}_1 \cdot \mathbf{G}_2 = G_{21} = \mathbf{G}_2 \cdot \mathbf{G}_1 = 0. \tag{4.13}$$

In Figure 4.1, the angle from the vectors $\mathbf{A}_2$ to $\mathbf{a}_2$ is the rotation of the cross-section and is denoted by θ. The rotation can be expressed as

$$\mathbf{a}_2 = \mathbf{\Lambda}(\theta)\mathbf{A}_2. \tag{4.14}$$

Additionally, the right stretch tensor $\mathbf{Q}$ is determined as

$$\mathbf{Q} = \mathbf{\Lambda}^{\mathrm{T}}(\theta)\mathbf{F}. \tag{4.15}$$

It follows that

$$\begin{aligned}\mathbf{E} = \frac{1}{2}(\mathbf{F}^{\mathrm{T}}\mathbf{F} - \mathbf{G}) &= \frac{1}{2}[(\mathbf{\Lambda}(\theta)\mathbf{Q})^{\mathrm{T}}(\mathbf{\Lambda}(\theta)\mathbf{Q}) - \mathbf{G}] \\ &= \frac{1}{2}(\mathbf{Q}^{\mathrm{T}}\mathbf{\Lambda}^{\mathrm{T}}(\theta)\mathbf{\Lambda}(\theta)\mathbf{Q} - \mathbf{G}) = \frac{1}{2}(\mathbf{Q}^{\mathrm{T}}\mathbf{Q} - \mathbf{G}).\end{aligned} \tag{4.16}$$

Define a tensor $\mathbf{L}$ as

$$\mathbf{L} = \mathbf{Q} - \mathbf{G}. \tag{4.17}$$

By using Equation (4.17) in Equation (4.16), the Green-Lagrange strain tensor in Equation (4.10) is expressed as

$$\begin{aligned}\mathbf{E} = \frac{1}{2}(\mathbf{Q}^{\mathrm{T}}\mathbf{Q} - \mathbf{G}) &= \frac{1}{2}(\mathbf{L}^{\mathrm{T}}\mathbf{L} + \mathbf{L}^{\mathrm{T}}\mathbf{G} + \mathbf{G}^{\mathrm{T}}\mathbf{L} + \mathbf{G}^{\mathrm{T}}\mathbf{G} - \mathbf{G}) \\ &= \frac{1}{2}(\mathbf{L}^{\mathrm{T}}\mathbf{L} + \mathbf{L}^{\mathrm{T}} + \mathbf{L}).\end{aligned} \tag{4.18}$$

In the above equation, some properties of the metric tensor $\mathbf{G}$ are utilized, i.e., $\mathbf{G}^{\mathrm{T}} = \mathbf{G}$ and $\mathbf{GC} = \mathbf{CG} = \mathbf{C}$ for all arbitrary tensors $\mathbf{C}$ (Basar & Weichert, 2000).

In essence, the orthonormal vectors $\mathbf{a}_1/a_1$ and $\mathbf{a}_2$ can be seen as the results of rotating the orthonormal vectors $\mathbf{A}_1$ and $\mathbf{A}_2$ by the angle θ, respectively. Similarly, the orthonormal vectors $\mathbf{g}_1/\|\mathbf{g}_1\|$ and $\mathbf{g}_2$ can be regarded as the results of rotating the orthonormal vectors $\mathbf{G}_1/\|\mathbf{G}_1\|$ and $\mathbf{G}_2$ by the angle θ, respectively. Thus, the rotation tensor $\mathbf{\Lambda}(\theta)$ can be written in terms of these vectors as

$$\mathbf{\Lambda}(\theta) = \frac{\mathbf{a}_1}{a_1} \otimes \mathbf{A}_1 + \mathbf{a}_2 \otimes \mathbf{A}_2 = \frac{\mathbf{g}_1}{g_1} \otimes \frac{\mathbf{G}_1}{G_1} + \mathbf{g}_2 \otimes \mathbf{G}_2 \tag{4.19}$$

where G_1 and g_1 denote the lengths of $\mathbf{G}_1$ and $\mathbf{g}_1$, respectively.

Straightforwardly, the transpose of $\mathbf{\Lambda}(\theta)$ is obtained as

$$\mathbf{\Lambda}^{\mathrm{T}}(\theta) = \mathbf{A}_1 \otimes \frac{\mathbf{a}_1}{a_1} + \mathbf{A}_2 \otimes \mathbf{a}_2 = \frac{\mathbf{G}_1}{G_1} \otimes \frac{\mathbf{g}_1}{g_1} + \mathbf{G}_2 \otimes \mathbf{g}_2. \tag{4.20}$$

Using Equations (4.9), (4.11), (4.12), (4.15), and (4.20) with Equation (4.17) and noting that $\mathbf{g}_1 \cdot \mathbf{g}_2 = \mathbf{g}_2 \cdot \mathbf{g}_1 = 0$ yield

$$\mathbf{L} = (g_1 - G_1)G_1\mathbf{G}^1 \otimes \mathbf{G}^1. \tag{4.21}$$

Let k_0 denote the signed curvature of the initial configuration, given by

$$\begin{aligned} k_0 = \frac{\|\mathbf{R}_0'(S)\|\|\mathbf{R}_0''(S)\| \sin \Omega}{\|\mathbf{R}_0'(S)\|^3} = \frac{\mathbf{R}_0''(S) \cdot \mathbf{\Lambda}\left(\frac{\pi}{2}\right) \mathbf{R}_0'(S)}{\|\mathbf{R}_0'(S)\|^3} = \frac{\mathbf{A}_1' \cdot \mathbf{\Lambda}\left(\frac{\pi}{2}\right) \mathbf{A}_1}{\|\mathbf{A}_1\|^3} \\ = \mathbf{A}_1' \cdot \mathbf{A}_2 = -\mathbf{A}_1 \cdot \mathbf{A}_2' \end{aligned} \tag{4.22}$$

where Ω is the angle from $\mathbf{R}_0'(S)$ to $\mathbf{R}_0''(S)$. Similarly, let k denote the signed curvature of the deformed configuration, given by

$$k = \frac{\|\mathbf{r}_0'(S)\| \|\mathbf{r}_0''(S)\| \sin \omega}{\|\mathbf{r}_0'(S)\|^3} = \frac{\mathbf{r}_0''(S) \cdot \mathbf{\Lambda}\left(\frac{\pi}{2}\right) \mathbf{r}_0'(S)}{\|\mathbf{r}_0'(S)\|^3} = \frac{\mathbf{a}_1' \cdot \mathbf{\Lambda}\left(\frac{\pi}{2}\right) \mathbf{a}_1}{\|\mathbf{a}_1\|^3}$$
$$= \frac{\mathbf{a}_1' \cdot (a_1 \mathbf{a}_2)}{a_1^3} = -\frac{\mathbf{a}_1 \cdot \mathbf{a}_2'}{a_1^2} \tag{4.23}$$

where ω is the angle from $\mathbf{r}_0'(S)$ to $\mathbf{r}_0''(S)$. In addition, in Equations (4.22) and (4.23), the following is used, i.e.,

$$(\mathbf{A}_1 \cdot \mathbf{A}_2)' = 0 = \mathbf{A}_1' \cdot \mathbf{A}_2 + \mathbf{A}_1 \cdot \mathbf{A}_2' \quad (\mathbf{a}_1 \cdot \mathbf{a}_2)' = 0 = \mathbf{a}_1' \cdot \mathbf{a}_2 + \mathbf{a}_1 \cdot \mathbf{a}_2'. \tag{4.24}$$

Recall that $\mathbf{A}_1$ and $\mathbf{A}_2'$ are both tangent to the initial beam axis and $\mathbf{A}_1$ is a unit vector. In addition, $\mathbf{a}_1/a_1$ and $\mathbf{a}_2'$ are tangent to the deformed beam axis and $\mathbf{a}_1/a_1$ is a unit vector. It follows that

$$\mathbf{A}_2' = (\mathbf{A}_1 \cdot \mathbf{A}_2')\mathbf{A}_1 = -k_0 \mathbf{A}_1 \qquad \mathbf{a}_2' = \left(\frac{\mathbf{a}_1}{a_1} \cdot \mathbf{a}_2'\right)\frac{\mathbf{a}_1}{a_1} = -k\mathbf{a}_1. \tag{4.25}$$

Consequently, $\mathbf{G}_1$ and $\mathbf{g}_1$ become

$$\mathbf{G}_1 = \mathbf{A}_1 + T\mathbf{A}_2' = (1 - Tk_0)\mathbf{A}_1 \qquad \mathbf{g}_1 = \mathbf{a}_1 + T\mathbf{a}_2' = (1 - Tk)\mathbf{a}_1. \tag{4.26}$$

Subsequently, the lengths of $\mathbf{G}_1$ and $\mathbf{g}_1$ are obtained as

$$G_1 = 1 - Tk_0 \qquad g_1 = a_1 - a_1 Tk. \tag{4.27}$$

Substituting Equation (4.27) into Equation (4.21) yields

$$\mathbf{L} = \left[(a_1 - 1) - T\left(k_0(a_1 - 1) + (a_1 k - k_0)\right) + T^2 k_0 (a_1 k - k_0)\right]\mathbf{G}^1$$
$$\otimes \mathbf{G}^1. \tag{4.28}$$

For thin beams, T is small. In addition, under small strains, $(a_1 - 1)$ and $T(a_1 k - k_0)$ are small. Consequently, $Tk_0(a_1 - 1)$ and $T^2 k_0(a_1 k - k_0)$ in Equation (4.28) can be neglected, which yields

$$\mathbf{L} = [(a_1 - 1) - T(a_1 k - k_0)]\mathbf{G}^1 \otimes \mathbf{G}^1. \tag{4.29}$$

It follows that

$$\mathbf{L}^\mathrm{T}\mathbf{L} = [(a_1 - 1)^2 - 2T(a_1 - 1)(a_1 k - k_0) + T^2(a_1 k - k_0)^2]\mathbf{G}^1 \otimes \mathbf{G}^1. \tag{4.30}$$

Since T, $(a_1 - 1)$, and $T(a_1 k - k_0)$ are small, $\mathbf{L}^\mathrm{T}\mathbf{L}$ in Equation (4.18) can be discarded to give

$$\mathbf{E} = \frac{1}{2}(\mathbf{L}^\mathrm{T} + \mathbf{L}) = \mathbf{L}. \tag{4.31}$$

Consequently, the matrix form of the tensor $\mathbf{E}$ is given by

$$\mathbf{E} = \begin{bmatrix} E_{11} & E_{12} \\ E_{21} & E_{22} \end{bmatrix} = \begin{bmatrix} (a_1 - 1) - T(a_1 k - k_0) & 0 \\ 0 & 0 \end{bmatrix} = \begin{bmatrix} \Gamma_{11} - TK_{11} & 0 \\ 0 & 0 \end{bmatrix}. \tag{4.32}$$

Here, Γ_{11} represents the axial strain and K_{11} effectively represents the change in curvature due to bending. It is worth noting that axial deformation in a curved beam also leads to changes in curvature as evident in Equation (4.23), where the curvature varies with a_1.

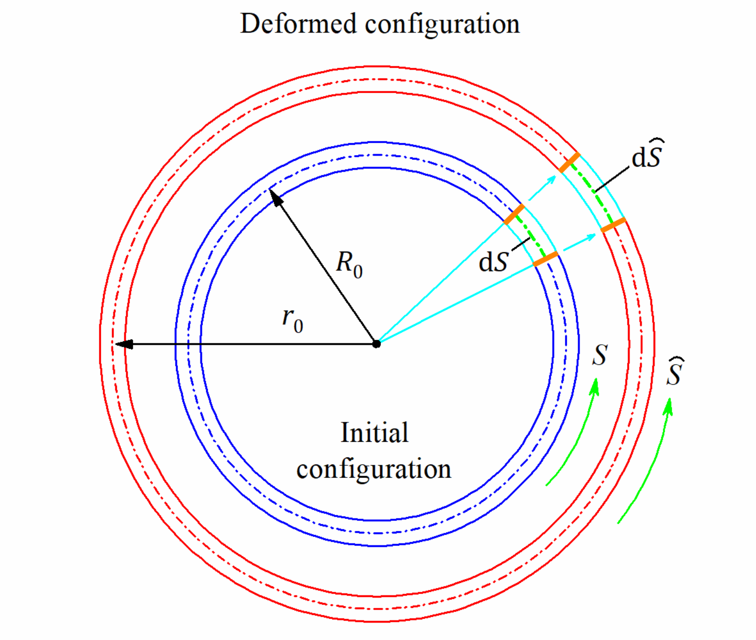

Figure 4.2 A thin circular ring under radial expansion.

To demonstrate the physical meanings of the two components of E_{11}, consider a thin circular ring with an initial axis radius of R_0, as shown in Figure 4.2. The ring is deformed into a larger circular ring, with its axis now having a radius of r_0, as also shown in Figure 4.2. This deformation is created such that each cross-section moves outward solely in the radial direction. Let S and $\hat{S}$ represent the arc-length parameters of the undeformed and deformed rings, respectively. The directions of the two arc-length parameters are as shown in Figure 4.2. The signed curvatures of the two beam axes are obtained as

$$k_0 = \frac{1}{R_0} \qquad\qquad k = \frac{1}{r_0}. \tag{4.33}$$

Let $\mathbf{r}_0(\hat{S})$ be the position vector of the deformed ring. The variable $\mathbf{a}_1$ in Equation (4.2) is then expressed as

$$\mathbf{a}_1 = \frac{\mathrm{d}\mathbf{r}_0}{\mathrm{d}S} = \frac{\mathrm{d}\mathbf{r}_0}{\mathrm{d}\hat{S}}\frac{\mathrm{d}\hat{S}}{\mathrm{d}S} = \mathbf{n}\frac{\mathrm{d}\hat{S}}{\mathrm{d}S} \tag{4.34}$$

where $\mathbf{n}$ is a unit tangent vector of the deformed axis. It follows that

$$a_1 = \|\mathbf{a}_1\| = \frac{\mathrm{d}\hat{S}}{\mathrm{d}S} = \frac{r_0}{R_0}. \tag{4.35}$$

Subsequently, Γ_{11} and K_{11} are obtained as

$$\begin{aligned}\Gamma_{11} &= a_1 - 1 = \frac{r_0}{R_0} - 1 \\ &= \frac{2\pi r_0 - 2\pi R_0}{2\pi R_0}\end{aligned} \qquad K_{11} = a_1 k - k_0 = \frac{r_0}{R_0}\frac{1}{r_0} - \frac{1}{R_0} = 0\,. \tag{4.36}$$

As expected, in this example, there is only axial strain, and the bending strain is zero. There is no change in curvature due to bending, as indicated by $K_{11} = 0$. The observed change in curvature is solely due to axial deformation.

Next, the second Piola-Kirchhoff stress tensor $\mathbf{S}$ is written in the covariant curvilinear coordinate system as

$$\mathbf{S} = S^{\alpha\beta}\mathbf{G}_\alpha \otimes \mathbf{G}_\beta. \tag{4.37}$$

In this study, linear elastic isotropic materials are considered. The relationship between S^{11} and E_{11} is described as (Vo & Nanakorn, 2020)

$$S^{11} = \bar{E}E_{11} \tag{4.38}$$

where $\bar{E}$ denotes Young's modulus measured in the covariant curvilinear coordinate system. Let E represent Young's modulus of the material. Following Vo and Nanakorn (2020), it is assumed in this study that, for thin beams, $\bar{E}$ can be approximated as E without significant error. Under this assumption, $\bar{E}$ on a cross-section is therefore constant.

4.1.3 Virtual work principle

The virtual work equation is written as

$$\delta\Pi_{int} - \delta\Pi_{ext} = 0 \tag{4.39}$$

where $\delta\Pi_{int}$ and $\delta\Pi_{ext}$ are, respectively, the internal and external virtual work.

The resultant internal forces are defined as

$$N^{11} = \int_A S^{11}\mathrm{d}A = EA\mathit{\Gamma}_{11} \qquad M^{11} = -\int_A TS^{11}\mathrm{d}A = EIK_{11} \tag{4.40}$$

with N^{11} being the resultant axial force, and M^{11} being the resultant bending moment. In addition, A is the cross-sectional area, and I represents the cross-sectional moment of inertia.

By utilizing Equation (4.40), the internal virtual work is obtained as

$$\begin{aligned}\delta\Pi_{int} &= \int_V \delta E_{11}S^{11}dV = \int_0^l\int_A \delta(\mathit{\Gamma}_{11} - TK_{11})E(\mathit{\Gamma}_{11} - TK_{11})dA\,dS \\ &= \int_0^l \delta\mathbf{\Gamma}^{\mathrm{T}}\mathbf{D}\mathbf{\Gamma}\,\mathrm{d}S\end{aligned} \tag{4.41}$$

where

$$\mathbf{\Gamma} = [\mathit{\Gamma}_{11} \quad K_{11}]^{\mathrm{T}} \qquad \mathbf{D} = \begin{bmatrix} EA & 0 \\ 0 & EI \end{bmatrix}. \tag{4.42}$$

In addition, V and l are, respectively, the volume and length of the beam element in the reference configuration.

To complete the virtual work equation, the external virtual work is expressed as

$$\delta\Pi_{ext} = \int_0^l [\delta u_{0X}(S) f_X(S) + \delta u_{0Y}(S) f_Y(S) + \delta\theta(S) m(S)] \mathrm{d}S \\ + \delta u_{0X}(0) F_X(0) + \delta u_{0Y}(0) F_Y(0) + \delta\theta(0) M(0) \\ + \delta u_{0X}(l) F_X(l) + \delta u_{0Y}(l) F_Y(l) + \delta\theta(l) M(l). \tag{4.43}$$

Here, $u_{0X}(S)$ and $u_{0Y}(S)$ represent, respectively, the displacements of the beam axis in the X and Y directions, as defined in Equation (4.1), while $\theta(S)$ is the rotation of the cross-section, introduced earlier. Moreover, $f_X(S)$ and $f_Y(S)$ are, respectively, the distributed forces applied to the beam axis, while $m(S)$ is the distributed moment. Additionally, $F_X(0)$, $F_Y(0)$, and $M(0)$ are the applied concentrated forces and moment at $S = 0$, and $F_X(l)$, $F_Y(l)$, and $M(l)$ are the applied concentrated forces and moment at $S = l$.

4.2 NURBS representations of beam configurations with varying weights

4.2.1 Representations of beam axes using cubic NURBS curves

Originally, both reference and deformed beam axes are parameterized by the arch-length S. Here, these beam axes are further represented using NURBS curves as

$$\mathbf{R}_0(\xi) = \sum_{i=1}^{n} R_{i,p}(\xi)\mathbf{C}_i \qquad \mathbf{r}_0(\xi) = \sum_{i=1}^{n} r_{i,p}(\xi)\mathbf{c}_i \tag{4.44}$$

where p denotes the degree of the basis function, n is the number of control points, and $\mathbf{C}_i = [X_i \quad Y_i]^{\mathrm{T}}$ and $\mathbf{c}_i = [x_i \quad y_i]^{\mathrm{T}}$ represent the i-th control points in the reference and deformed configurations, respectively. In addition, $R_{i,p}(\xi)$ and $r_{i,p}(\xi)$ are NURBS basis functions, given by

$$R_{i,p}(\xi) = \frac{N_{i,p}(\xi)W_i}{\sum_{j=1}^{n} N_{j,p}(\xi)W_j} \qquad r_{i,p}(\xi) = \frac{N_{i,p}(\xi)w_i}{\sum_{j=1}^{n} N_{j,p}(\xi)w_j} \tag{4.45}$$

where W_i and w_i denote non-negative weights, and $N_{i,p}(\xi)$ denotes a B-spline basis function, defined over a knot vector $\Xi = \{\xi_1, \xi_2, \dots, \xi_{n+p+1}\}$, where $\xi_i \leq \xi_{i+1}$ is a knot value.

Using Equations (4.44) in Equation (4.1) gives

$$\mathbf{u}_0(\xi) = \begin{bmatrix} u_{0X}(\xi) \\ u_{0Y}(\xi) \end{bmatrix} = \mathbf{r}_0(\xi) - \mathbf{R}_0(\xi) = \sum_{i=1}^{n} r_{i,p}(\xi)\mathbf{c}_i - \sum_{i=1}^{n} R_{i,p}(\xi)\mathbf{C}_i. \tag{4.46}$$

Given that $\mathbf{C}_i$ is constant, $\mathbf{u}_0(\xi)$ dependents solely on $\mathbf{c}_i$.

This study employs cubic NURBS representations, i.e., $p = 3$, for Euler-Bernoulli beams. By using $\xi \in [0, 1]$ and $\Xi = \Xi_\mathrm{c} = \{0, 0, 0, 0, 1, 1, 1, 1\}$, the cubic NURBS consists of four control points, i.e., $n = 4$, and four cubic B-spline basis functions determined in Equations (3.4) and (3.5).

4.2.2 Degrees of freedom

As previously mentioned, different beam configurations can be optimally represented by NURBS curves using various combinations of weights in their NURBS basis functions. Consequently, allowing some of the weights to vary constitutes a better strategy for representing different configurations. In this study, the weights associated with the second and the third control points in the deformed configuration, denoted by w_2 and w_3 in Equation (4.45), are allowed to vary. Thus, the deformed configuration is represented using $\mathbf{c}_i = [x_i \quad y_i]^\mathrm{T}$, $i = 1, 2, 3, 4$, along with w_2 and w_3. These 10 variables can be directly used as DOFs. However, they do not include end rotational DOFs. The absence of end rotational DOFs poses challenges in enforcing rotational continuity across elements, prescribing end rotations, and applying external end moments. To address this limitation, a vector $\mathbf{U}$, which incorporates the end rotations, is introduced as

$$\mathbf{U} = [x_1 \quad y_1 \quad \theta_1 \quad l_1 \quad w_2 \quad w_3 \quad l_3 \quad x_4 \quad y_4 \quad \theta_4]^\mathrm{T}. \tag{4.47}$$

Here, θ_1 and θ_4 denotes θ at $S = 0$ and l, respectively, while l_i is the distance between the control points $\mathbf{c}_i$ and $\mathbf{c}_{i+1}$ in the deformed configuration as depicted in Figure 4.3. In this study, the 10 members of $\mathbf{U}$ are used as DOFs.

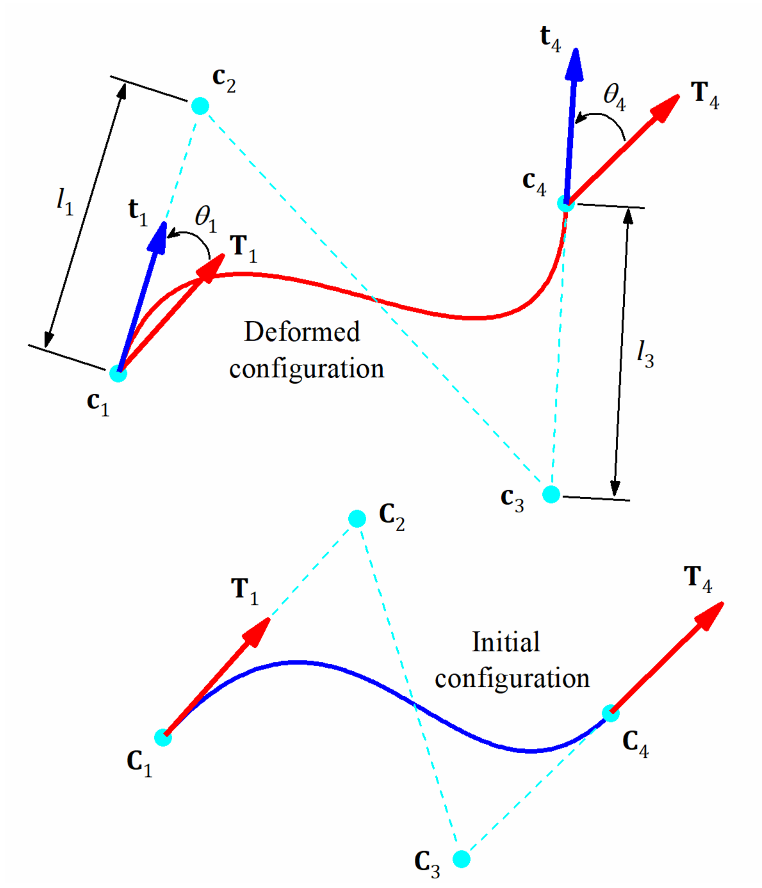

Figure 4.3 End tangent vectors and end rotations of a cubic curved beam element.

In Equation (4.47), instead of utilizing x_2, y_2, x_3, and y_3 as DOFs, θ_1, θ_4, l_1, and l_3 are employed. To achieve this, $\mathbf{c}_2$ and $\mathbf{c}_3$ are written in terms of θ_1, θ_4, l_1, and l_3 as

$$\mathbf{c}_2 = \mathbf{c}_1 + l_1\boldsymbol{\Lambda}(\theta_1)\mathbf{T}_1 \qquad \mathbf{c}_3 = \mathbf{c}_4 - l_3\boldsymbol{\Lambda}(\theta_4)\mathbf{T}_4. \tag{4.48}$$

As shown in Figure 4.3, $\mathbf{T}_1$ and $\mathbf{T}_4$ denote, respectively, the unit vectors tangent to the reference beam axis at $\mathbf{C}_1$ and $\mathbf{C}_4$, given by

$$\mathbf{T}_1 = \frac{\mathbf{C}_2 - \mathbf{C}_1}{\|\mathbf{C}_2 - \mathbf{C}_1\|} \qquad \mathbf{T}_4 = \frac{\mathbf{C}_4 - \mathbf{C}_3}{\|\mathbf{C}_4 - \mathbf{C}_3\|}. \tag{4.49}$$

Similarly, $\mathbf{t}_1$ and $\mathbf{t}_4$ denote, respectively, the unit vectors tangent to the deformed beam axis at $\mathbf{p}_1$ and $\mathbf{p}_4$, expressed as

$$\begin{aligned} \mathbf{t}_1 = \mathbf{\Lambda}(\theta_1)\mathbf{T}_1 &= \frac{\mathbf{c}_2 - \mathbf{c}_1}{\|\mathbf{c}_2 - \mathbf{c}_1\|} & \qquad \mathbf{t}_4 = \mathbf{\Lambda}(\theta_4)\mathbf{T}_4 &= \frac{\mathbf{c}_4 - \mathbf{c}_3}{\|\mathbf{c}_4 - \mathbf{c}_3\|} \\ &= \frac{\mathbf{c}_2 - \mathbf{c}_1}{l_1} & &= \frac{\mathbf{c}_4 - \mathbf{c}_3}{l_3}. \end{aligned} \tag{4.50}$$

It is important to note that $\mathbf{C}_1$, $\mathbf{C}_4$, $\mathbf{c}_1$ and $\mathbf{c}_4$ are always located at the ends of the beam element.

By using Equation (4.48), $u_{0X}(\xi)$ and $u_{0Y}(\xi)$ in Equation (4.46) can now be expressed in terms of x_1, y_1, x_4, y_4, θ_1, θ_4, l_1, and l_3, instead of x_1, y_1, x_2, y_2, x_3, y_3, x_4, and y_4. As w_2 and w_3 are treated as DOFs, $u_{0X}(\xi)$ and $u_{0Y}(\xi)$ are now written in terms of the DOF vector $\mathbf{U}$ in Equation (4.47).

4.2.3 Relationship between beam axis parameters

The initial and deformed beam axes are now parameterized using S and ξ. The relationship between $\mathrm{d}S$ and $\mathrm{d}\xi$ is expressed as

$$\mathrm{d}S = \left\| \frac{\mathrm{d}\mathbf{R}_0(\xi)}{\mathrm{d}\xi} \right\| \mathrm{d}\xi. \tag{4.51}$$

The above equation facilitates integrations in the S domain of integrands expressed in terms of ξ to be determined in the ξ domain. In addition, it enables the determination of derivatives of functions of ξ with respect to S to be computed via the chain rule (Vo & Nanakorn, 2020).

4.3 Planar Euler-Bernoulli beam element using cubic NURBS curves with varying weights

Define a matrix **B** as

$$\mathbf{B} = \begin{bmatrix} \frac{\partial \Gamma_{11}}{\partial x_1} & \frac{\partial \Gamma_{11}}{\partial y_1} & \frac{\partial \Gamma_{11}}{\partial \theta_1} & \frac{\partial \Gamma_{11}}{\partial l_1} & \frac{\partial \Gamma_{11}}{\partial w_2} & \frac{\partial \Gamma_{11}}{\partial w_3} & \frac{\partial \Gamma_{11}}{\partial l_3} & \frac{\partial \Gamma_{11}}{\partial x_4} & \frac{\partial \Gamma_{11}}{\partial y_4} & \frac{\partial \Gamma_{11}}{\partial \theta_4} \\ \frac{\partial K_{11}}{\partial x_1} & \frac{\partial K_{11}}{\partial y_1} & \frac{\partial K_{11}}{\partial \theta_1} & \frac{\partial K_{11}}{\partial l_1} & \frac{\partial K_{11}}{\partial w_2} & \frac{\partial K_{11}}{\partial w_3} & \frac{\partial K_{11}}{\partial l_3} & \frac{\partial K_{11}}{\partial x_4} & \frac{\partial K_{11}}{\partial y_4} & \frac{\partial K_{11}}{\partial \theta_4} \end{bmatrix}. \tag{4.52}$$

Subsequently, the variation of $\mathbf{\Gamma}$ in Equation (4.42) can be determined as

$$\delta\mathbf{\Gamma} = \mathbf{B}\delta\mathbf{U}. \tag{4.53}$$

The internal virtual work is then written as

$$\delta\Pi_{int} = \delta\mathbf{U}^{\mathrm{T}} \int_0^l \mathbf{B}^{\mathrm{T}}\mathbf{D}\mathbf{\Gamma}\mathrm{d}S. \tag{4.54}$$

Equation (4.14) yields

$$\delta\mathbf{a}_2 = \frac{\mathrm{d}\mathbf{\Lambda}(\theta)}{\mathrm{d}\theta}\mathbf{A}_2\delta\theta = -\mathbf{\Lambda}\left(\theta - \frac{\pi}{2}\right)\mathbf{A}_2\delta\theta = -\frac{\mathbf{a}_1}{a_1}\delta\theta \tag{4.55}$$

which leads to

$$\delta\theta = -\frac{\mathbf{a}_1}{a_1} \cdot \delta\mathbf{a}_2. \tag{4.56}$$

Introduce vectors $\mathbf{H}_X$, $\mathbf{H}_Y$ and $\mathbf{H}_\theta$ as

$$\mathbf{H}_X = \begin{bmatrix} \frac{\partial u_{0X}}{\partial x_1} & \frac{\partial u_{0X}}{\partial y_1} & \frac{\partial u_{0X}}{\partial \theta_1} & \frac{\partial u_{0X}}{\partial l_1} & \frac{\partial u_{0X}}{\partial w_2} & \frac{\partial u_{0X}}{\partial w_3} & \frac{\partial u_{0X}}{\partial l_3} & \frac{\partial u_{0X}}{\partial x_4} & \frac{\partial u_{0X}}{\partial y_4} & \frac{\partial u_{0X}}{\partial \theta_4} \end{bmatrix} \tag{4.57}$$

$$\mathbf{H}_Y = \begin{bmatrix} \frac{\partial u_{0Y}}{\partial x_1} & \frac{\partial u_{0Y}}{\partial y_1} & \frac{\partial u_{0Y}}{\partial \theta_1} & \frac{\partial u_{0Y}}{\partial l_1} & \frac{\partial u_{0Y}}{\partial w_2} & \frac{\partial u_{0Y}}{\partial w_3} & \frac{\partial u_{0Y}}{\partial l_3} & \frac{\partial u_{0Y}}{\partial x_4} & \frac{\partial u_{0Y}}{\partial y_4} & \frac{\partial u_{0Y}}{\partial \theta_4} \end{bmatrix} \tag{4.58}$$

$$\mathbf{H}_\theta = -\frac{1}{a_1}\left[\mathbf{a}_1 \cdot \frac{\partial \mathbf{a}_2}{\partial x_1} \quad \mathbf{a}_1 \cdot \frac{\partial \mathbf{a}_2}{\partial y_1} \quad \mathbf{a}_1 \cdot \frac{\partial \mathbf{a}_2}{\partial \theta_1} \quad \mathbf{a}_1 \cdot \frac{\partial \mathbf{a}_2}{\partial l_1} \quad \mathbf{a}_1 \cdot \frac{\partial \mathbf{a}_2}{\partial w_2} \quad \mathbf{a}_1 \cdot \frac{\partial \mathbf{a}_2}{\partial w_3} \quad \mathbf{a}_1 \cdot \frac{\partial \mathbf{a}_2}{\partial l_3} \quad \mathbf{a}_1 \cdot \frac{\partial \mathbf{a}_2}{\partial x_4} \quad \mathbf{a}_1 \cdot \frac{\partial \mathbf{a}_2}{\partial y_4} \quad \mathbf{a}_1 \cdot \frac{\partial \mathbf{a}_2}{\partial \theta_4}\right]. \tag{4.59}$$

By using $\mathbf{H}_X$, $\mathbf{H}_Y$, and $\mathbf{H}_\theta$, the variations of u_{0X}, u_{0Y} and θ can be expressed as

$$\delta u_{0X} = \mathbf{H}_X \delta \mathbf{U} \qquad \delta u_{0Y} = \mathbf{H}_Y \delta \mathbf{U} \qquad \delta\theta = \mathbf{H}_\theta \delta \mathbf{U}. \tag{4.60}$$

Define an end force vector **P** as

$$\mathbf{P} = [F_X(0) \quad F_Y(0) \quad M(0) \quad 0 \quad 0 \quad 0 \quad 0 \quad F_X(l) \quad F_Y(l) \quad M(l)]^{\mathrm{T}}. \tag{4.61}$$

The external virtual work is then expressed as

$$\delta\Pi_{ext} = \delta\mathbf{U}^{\mathrm{T}} \int_0^l (\mathbf{H}_X^{\mathrm{T}} f_X + \mathbf{H}_Y^{\mathrm{T}} f_{\mathrm{Y}} + \mathbf{H}_\theta^{\mathrm{T}} m)\mathrm{d}S + \delta\mathbf{U}^{\mathrm{T}}\mathbf{P}. \tag{4.62}$$

Equations (4.39), (4.54), and (4.62) lead to the system of nonlinear governing equations, i.e.,

$$\mathbf{\Phi} = \mathbf{p} + \mathbf{P} \tag{4.63}$$

where

$$\mathbf{\Phi} = \int_0^l \mathbf{B}^{\mathrm{T}}\mathbf{D}\mathbf{\Gamma}\mathrm{d}S \qquad \mathbf{p} = \int_0^l (\mathbf{H}_X^{\mathrm{T}} f_X + \mathbf{H}_Y^{\mathrm{T}} f_{\mathrm{Y}} + \mathbf{H}_\theta^{\mathrm{T}} m)\mathrm{d}S. \tag{4.64}$$

Equation (4.64) is nonlinear with respect to the discrete unknowns, and the Newton-Raphson method (Torkamani & Sonmez, 2008) is used to solve it in this study. To this end, the derivatives of $\mathbf{\Phi}$ and $\mathbf{p}$ with respect to the components of $\mathbf{U}$ must be determined. This task is carried out using symbolic computing capabilities of available commercial software.

4.4 Numerical examples

The proposed Euler-Bernoulli beam element is validated by solving five beam problems, each involving large and complex deformations. These examples utilize prismatic beams with rectangular cross-sections, where b and h represent the width and height of the cross-section, respectively. In addition, E denotes Young's modulus, and $I = bh^3/12$ is the cross-sectional moment of inertia. To thoroughly assess the efficiency of the varying-weight concept, the performances of the proposed varying-weight element are rigorously compared with those of the constant-weight element. Specifically, three models—VW, CW1, and CW2—are employed for each problem. Model VW uses the minimum number of varying-weight elements necessary to yield accurate solutions, while model CW1 employs constant-weight elements with a comparable number of DOFs to VW. As CW1 for each problem consistently exhibits lower accuracy than VW, the number of employed constant-weight elements is increased from CW1 until the solution attains the accuracy level of VW. The resulting model is referred to as CW2. The details of the models for the five problems are shown in Table 4.1, while the assessments specific to each problem are presented in a separate subsection. In the first problem, the reference solutions are obtained analytically, while the reference solutions in the other problems are converged solutions obtained using fine meshes of the planar curved Euler-Bernoulli beam element proposed in the study of Vo and Nanakorn (2020).

Table 4.1 Model details.

Problem	No. of elements (No. of DOFs)			DOF ratio of CW2 /VW
	VW	CW1	CW2	
4.4.1 – A circular arch under a uniformly distributed moment	7 (49)	10 (50)	28 (140)	2.9
4.4.2 – A spiral beam under an end moment	17 (119)	24 (120)	54 (270)	2.3
4.4.3 – A curved spring in compression	14 (98)	20 (100)	50 (250)	2.6
4.4.4 – A wheel with curved spokes under equidistant concentrated rim loads	32 (212)	48 (228)	120 (588)	2.8
4.4.5 – An S-shaped beam under equal end moments	16 (111)	23 (114)	59 (294)	2.6

4.4.1 A circular arch under a uniformly distributed moment

The first problem involves a cantilever circular arch subjected to a uniformly distributed moment m applied along its entire length $L = \pi R/2$, where R is the radius of the arch depicted in Figure 4.4. Analytical solutions for the problem can be obtained and serve as reference solutions.

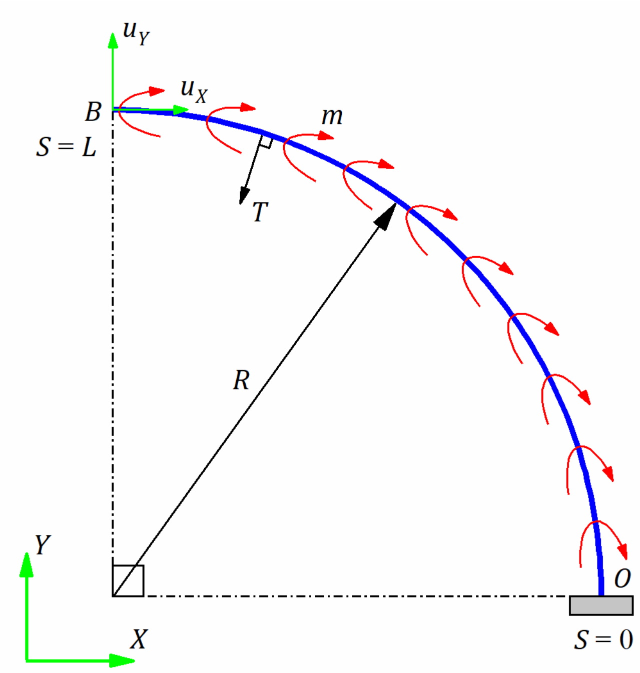

Figure 4.4 Problem 4.4.1: A circular arch under a uniformly distributed moment.

Define α as

$$\alpha(S) = \int_0^S k(S)\mathrm{d}S = \int_0^S \frac{(k_0 + K_{11})}{a_1}\mathrm{d}S = \int_0^S \frac{(1/R + K_{11})}{a_1}\mathrm{d}S \tag{4.65}$$

where S denotes the arc-length variable, starting at the support O. Here, $\alpha(S)$ represents the angle between the unit tangent vectors at $S = 0$ and at S. Note that the unit tangent vector at $S = 0$ is a vertical vector pointing in the positive Y direction. Since the problem involves pure bending, the beam's length L remains unchanged during deformation, i.e., $a_1 = 1$. Additionally, K_{11} is determined from the internal resultant moment M^{11} via Equation (4.40) as

$$K_{11} = -\frac{m(L-S)}{EI}. \tag{4.66}$$

Subsequently, Equation (4.65) can be expressed as

$$\alpha(S) = \int_0^S \left(\frac{1}{R} - \frac{m(L-S)}{EI}\right) \mathrm{d}S = \frac{S}{R} - \frac{m(LS - S^2/2)}{EI}. \tag{4.67}$$

The coordinates of the deformed beam axis can then be calculated as

$$x(S) = x_O - \int_0^S \sin\alpha \, \mathrm{d}S \qquad\qquad y(S) = y_O + \int_0^S \cos\alpha \, \mathrm{d}S \tag{4.68}$$

where (x_O, y_O) represents the coordinates of the beam axis at O in Figure 4.4. Figure 4.5 illustrates the deformed configurations at various magnitudes of m, obtained from Equation (4.68). The arch experiences significant displacements and transforms into a spiral-like configuration when $m = 6\pi EI/L^2$, at which point the cross-section at the free end rotates by an angle of 3π.

The X and Y displacements of the beam axis can be obtained from the coordinates of the initial and deformed beam axes. Let $X(S)$ and $Y(S)$ denote the coordinates of the initial beam axis, and let $u_{0X}(S)$ and $u_{0Y}(S)$ represent the displacements in the X and Y directions, respectively. The translational displacements of the beam axis, normalized by the beam length L, are given by

$$\frac{u_{0X}(S)}{L} = \frac{x(S) - X(S)}{L} \qquad\qquad \frac{u_{0Y}(S)}{L} = \frac{y(S) - Y(S)}{L}. \tag{4.69}$$

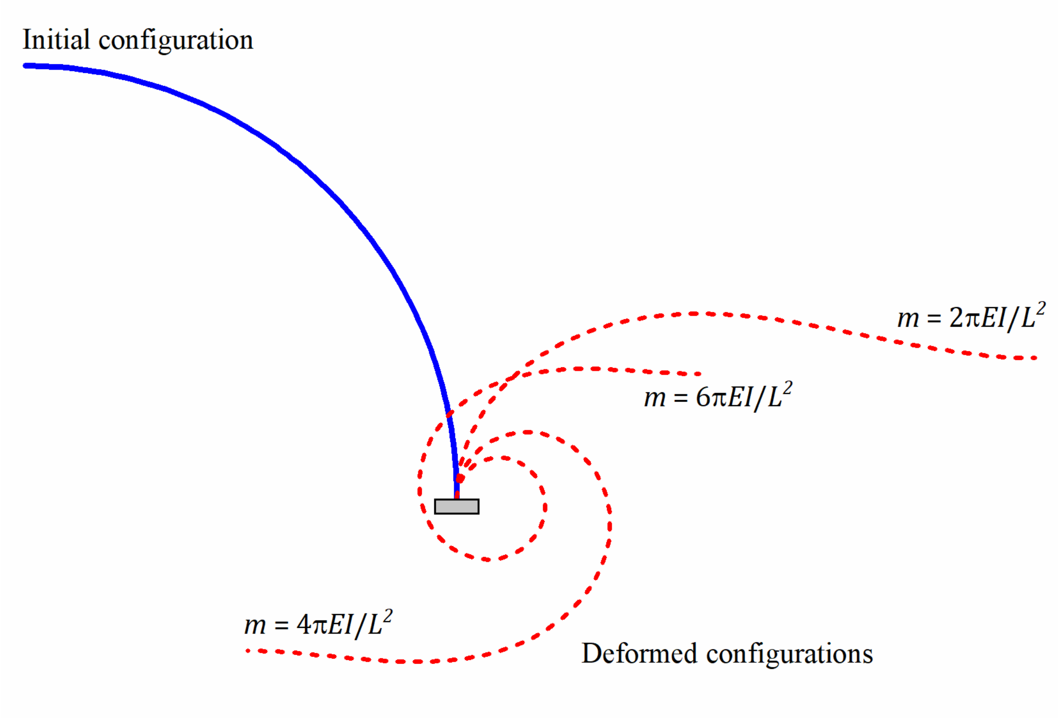

Figure 4.5 Problem 4.4.1: Analytical deformed configurations at various magnitudes of the applied moment m.

For the numerical analysis, the cross-sectional height h is set to $0.01R$. Figure 4.6 presents the normalized translational displacements at the free end B, i.e., $u_{0X,B}/L$ and $u_{0Y,B}/L$. From the magnified figures within Figure 4.6, it can be seen that model VW yields noticeably better results than CW1. As mentioned earlier, VW and CW1 employ approximately the same number of DOFs, as shown in Table 4.1. The number of employed constant-weight elements is increased from CW1 until the solution attains the accuracy level of VW, resulting in model CW2. The results in Table 4.1 show that CW2 requires about three times the DOFs of VW for a comparable level of accuracy. Figure 4.7 shows the analytical deformed beam axis at $m = 6\pi EI/L^2$ as well as those from the three models. The figure illustrates the clear difference in the deformed beam axes between VW and CW1. As CW2 is designed to achieve accuracy comparable to VW, the deformed beam axes from VW and CW2 are visually indistinguishable. More importantly, they also excellently match the analytical one.

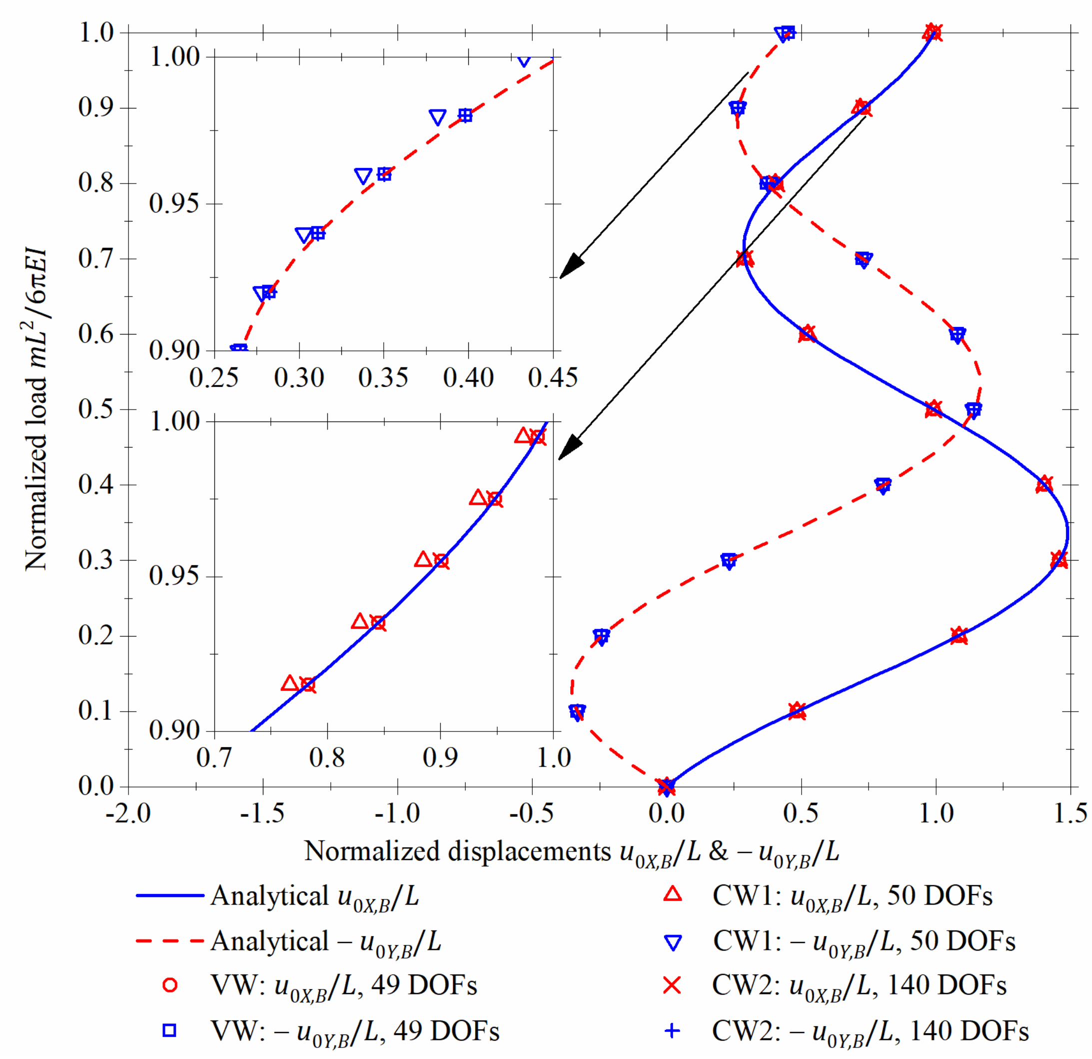

Figure 4.6 Problem 4.4.1: Normalized load-displacement curves for the displacements at the free end B.

Furthermore, Γ_{11} and K_{11} at $m = 6\pi EI/L^2$, obtained using these three models, are compared with the analytical solutions in Figure 4.8. The values of Γ_{11} and K_{11} from the three models are calculated at the Gauss points for numerical integration, while the exact K_{11} is obtained from Equation (4.66) and the exact Γ_{11} is equal to zero due to pure bending. Evidently, Γ_{11} and K_{11} given by model VW are very accurate compared to the analytical solutions. In contrast, model CW2 provides rather accurate K_{11} but quite inaccurate Γ_{11}, while CW1 yields significantly inaccurate Γ_{11} and K_{11}.

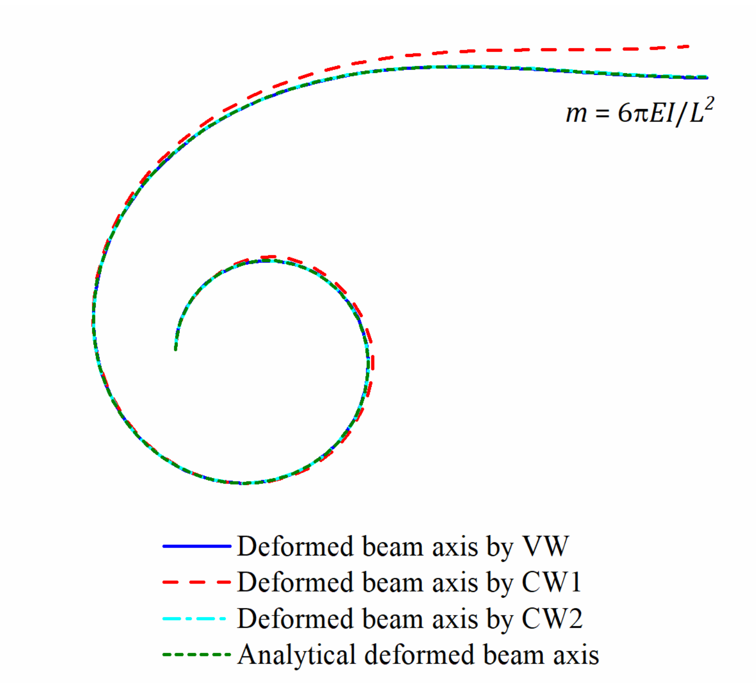

Figure 4.7 Problem 4.4.1: Deformed configurations at $m = 6\pi EI/L^2$.

Another accuracy assessment involves the convergence of solutions at $m = 6\pi EI/L^2$ with respect to the number of DOFs. To this end, the relative error representing the difference between the obtained and reference deformed beam axes is defined as

$$\text{Relative error} = \sqrt{\frac{\int_0^L \left(\mathbf{r}_{0,num} - \mathbf{r}_{0,ref}\right)^2 \mathrm{d}S}{\int_0^L \left(\mathbf{r}_{0,ref}\right)^2 \mathrm{d}S}}. \tag{4.70}$$

Here, $\mathbf{r}_{0,num}$ denotes the final deformed beam axis at $m = 6\pi EI/L^2$ obtained from either the varying-weight element or the constant-weight element, while $\mathbf{r}_{0,ref}$ is the reference final deformed beam axis, obtained analytically from Equation (4.68).

Figure 4.9 shows that the varying-weight element consistently achieves smaller relative errors compared to the constant-weight element. Initially, the order of convergence for the varying-weight element is significantly higher than that of the constant-weight element, with values of 10.5 versus 3. However, towards the end of the

DOF range, the order of convergence for the varying-weight element becomes slightly lower than that of the constant-weight element, showing values of 3.5 versus 4. Nonetheless, the varying-weight element maintains its superiority in accuracy throughout.

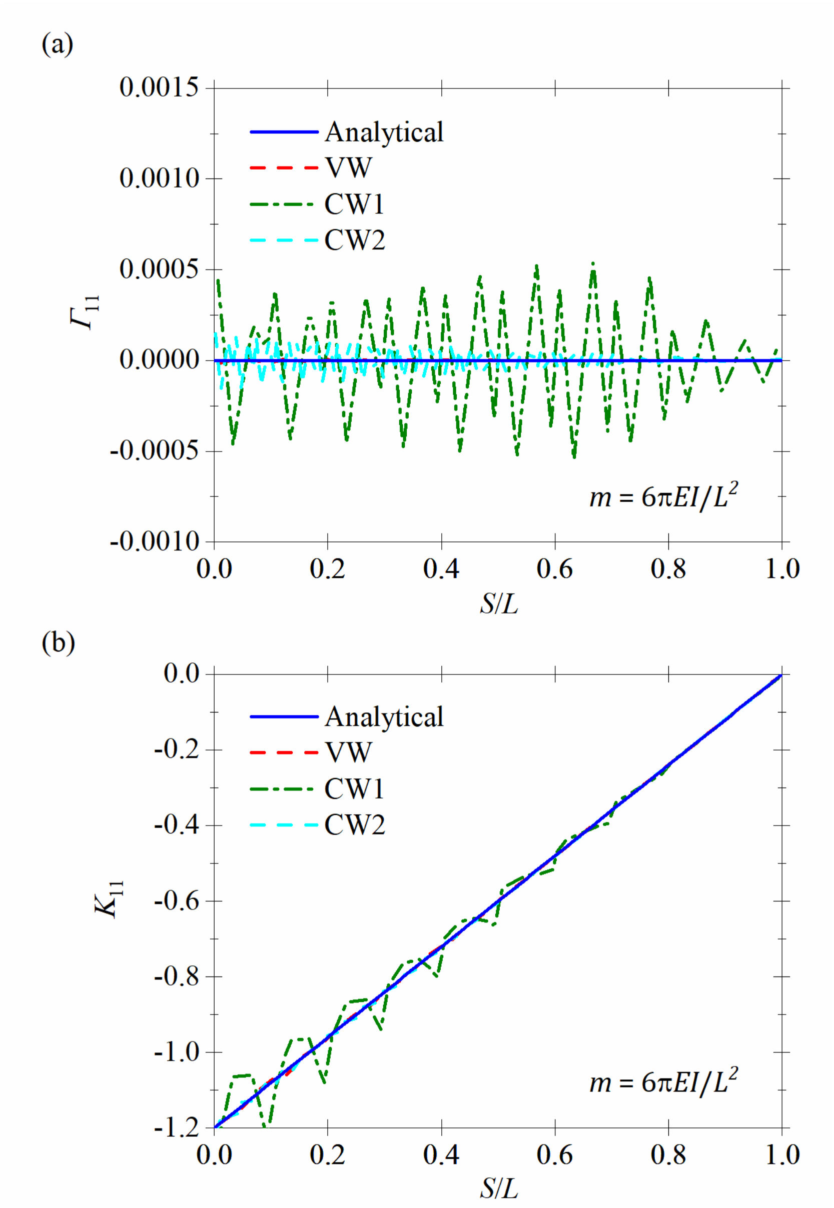

Figure 4.8 Problem 4.4.1: Γ_{11} and K_{11} at $m = 6\pi EI/L^2$.

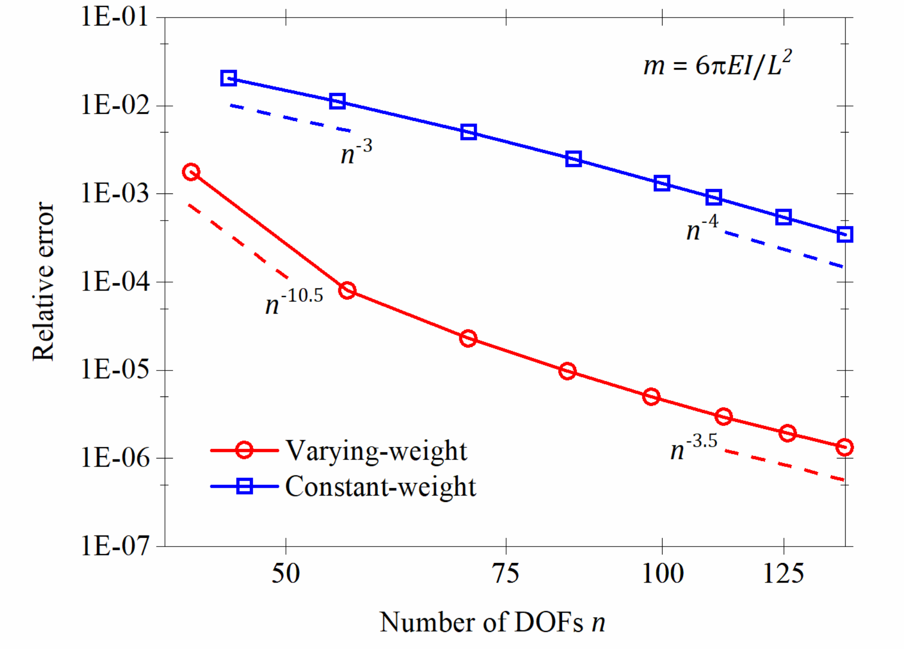

Figure 4.9 Problem 4.4.1: Convergence with respect to DOFs at $m = 6\pi EI/L^2$.

Locking effects are common challenges in thin beam analyses, where the computed stiffness of a beam exceeds its actual stiffness, resulting in reduced displacements with significant inaccuracies. Various techniques, including reduced integration methods, $\overline{\mathrm{B}}$ projection methods, and discrete strain gap methods, have been employed to mitigate this issue (Koschnick, Bischoff, Camprubí & Bletzinger, 2005; Miao, Borden, Scott & Thomas, 2018; Noor & Peters, 1981; Stolarski & Belytschko, 1982). However, these approaches often involve additional complex and expensive procedures. Therefore, there is increasing interest in elements that are inherently free from locking effects. As demonstrated in this problem, the proposed varying-weight element belongs to this category of elements.

Locking effects are examined in this problem using the results of convergence tests with respect to the number of DOFs for three thickness values, i.e., $h/R = 0.01$, 0.001, and 0.0001, representing a very thin beam to an extremely thin beam. The convergence results from the varying-weight element in Figure 4.10a for these three thickness values are virtually overlapping, demonstrating no accuracy loss with the decrease in thickness and, therefore, no sign of locking effects. In contrast, in Figure 4.10b, the constant-weight element exhibits slight differences between the convergence results for the difference thickness values. Specifically, smaller ratios of h/R result in larger relative errors, demonstrating accuracy losses due to the decrease in thickness. This behavior of the constant-weight element indicates that it suffers from locking effects, although the observed effect is insignificant.

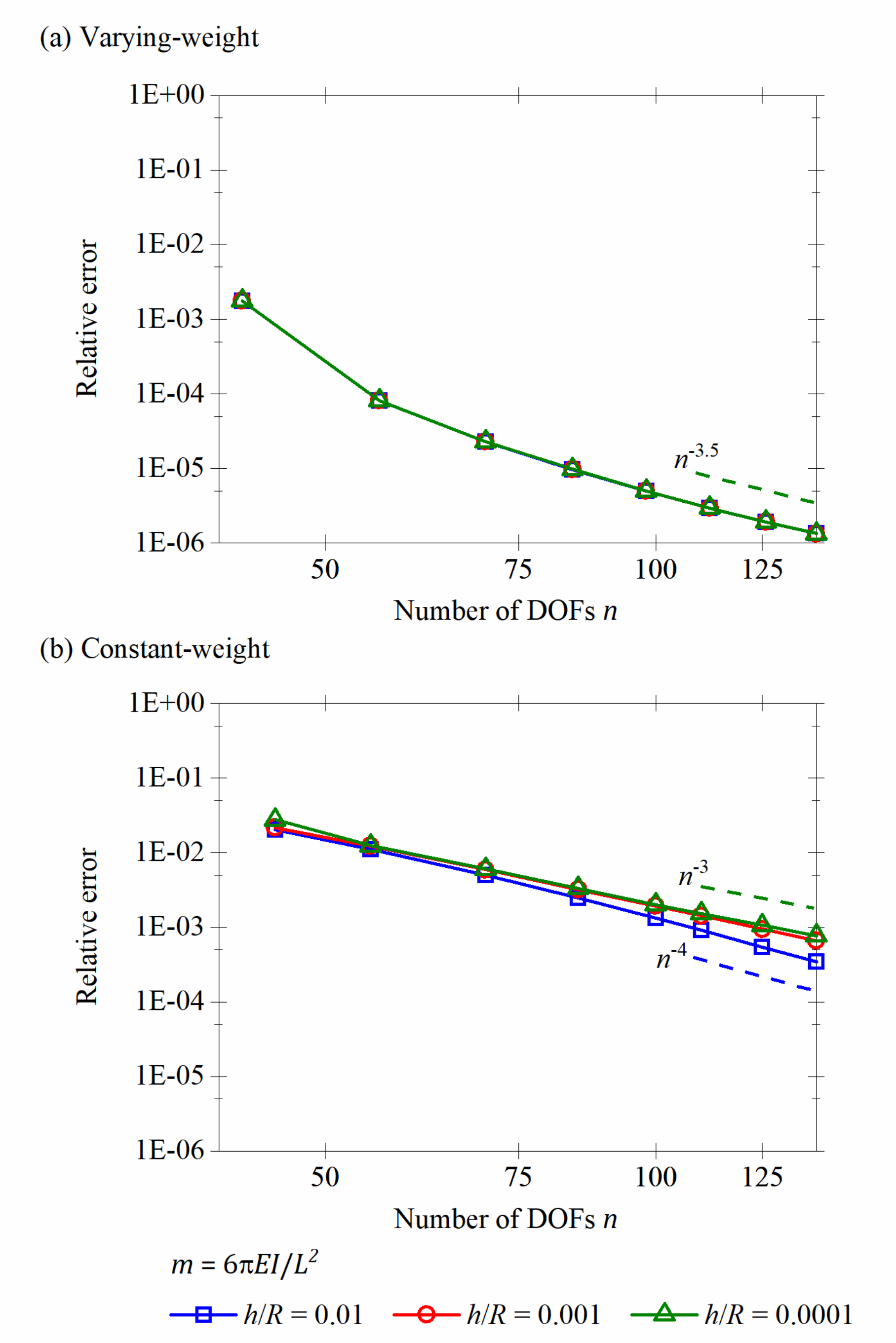

Figure 4.10 Problem 4.4.1: Convergence with respect to DOFs at $m = 6\pi EI/L^2$, for different thickness values: (a) the varying-weight element and (b) the constant-weight element.

4.4.2 A spiral beam under an end moment

The second problem concerns a cantilever beam with a spiral shape subjected to a concentrated moment M at its free end, as described in Figure 4.11. The initial beam axis of the spiral is mathematically defined by the following equations as

$$X(\varphi) = R(1+\varphi)\cos\varphi \qquad\qquad Y(\varphi) = R(1+\varphi)\sin\varphi. \tag{4.71}$$

Here, φ spans the range $[0, 4\pi]$, indicating two turns of the initial axis. It can be clearly seen that the initial beam axis has non-uniform curvature. The cross-sectional height h is set to $0.1R$.

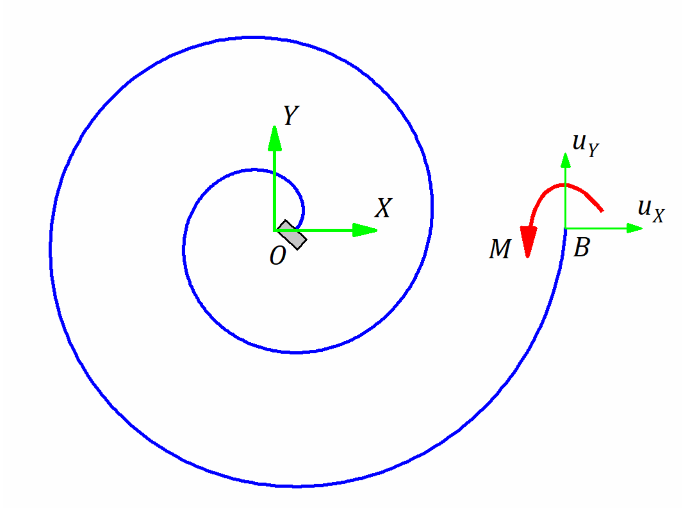

Figure 4.11 Problem 4.4.2: A spiral beam under an end moment.

The accuracy performance of the two elements is evaluated using the displacements at the free end B, denoted as $u_{0X,B}$ and $u_{0Y,B}$, with the three models, VW, CW1, and CW2, detailed in Table 4.1. As mentioned earlier, for this problem, the reference solutions for the two displacements are converged solutions obtained using a fine mesh of the planar curved Euler-Bernoulli beam element proposed by Vo and Nanakorn (2020). Specifically, 1,000 DOFs are used to obtain the reference solutions. Figure 4.12 shows the normalized load-displacement curves for $u_{0X,B}$ and $u_{0Y,B}$ obtained from the three models, with comparisons to the reference solutions. Through the magnified figures in Figure 4.12, it can be seen again that VW yields much better results than CW1 when compared to the reference solutions, although they employ approximately the same numbers of DOFs. In contrast, as shown in Table 4.1, CW2 requires more than twice the number of DOFs as VW to achieve the same accuracy level. Figure 4.13 presents the deformed configurations at $M = 0.15EI/R$ from the three model as well as the reference model. The deformed axes by VW and CW2 closely match the reference, while that by CW1 exhibits noticeable deviation. As shown in Figure 4.13a, at $M = 0.15EI/R$, the deformed configuration is very different from the initial one.

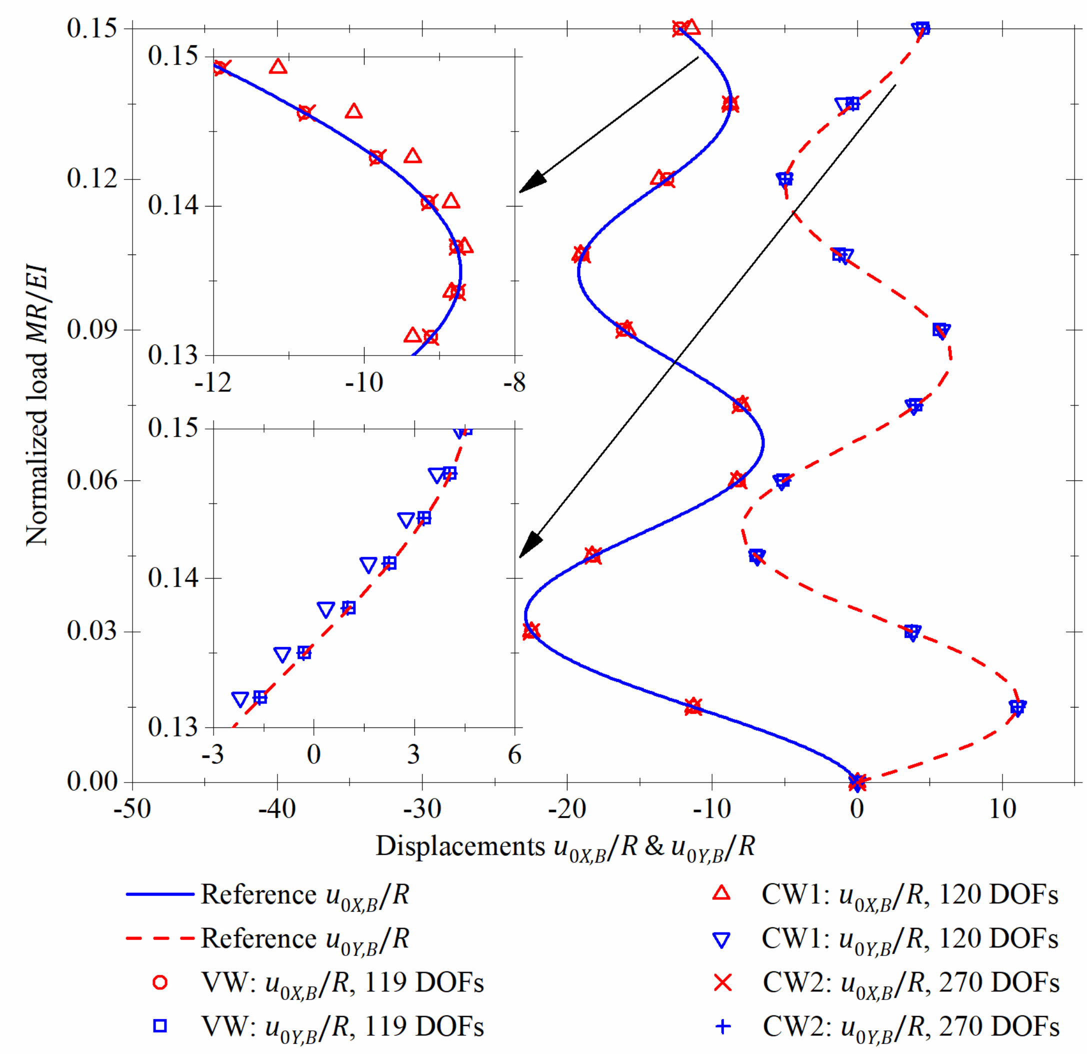

Figure 4.12 Problem 4.4.2: Normalized load-displacement curves for the displacements at the free end B.

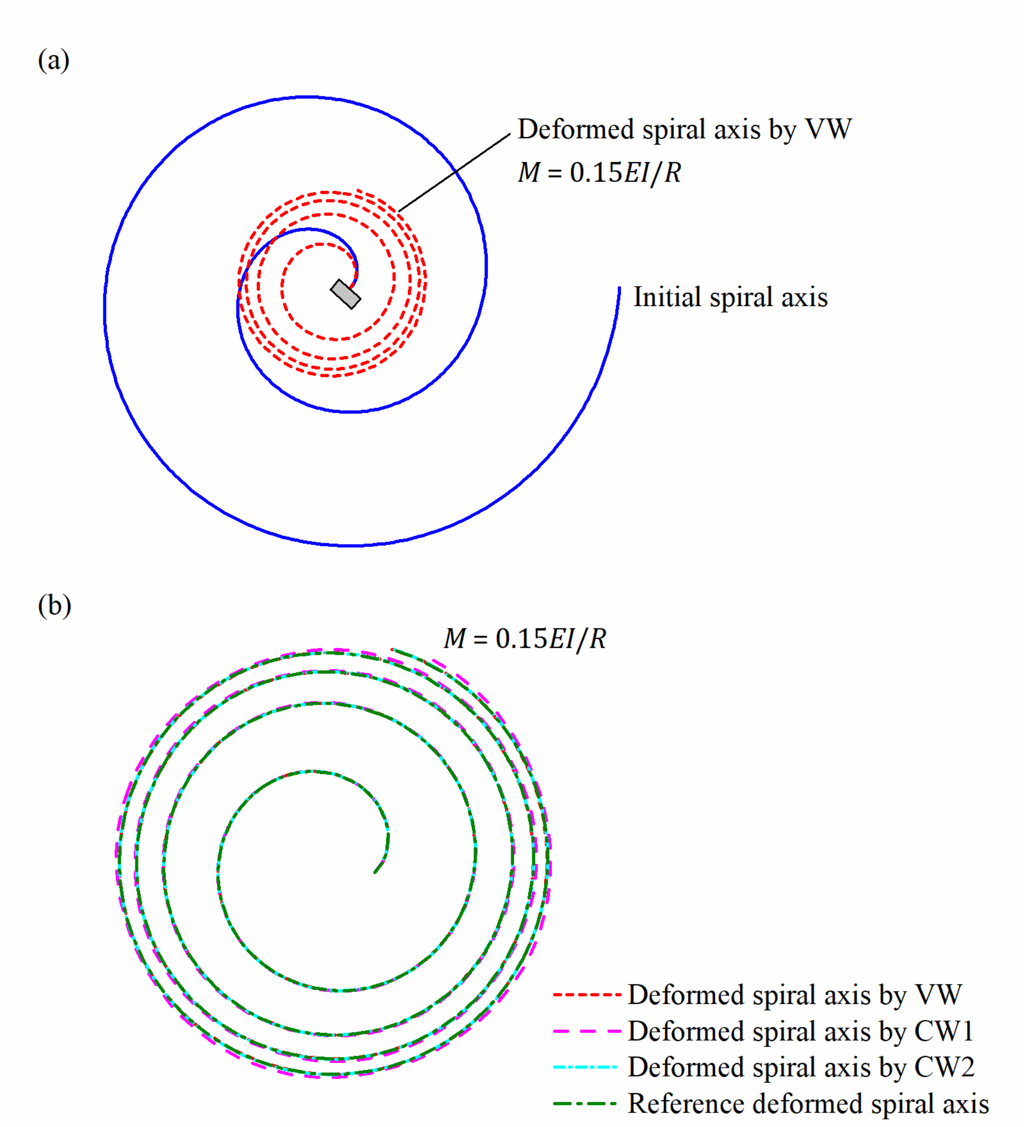

Figure 4.13 Problem 4.4.2: Deformed configurations at $M = 0.15EI/R$.

Locking effects in this problem are examined by considering the final deformed spiral axes at $M = 0.15EI/R$. For a fair comparison between the varying-weight and constant-weight elements, models VW and CW1 are used due to their similar numbers of DOFs. For each model, the problem is solved with three thickness values, i.e., $h/R = 0.1$, 0.01, and 0.001, representing a very thin beam to an extremely thin beam. The obtained deformed spiral axes are shown in Figure 4.14. Note that the applied moment $M = 0.15EI/R$ is a normalized value that yields the same displacements for different values of h/R. Figure 4.14 shows that the solutions obtained from both models VW and CW1 for the three thickness values virtually do not vary with the thickness. Therefore, for this problem, both the varying-weight and constant-weight elements do not exhibit any locking effect.

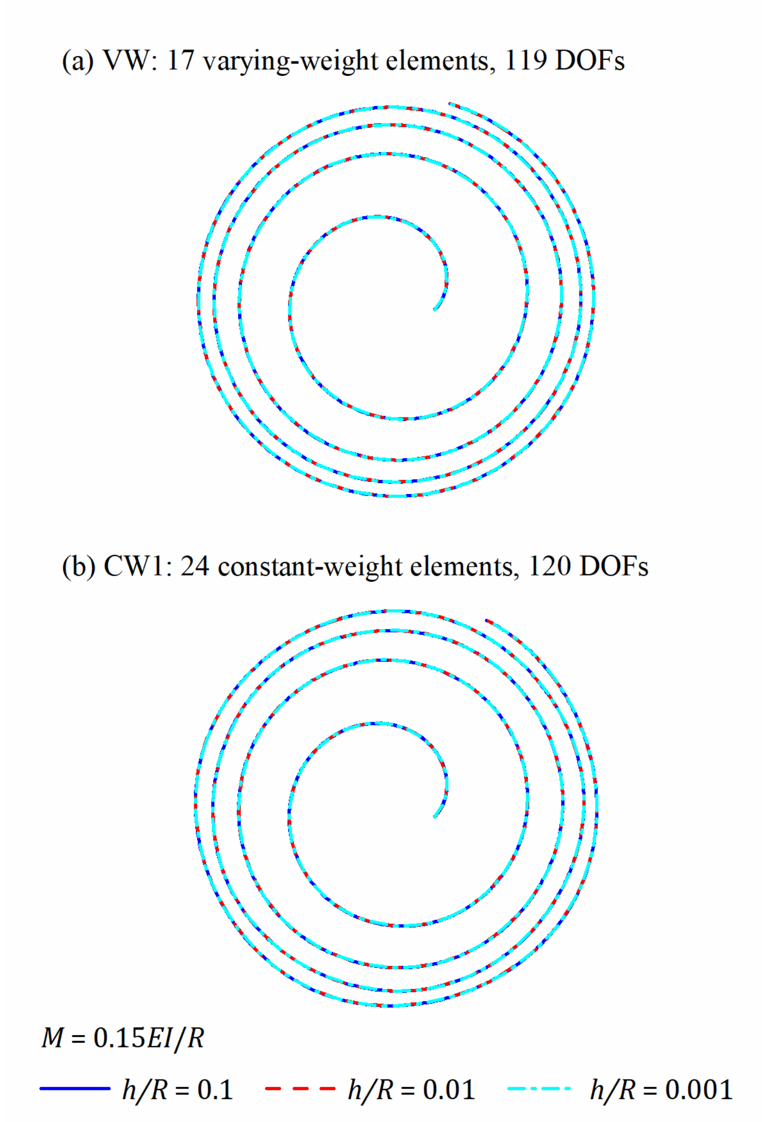

Figure 4.14 Problem 4.4.2: Deformed configurations at $M = 0.15EI/R$, for different thickness values: (a) VW and (b) CW1.

4.4.3 A curved spring in compression

This problem focuses on the behavior of a curved plane spring under compression, particularly exploring its buckling behavior through geometrically nonlinear analysis. The problem description is presented in Figure 4.15, and the length of the spring can be determined as $L = 46\pi R/3$. Additionally, the cross-sectional height h is set equal to $0.1R$.

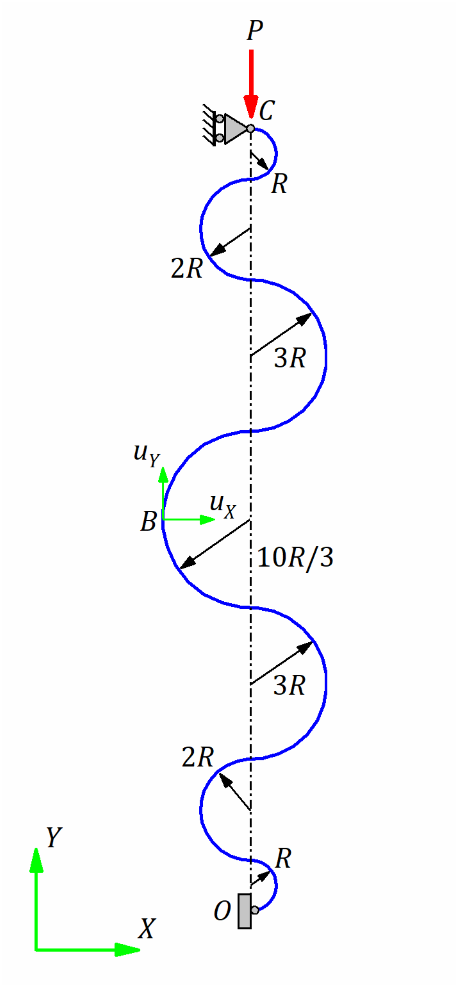

Figure 4.15 Problem 4.4.3: A curved spring in compression.

Figure 4.16 illustrates the normalized load-displacement curves for the displacements of the spring axis at point B, denoted by $u_{0X,B}$ and $u_{0Y,B}$. The curves are obtained from the three models, with comparisons to the reference solutions. For this problem, the reference solutions are obtained using the planar curved Euler-Bernoulli beam element proposed in Vo and Nanakorn (2020) with 1,050 DOFs. From the magnified figures in Figure 4.16, it can be seen that VW yields much more accurate solutions than CW1 when compared to the reference solutions. In contrast, as shown in Table 4.1, CW2 requires 2.6 times the number of DOFs as VW to achieve the same accuracy level.

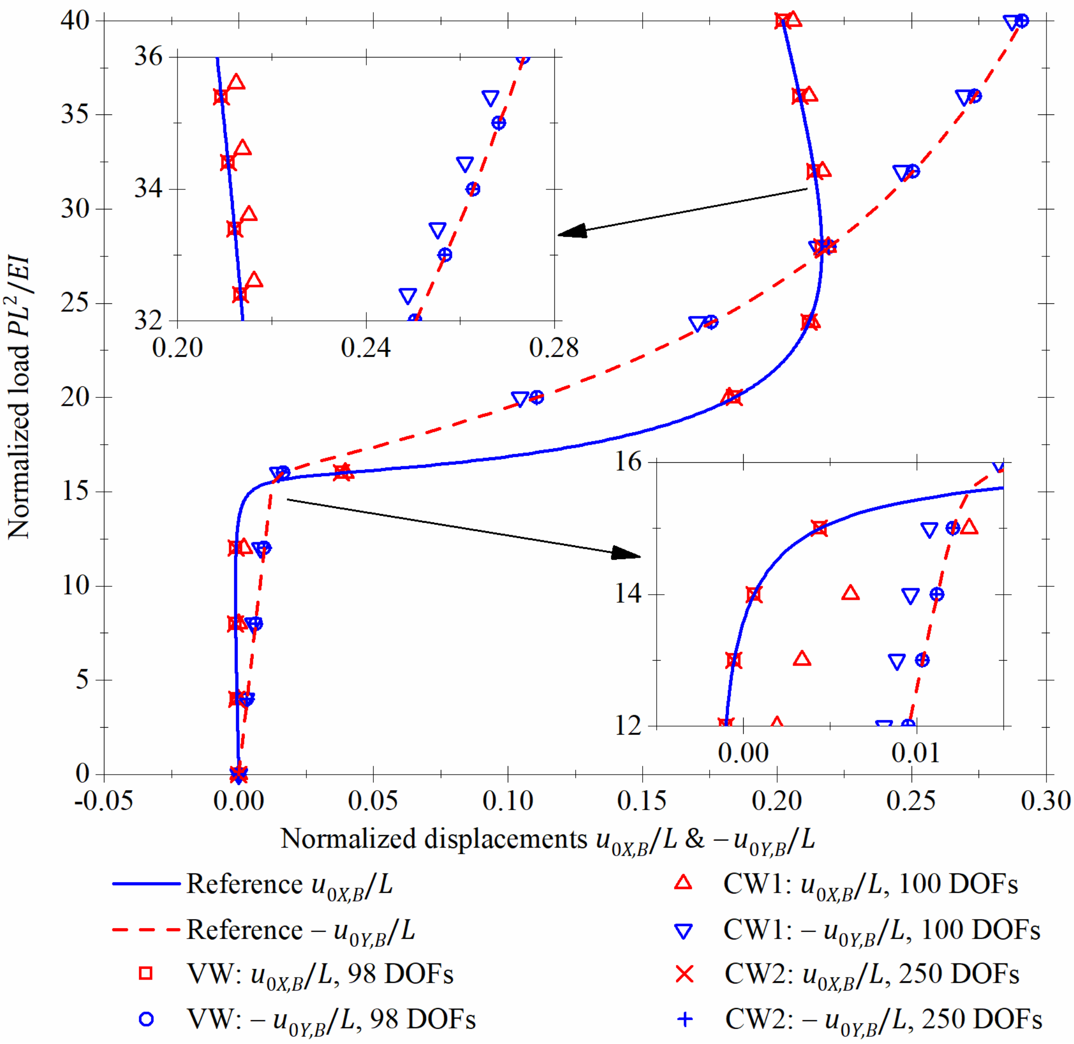

Figure 4.16 Problem 4.4.3: Normalized load-displacement curves for the displacements at point B.

Figure 4.17 shows the deformed configurations of the spring at various magnitudes of the applied force P, obtained using VW. In Figure 4.17a-c, where P is between $5EI/L^2$ and $15EI/L^2$, the spring undergoes approximately linear deformations with insignificant lateral displacements, as shown in Figure 4.16. However, in Figure 4.17d-f, where P is larger and between $20EI/L^2$ and $40EI/L^2$, significant lateral and vertical displacements occur, as evident in Figure 4.16. The behavior shown in Figure 4.16 and Figure 4.17 indicates that the spring reaches its buckling load and becomes unstable between $15EI/L^2$ and $20EI/L^2$. Figure 4.18 shows the deformed configurations at $P = 40EI/L^2$, where the inaccuracy of model CW1 is noticeable.

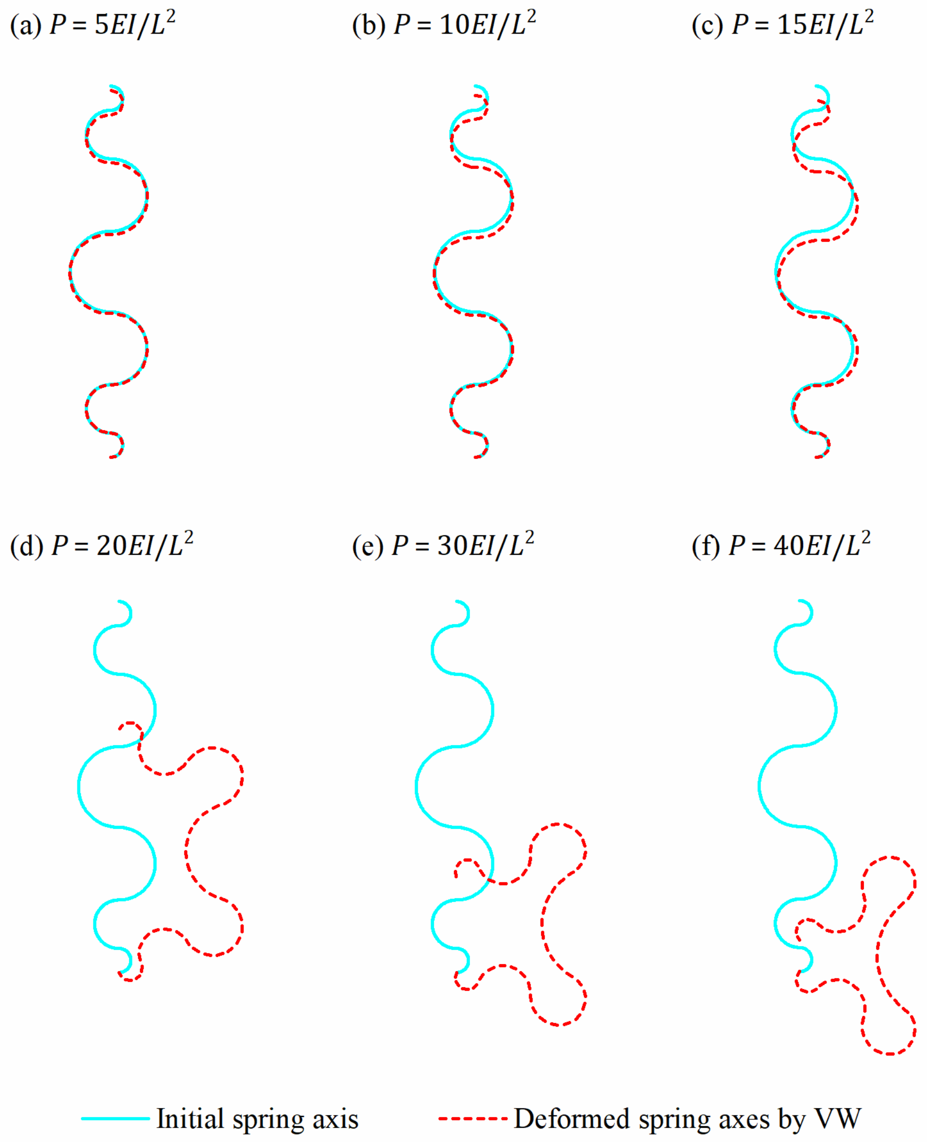

Figure 4.17 Problem 4.4.3: Deformed configurations at various magnitudes of the applied force P.

Figure 4.19 shows the deformed configurations at $P = 40EI/L^2$, obtained from VW and CW1 for three different thickness values, i.e., $h/R = 0.1$, 0.01, and 0.001, representing a very thin beam to an extremely thin beam. Similar to the previous problem, the applied force $P = 40EI/L^2$ is a normalized value that yields the same displacements for different values of h/R. It can be seen from the figure that neither the varying-weight element nor the constant-weight element exhibits locking effects as their results virtually do not vary with the thickness.

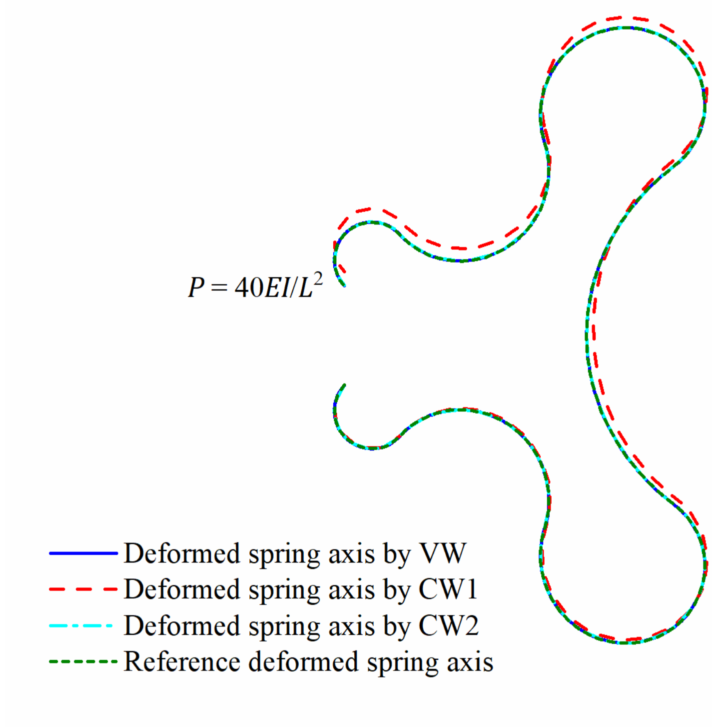

Figure 4.18 Problem 4.4.3: Deformed configurations at $P = 40EI/L^2$.

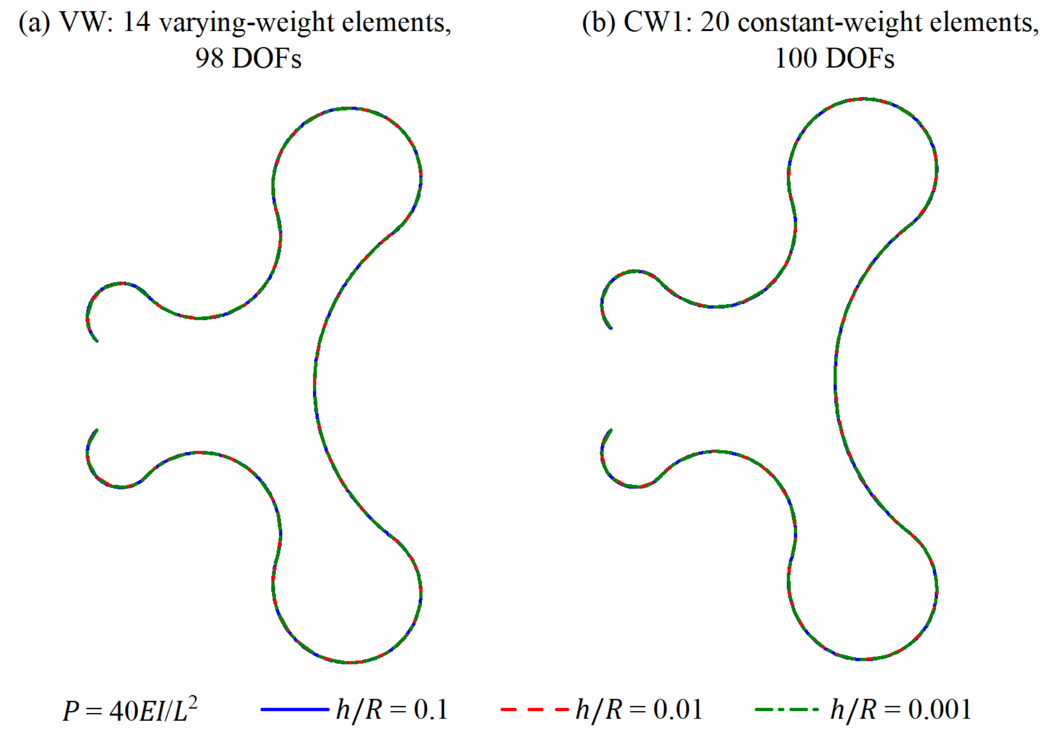

Figure 4.19 Problem 4.4.3: Deformed configurations at $P = 40EI/L^2$, for different thickness values: (a) VW and (b) CW1.

4.4.4 A wheel with curved spokes under equidistant concentrated rim loads

A wheel of radius R in Figure 4.20 is analyzed. The wheel has four curved spokes, each a half-circle with a radius of $R/2$, and is subjected to compression from two pairs of concentrated force P. The center of the wheel serves as a fixed support. The cross-sectional height h is set equal to $0.01R$ for all the members.

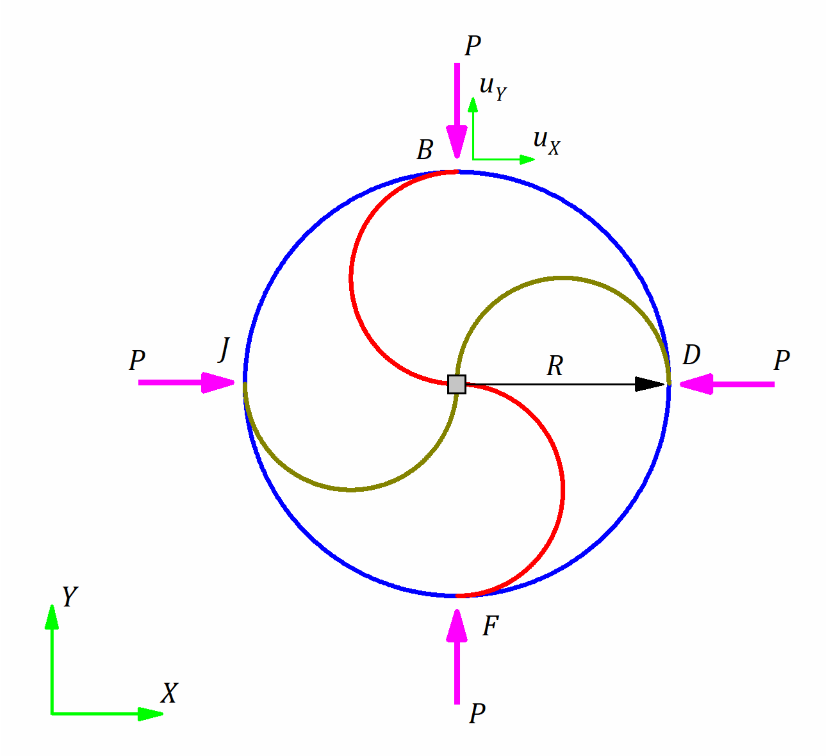

Figure 4.20 Problem 4.4.4: A wheel with curved spokes under equidistant concentrated rim loads.

Figure 4.21 displays the normalized load-displacement curves for the displacements at point B, denoted by $u_{0X,B}$ and $u_{0Y,B}$. The reference solutions in the figure are obtained using the planar curved Euler-Bernoulli beam element proposed in Vo and Nanakorn (2020) with 1,088 DOFs. It can be seen from the figure again that the varying-weight element noticeably outperforms the constant-weight element. As indicated in Table 4.1, CW2 requires nearly three times as many DOFs as VW to achieve the same level of accuracy. In Figure 4.22, the deformed configurations at $P = 7EI/R^2$ are shown for the three models as well as the reference model. The deformed shapes by VW and CW2 closely match the reference results, whereas the configuration from CW1 exhibits noticeable deviation. As shown in Figure 4.22a, at $P = 7EI/R^2$, the deformed shape is markedly different from the initial one.

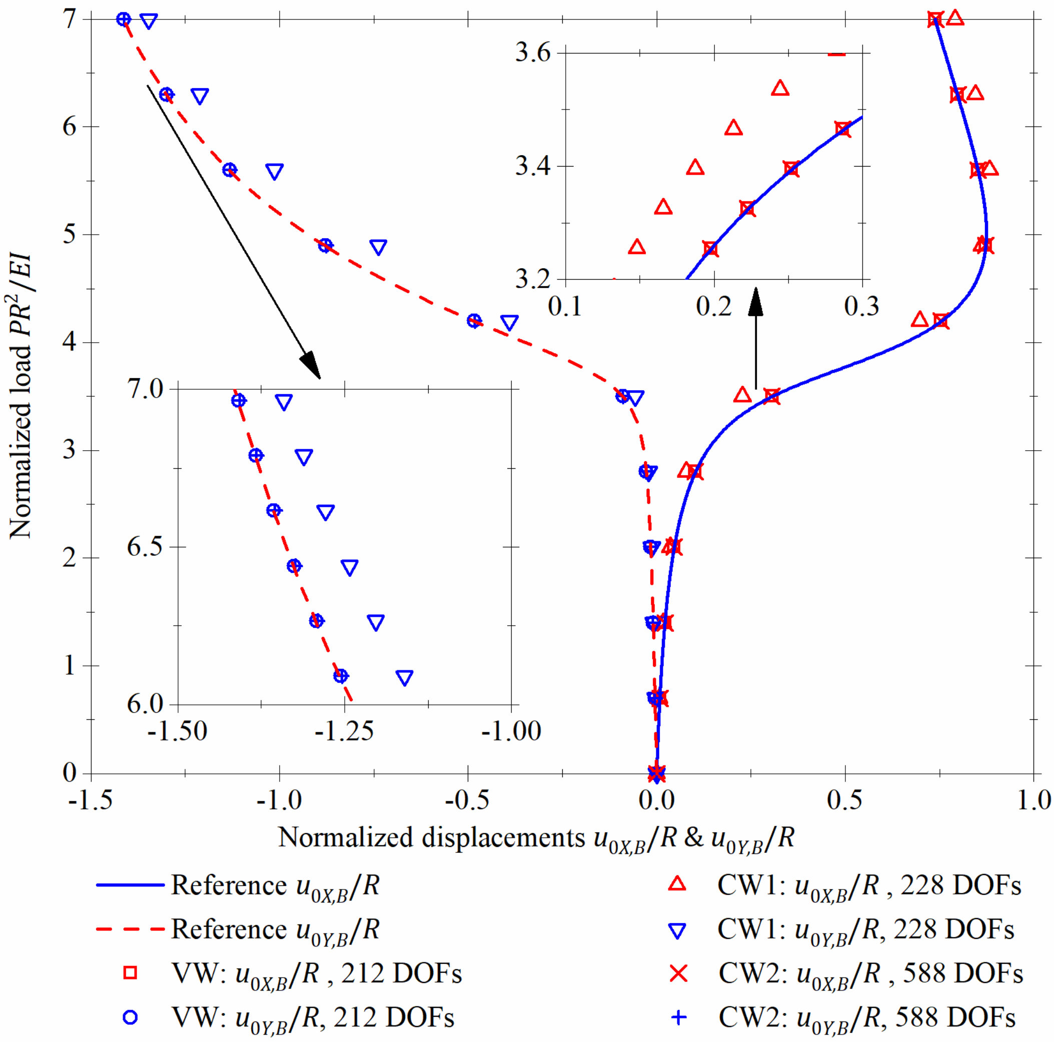

Figure 4.21 Problem 4.4.4: Normalized load-displacement curves for the displacements at point B.

For the locking investigation, the wheel is analyzed at $P = 7EI/R^2$ using VW and CW1 with three thickness values, i.e., $h/R = 0.01, 0.001, 0.0001$, representing a very thin beam to an extremely thin beam. The applied force $P = 7EI/R^2$ is a normalized value that yields the same displacements for different values of h/R. Figure 4.23 shows the deformed configurations at $P = 7EI/R^2$. The varying-weight element exhibits no locking effect, as indicated in Figure 4.23a, whereas the constant-weight element shows variation in the results for different h/R ratios, as indicated in Figure 4.23b, implying locking effects.

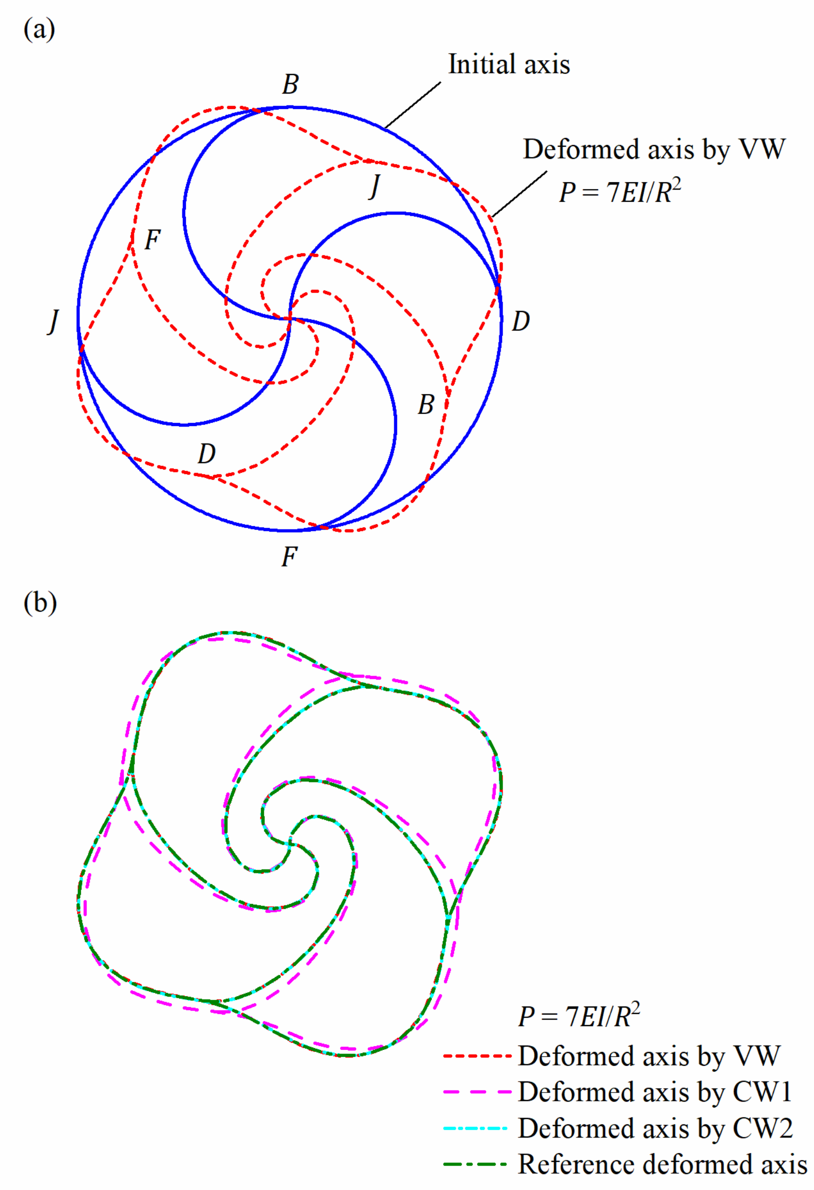

Figure 4.22 Problem 4.4.4: Deformed configurations at $P = 7EI/R^2$.

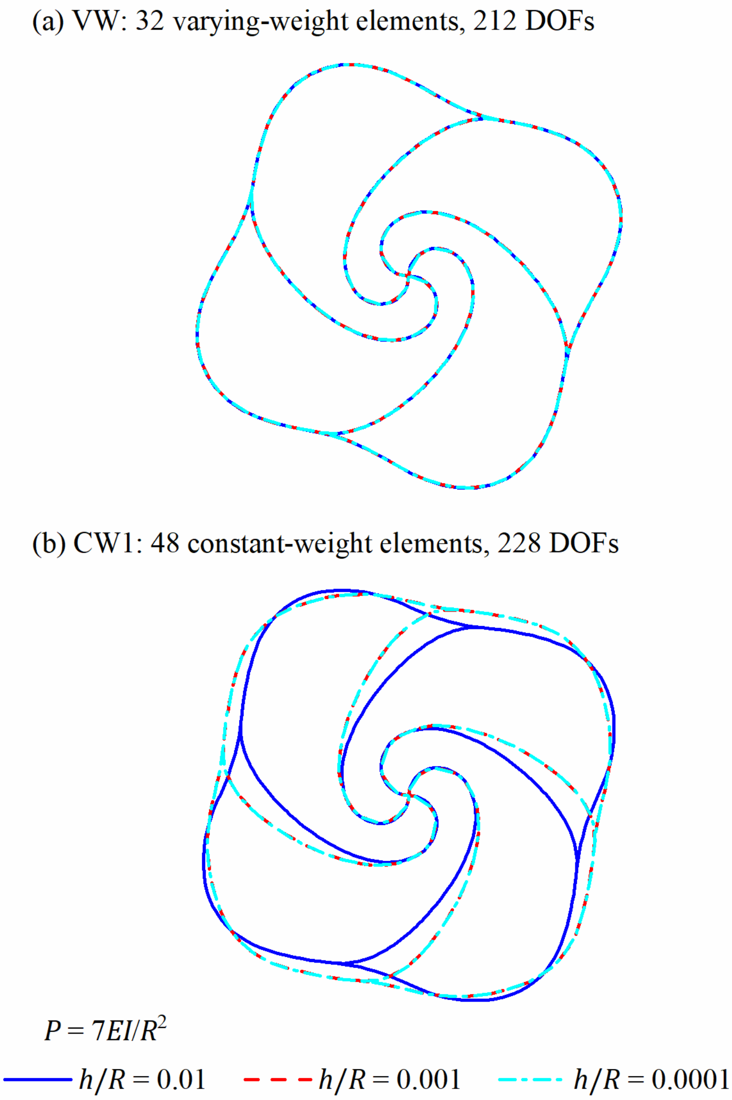

Figure 4.23 Problem 4.4.4: Deformed configurations at $P = 7EI/R^2$, for different thickness values: (a) VW and (b) CW1.

4.4.5 An S-shaped beam under equal end moments

Here, an S-shaped beam under equal end moments, as shown in Figure 4.24a, is analyzed. The beam has a pinned support at each end. At both ends of the beam, a concentrated moment M is applied in the same direction. The cross-sectional height h is set equal to $0.01R$. It can be deduced from the equilibrium and symmetry that the resultant moment and displacements at point C are zero. As a result, only the upper half of the beam, as shown in Figure 4.24b, is analyzed instead of the whole beam.

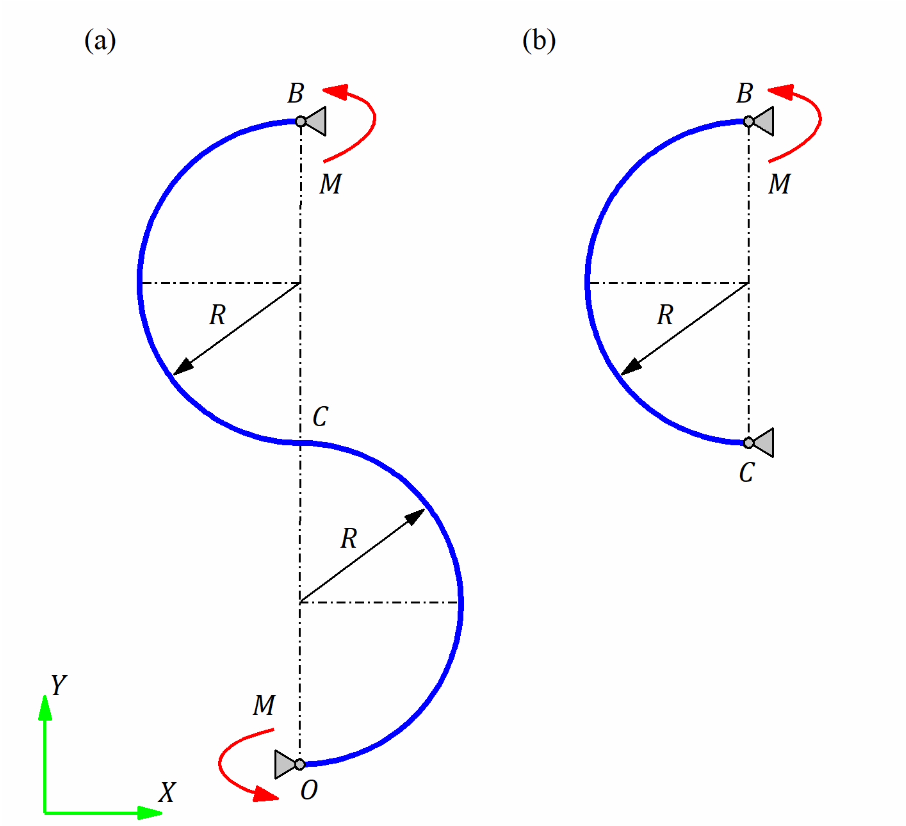

Figure 4.24 Problem 4.4.5: An S-shaped beam under equal end moments.

Figure 4.25 shows the normalized load-rotation curves for the cross-section rotation at point B, denoted by θ_B. The reference solution in the figure is obtained using the planar curved Euler-Bernoulli beam element proposed in Vo and Nanakorn (2020) with 999 DOFs. The beam exhibits highly complex snap behavior with multiple limit points. Figure 4.25, including its magnified details, confirms the superiority of the varying-weight element over the constant-weight element. According to Table 4.1, CW2 requires 2.6 times as many DOFs as VW to achieve the same level of accuracy. Figure 4.26 illustrates the deformed configurations at three limit points, specified in Figure 4.25, obtained by model VW, revealing significant changes from the initial S shape.

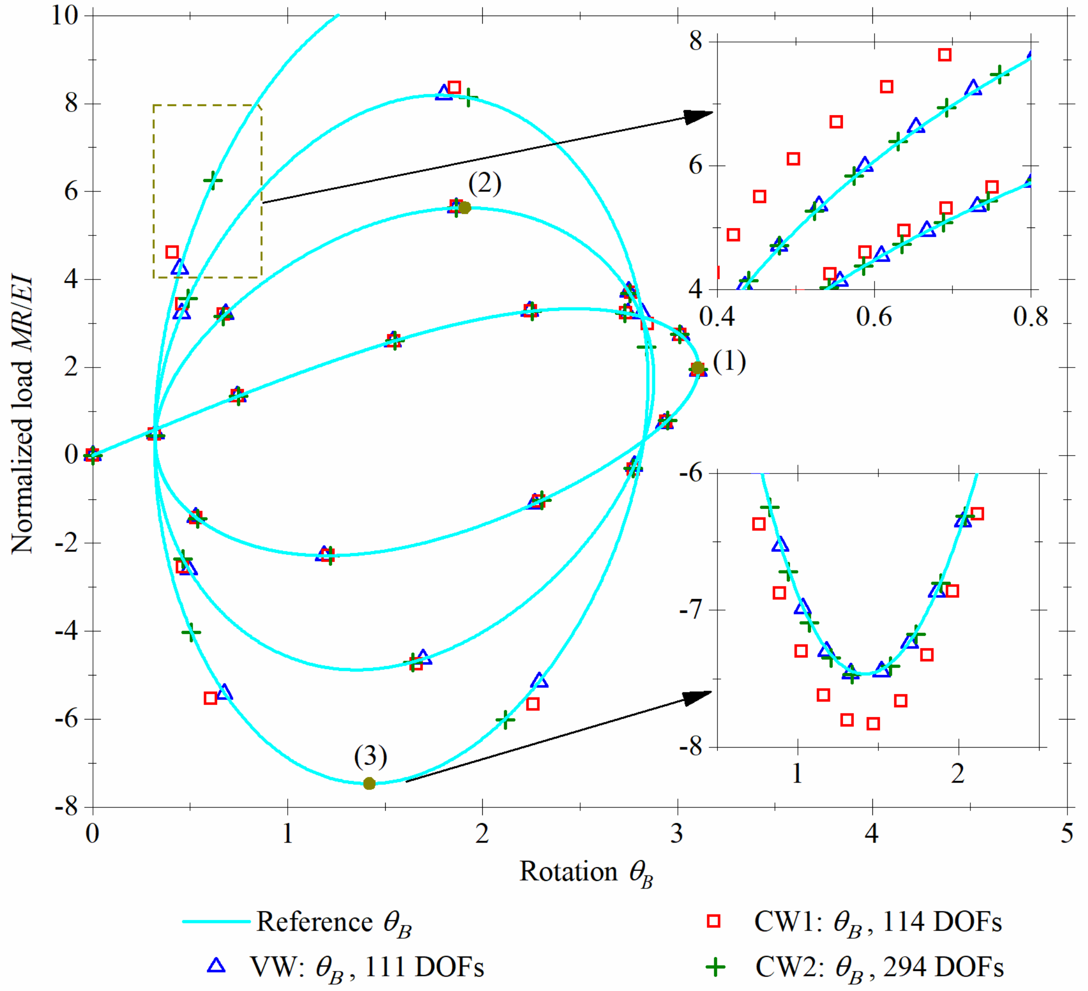

Figure 4.25 Problem 4.4.5: Normalized load-rotation curves for the rotation at point B.

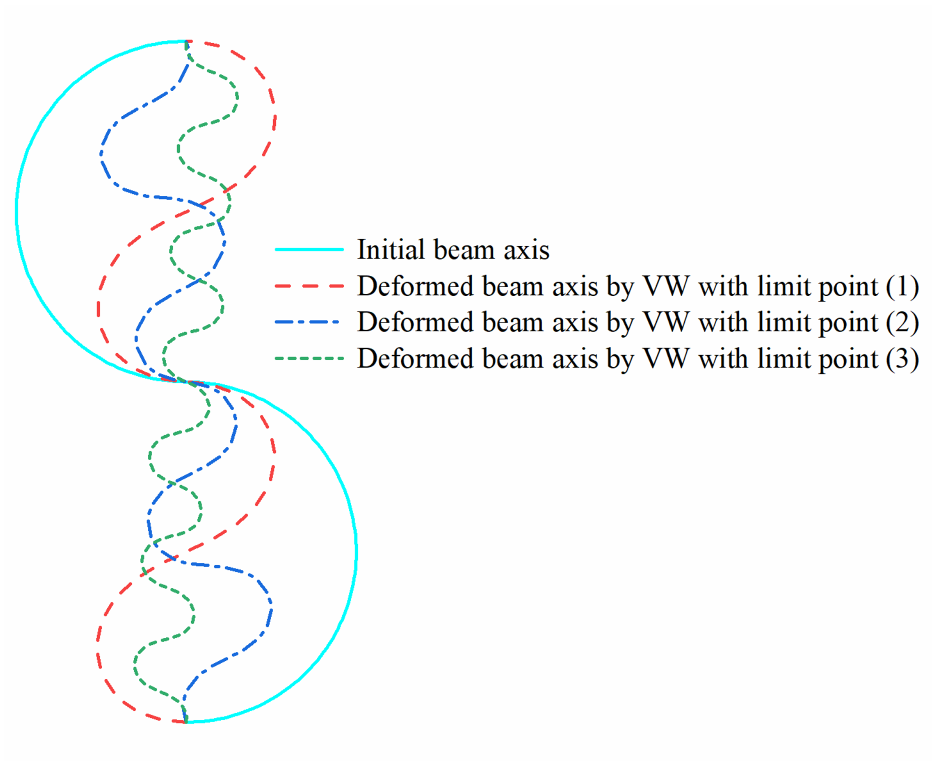

Figure 4.26 Problem 4.4.5: Deformed configurations at some limit points.

CHAPTER 5

PLANAR CURVED TIMOSHENKO-EHRENFEST BEAM ELEMENTS FOR LARGE-DISPLACEMENT AND SMALL-STRAIN ANALYSIS USING NURBS CURVES WITH VARYING WEIGHTS

Similar to the previous chapter, for large-displacement and small-strain analysis novel planar curved Timoshenko-Ehrenfest beam elements are developed in this chapter. The development of these Timoshenko-Ehrenfest beam elements involves curvilinear coordinate systems, and the assumptions of small strains and thin beams. The derived formulations are simplified compared to the finite-strain counterparts. In addition, NURBS-based discretization incorporating the varying-weight concept is also employed. Nonetheless, the discretization is implemented using both quadratic and cubic NURBS. Subsequently, the proposed beam elements are assessed through solving four beam problems.

5.1 Kinematics of planar curved Timoshenko-Ehrenfest beams

5.1.1 Defining the initial and deformed configurations

In Figure 5.1, the kinematics of Timoshenko-Ehrenfest beams are characterized by two configurations, i.e., the initial configuration and the deformed configuration. This study employs the total Lagrangian formulation, which anchors all computations to the initial configuration. The vectorial quantities are introduced for each configuration. The quantities associated with the initial and deformed configurations are, respectively, denoted by uppercase and lowercase letters.

In the initial configuration, $\mathbf{R}_0(S)$ denotes the coordinates of point Q_0 on the initial beam axis. Here, S represents the arch-length variable of the initial beam axis. Since all the vectorial quantities in this section are defined in terms of S, it will be omitted in the later function notations for brevity. The unit tangent vector and the unit director vector of the initial beam axis, denoted by $\mathbf{A}_1$, are specified as in Equations (4.2) and (4.3), respectively. Let point Q be on the same cross-section as point Q_0. The coordinates of Q, denoted by $\mathbf{R}$, can be specified as Equation (4.4). Accordingly, the basis vectors $\mathbf{G}_1$ and $\mathbf{G}_2$ are determined as in Equations (4.6) and (4.7), respectively. Note that vector $\mathbf{G}_1$ is parallel to the vector $\mathbf{A}_1$, while vector $\mathbf{G}_2$ equals the unit vector $\mathbf{A}_2$ which is constant across the cross-section.

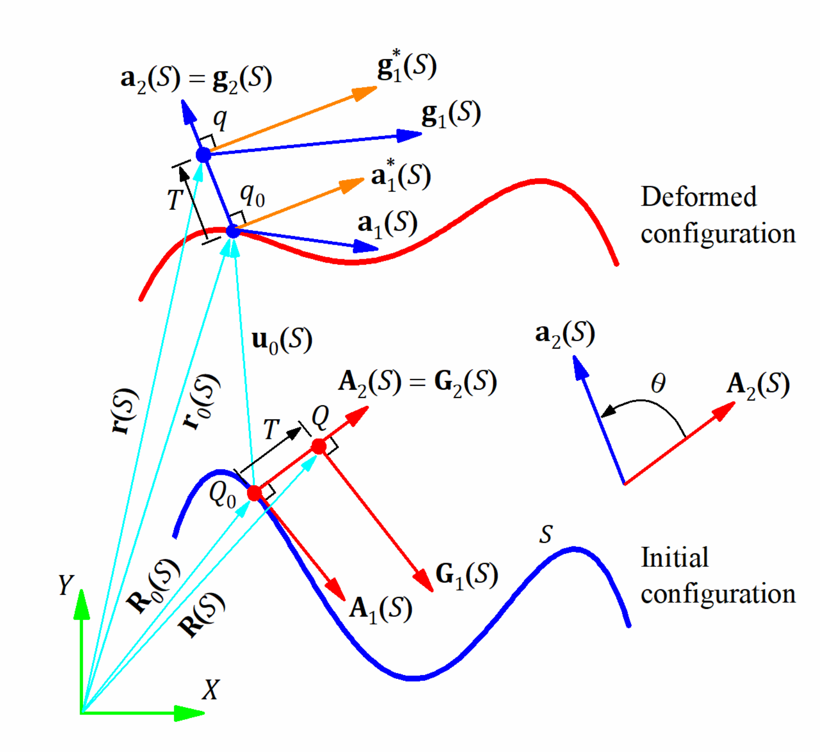

Figure 5.1 Initial and deformed configurations of a planar curved Timoshenko-Ehrenfest beam.

In the deformed configuration, q_0 represents the corresponding location of Q_0 on the deformed beam axis. The coordinates of q_0, denoted by $\mathbf{r}_0$, can be specified from Equation (4.1) where $\mathbf{u}_0 = [u_{0X} \quad u_{0Y}]^{\mathrm{T}}$ is still the translational displacements from Q_0 to q_0. Consequently, the tangent vector of the deformed beam axis, denoted by $\mathbf{a}_1$, is specified as in Equation (4.2). The unit vectors $\mathbf{a}_1^*$ and $\mathbf{a}_2$ are established in relation to the unit vectors $\mathbf{A}_1$ and $\mathbf{A}_2$, respectively, and incorporating the cross-sectional rotation θ as

$$\mathbf{a}_1^* = \mathbf{\Lambda}(\theta)\mathbf{A}_1 \qquad \mathbf{a}_2 = \mathbf{\Lambda}(\theta)\mathbf{A}_2. \tag{5.1}$$

In the framework of Timoshenko-Ehrenfest beams, the cross-sectional rotation θ is a result that integrates various influencing factors, primarily the bending and the shear effects. Generally, vector $\mathbf{a}_2$ is not perpendicular to the deformed beam axis. Therefore, vector $\mathbf{a}_1^*$ being orthogonal to the vector $\mathbf{a}_2$, is not tangential to the deformed beam axis. However, when the shear effect vanishes, bending remains the primary influencing factor for the cross-sectional rotation θ. Consequently, the vectors $\mathbf{a}_1^*$ and $\mathbf{a}_2$ become tangential and perpendicular to the deformed beam axis, respectively. This in fact aligns with the Euler-Bernoulli beam context (Vo & Nanakorn, 2020), when the shear effect is not considered in constructing beam kinematics.

On the same cross-section as point q_0, let q represent the corresponding location of Q. The coordinates of q, denoted by $\mathbf{r}$, can be determined as in Equation (4.5). Subsequently, the basis vectors $\mathbf{g}_1$ and $\mathbf{g}_2$ are defined as in Equations (4.6) and (4.7). In addition, the vector $\mathbf{g}_1^*$ is defined as

$$\mathbf{g}_1^* = \mathbf{\Lambda}(\theta)\mathbf{G}_1. \tag{5.2}$$

Vectors $\mathbf{g}_1$ and $\mathbf{a}_1$ do not exhibit parallelism, vector $\mathbf{g}_2$ equals the unit vector $\mathbf{a}_2$ which is tangential to the cross-section and remains constant across it. Additionally, vector $\mathbf{g}_1^*$ is parallel to the unit vector $\mathbf{a}_1^*$.

The basis vectors $\mathbf{G}_1$ and $\mathbf{G}_2$ are ultilized to form the covariant curvilinear coordinate system employed in the derivation. For the expression of the virtual work equation using the Green-Lagrange strain and second Piola-Kirchhoff stress tensors in this study, the reciprocal contravariant coordinate system is also introduced. The details of curvilinear coordinate systems are presented in 4.1.1, or can be referred to the studies of Vo and Nanakorn (2020, 2020).

5.1.2 Green-Lagrange strain and second Piola-Kirchhoff stress

The Green-Lagrange strain is specified in the contravariant curvilinear coordinate system $\mathbf{G}^\alpha \otimes \mathbf{G}^\beta$ as in Equations (4.10) $-$ (4.18). However, In Timoshenko-Ehrenfest beam, the tensor $\mathbf{Q}$, as defined in Equation (4.15), is not a right stretch tensor. The orthonormal vectors $\mathbf{a}_1^*$ and $\mathbf{a}_2$ can be regarded as the results of rotating the orthonormal vectors $\mathbf{A}_1$ and $\mathbf{A}_2$ by the angle θ, respectively. Let $G_1 = \|\mathbf{G}_1\|$ denote the length of vector $\mathbf{G}_1$, the orthonormal vectors $\mathbf{g}_1^*/G_1$ and $\mathbf{g}_2$ can be seen as the results of rotating the orthonormal vectors $\mathbf{G}_1/G_1$ and $\mathbf{G}_2$ by the angle θ, respectively. The rotation tensor $\mathbf{\Lambda}(\theta)$ can be expressed in terms of these vectors as

$$\mathbf{\Lambda}(\theta) = \mathbf{a}_1^* \otimes \mathbf{A}_1 + \mathbf{a}_2 \otimes \mathbf{A}_2 = \frac{\mathbf{g}_1^*}{G_1} \otimes \frac{\mathbf{G}_1}{G_1} + \mathbf{g}_2 \otimes \mathbf{G}_2. \tag{5.3}$$

The transpose of the rotation tensor can be specified as

$$\mathbf{\Lambda}^{\mathrm{T}}(\theta) = \mathbf{A}_1 \otimes \mathbf{a}_1^* + \mathbf{A}_2 \otimes \mathbf{a}_2 = \frac{\mathbf{G}_1}{G_1} \otimes \frac{\mathbf{g}_1^*}{G_1} + \mathbf{G}_2 \otimes \mathbf{g}_2. \tag{5.4}$$

From Equations (4.9), (4.11), (4.12), (4.15), and (5.4), the tensor $\mathbf{L}$ in Equation (4.17) is expressed explicitly as

$$\mathbf{L} = \mathbf{\Lambda}^{\mathrm{T}}(\theta)\mathbf{F} - \mathbf{G} = (\mathbf{g}_1^* \cdot \mathbf{g}_1 - (G_1)^2)\mathbf{G}^1 \otimes \mathbf{G}^1 + (\mathbf{a}_1 \cdot \mathbf{a}_2)\mathbf{G}^2 \otimes \mathbf{G}^1. \tag{5.5}$$

For the explicit demonstration of the above equation, please see Appendix A.

In Equation (5.5), to determine the term $\mathbf{g}_1^* . \mathbf{g}_1 - (G_1)^2$, $G_1 = \|\mathbf{G}_1\|$ is specified in the same manner as in 4.1.2, resulted in Equation (4.27). Recall that $\mathbf{a}_1^*$ is a unit vector, $\mathbf{g}_1^*$ is parallel to $\mathbf{a}_1^*$, and $\|\mathbf{g}_1^*\| = \|\mathbf{G}_1\| = G_1$. It yields G_1

$$\frac{\mathbf{g}_1^*}{G_1} = \mathbf{a}_1^*. \tag{5.6}$$

With the aid of Equations (4.6), (4.7), (4.27), and (5.6), the following variation is obtained as

$$
\begin{aligned}
\mathbf{g}_1^* \cdot \mathbf{g}_1 - (G_1)^2 &= (G_1\mathbf{a}_1^*) \cdot \mathbf{a}_1 + (G_1\mathbf{a}_1^*) \cdot (T\mathbf{a}_2') - (G_1)^2 \\
&= (\mathbf{a}_1 \cdot\ \mathbf{a}_1^* + T\mathbf{a}_1^* \cdot \mathbf{a}_2' - G_1)G_1 \\
&= \big(\mathbf{a}_1 \cdot\ \mathbf{a}_1^* - 1 - T(\mathbf{A}_1 \cdot \mathbf{A}_2' - \mathbf{a}_1^* \cdot \mathbf{a}_2')\big)(1 - Tk_0) \\
&= (\mathbf{a}_1 \cdot\ \mathbf{a}_1^* - 1) - T(\mathbf{A}_1 \cdot \mathbf{A}_2' - \mathbf{a}_1^* \cdot \mathbf{a}_2') - Tk_0(\mathbf{a}_1 \cdot\ \mathbf{a}_1^* - 1) \\
&+ T^2k_0(\mathbf{A}_1 \cdot \mathbf{A}_2' - \mathbf{a}_1^* \cdot \mathbf{a}_2').
\end{aligned}
\tag{5.7}
$$

Substituting Equation (5.7) into Equation (5.5) gives

$$
\begin{aligned}
\mathbf{L} = \big((\mathbf{a}_1 \cdot\ \mathbf{a}_1^* - 1) - T(\mathbf{A}_1 \cdot \mathbf{A}_2' - \mathbf{a}_1^* \cdot \mathbf{a}_2') - Tk_0(\mathbf{a}_1 \cdot\ \mathbf{a}_1^* - 1) \\
+ T^2k_0(\mathbf{A}_1 \cdot \mathbf{A}_2' - \mathbf{a}_1^* \cdot \mathbf{a}_2')\big)\mathbf{G}^1 \otimes \mathbf{G}^1 + (\mathbf{a}_1 \cdot \mathbf{a}_2)\mathbf{G}^2 \otimes \mathbf{G}^1.
\end{aligned}
\tag{5.8}
$$

For small strains, $(\mathbf{a}_1 \cdot\ \mathbf{a}_1^* - 1)$, $T(\mathbf{A}_1 \cdot \mathbf{A}_2' - \mathbf{a}_1^* \cdot \mathbf{a}_2')$, and $(\mathbf{a}_1 \cdot \mathbf{a}_2)$ are small. In addition, T is small for thin beams. Therefore, the terms $Tk_0(\mathbf{a}_1 \cdot\ \mathbf{a}_1^* - 1)$ and $T^2k_0(\mathbf{A}_1 \cdot \mathbf{A}_2' - \mathbf{a}_1^* \cdot \mathbf{a}_2')$ can be ignored, that leads to the shortening of tensor **L** as

$$
\mathbf{L} = \big(\mathbf{a}_1 \cdot\ \mathbf{a}_1^* - 1 - T(\mathbf{A}_1 \cdot \mathbf{A}_2' - \mathbf{a}_1^* \cdot \mathbf{a}_2')\big)\mathbf{G}^1 \otimes \mathbf{G}^1 + (\mathbf{a}_1 \cdot \mathbf{a}_2)\mathbf{G}^2 \otimes \mathbf{G}^1. \tag{5.9}
$$

Furthermore, since $(\mathbf{a}_1 \cdot\ \mathbf{a}_1^* - 1)$, $T(\mathbf{A}_1 \cdot \mathbf{A}_2' - \mathbf{a}_1^* \cdot \mathbf{a}_2')$, and $(\mathbf{a}_1 \cdot \mathbf{a}_2)$ are small, $\mathbf{L}^{\mathrm{T}}\mathbf{L}$ in Equation (4.18) can also be neglected (see Appendix B for more details). It follows that

$$
\mathbf{E} = \frac{1}{2}(\mathbf{L}^{\mathrm{T}} + \mathbf{L}). \tag{5.10}
$$

Substituting Equation (5.9) into Equation (5.10) gives

$$
\begin{aligned}
\mathbf{E} = \big(\mathbf{a}_1 \cdot\ \mathbf{a}_1^* - 1 - T(\mathbf{A}_1 \cdot \mathbf{A}_2' - \mathbf{a}_1^* \cdot \mathbf{a}_2')\big)\mathbf{G}^1 \otimes \mathbf{G}^1 + \frac{1}{2}(\mathbf{a}_1 \cdot \mathbf{a}_2)\mathbf{G}^1 \otimes \mathbf{G}^2 \\
+ \frac{1}{2}(\mathbf{a}_1 \cdot \mathbf{a}_2)\mathbf{G}^2 \otimes \mathbf{G}^1
\end{aligned}
\tag{5.11}
$$

The tensor **E** is expressed in the matrix form as

$$
\mathbf{E} = \begin{bmatrix} E_{11} & E_{12} \\ E_{21} & E_{22} \end{bmatrix} = \begin{bmatrix} \mathbf{a}_1 \cdot \mathbf{a}_1^* - 1 - T(\mathbf{A}_1 \cdot \mathbf{A}_2' - \mathbf{a}_1^* \cdot \mathbf{a}_2') & \frac{1}{2}\mathbf{a}_1 \cdot \mathbf{a}_2 \\ \frac{1}{2}\mathbf{a}_1 \cdot \mathbf{a}_2 & 0 \end{bmatrix}
$$

$$
= \begin{bmatrix} \Gamma_{11} - TK_{11} & \frac{1}{2}\Gamma_{12} \\ \frac{1}{2}\Gamma_{12} & 0 \end{bmatrix} \tag{5.12}
$$

where Γ_{11} is the axial strain, $\Gamma_{12} = 2E_{12} = 2E_{21}$ is the engineering shear strain. As K_{11} accounts for the shear effect, it does not solely reflect the change of curvature due to bending. Apparently, due to the small-strain assumption, Γ_{11} in Equation (5.12) are simpler than that in Equation (24) in the research of Vo and Nanakorn (2020), where the small-strain assumption is not applied.

The energy conjugate of the Green-Lagrange strain **E** is the second Piola-Kirchhoff stress **S**, specified in the covariant curvilinear coordinate system $\mathbf{G}_\alpha \otimes \mathbf{G}_\beta$ as Equation (4.37). As the Green-Lagrange strain tensor **E** has three non-zero strain components, i.e., E_{11}, E_{12} and E_{21}, the second Piola-Kirchhoff stress tensor **S** also consists of three corresponding non-zero stress components, i.e., S^{11}, S^{12} and S^{21}. These stress components are determined as

$$
S^{11} = \bar{E}E_{11} \qquad S^{12} = S^{21} = 2\bar{G}E_{12} = 2\bar{G}E_{21}. \tag{5.13}
$$

Linear elastic isotropic materials are applied in this study, $\bar{E}$ and $\bar{G}$ denote Young's modulus and shear modulus, respectively, measured in the covariant curvilinear coordinate system $\mathbf{G}_\alpha \otimes \mathbf{G}_\beta$. Let E and G represent Young's modulus and shear modulus of the material. For thin beams, $\bar{E}$ and $\bar{G}$ are assumed as constant across a cross-section as (Vo & Nanakorn, 2020)

$$
\bar{E} \approx E \qquad \bar{G} \approx G. \tag{5.14}
$$

5.1.3 The principle of virtual work

The principle of virtual work is expressed as

$$\delta\Pi_{int} = \delta\Pi_{ext} \tag{5.15}$$

where $\delta\Pi_{int}$ is internal virtual work and $\delta\Pi_{ext}$ is external virtual work.

The cross-sectional resultant forces are determined by the following integrations as

$$N^{11} = \int_A S^{11}\mathrm{d}A = EA\mathit{\Gamma}_{11} \qquad N^{12} = \int_A S^{12}dA = GA\mathit{\Gamma}_{12} \tag{5.16}$$

$$M^{11} = -\int_A TS^{11}\mathrm{d}A = EIK_{11}. \tag{5.17}$$

Here, N_{11}, N_{12} and M_{11} are the resultant axial force, resultant shear force, and resultant bending moment, respectively. Additionally, A and I denote the cross-sectional area and cross-sectional moment of inertia, respectively.

The internal virtual work is expressed with the aid of Equations (5.16) and (5.17) as

$$\begin{aligned}\delta\Pi_{int} &= \int_V \mathbf{S}:\delta\mathbf{E}\mathrm{d}V = \int_V (S^{11}\delta E_{11} + 2S^{12}\delta E_{12})\mathrm{d}V \\ &= \int_0^l (N^{11}\delta\mathit{\Gamma}_{11} + N^{12}\delta\mathit{\Gamma}_{12} + M^{11}\delta K_{11})\mathrm{d}S = \int_0^l \delta\mathbf{\Gamma}^{\mathrm{T}}\mathbf{D}\mathbf{\Gamma}\mathrm{d}S.\end{aligned} \tag{5.18}$$

Here, l and V are the length and the volume of the initial beam element, respectively. In addition, $\mathbf{\Gamma}$ and $\mathbf{D}$ denote the strain vector and the moduli matrix, respectively, i.e.,

$$\boldsymbol{\Gamma} = \begin{bmatrix} \Gamma_{11} \\ \Gamma_{12} \\ K_{11} \end{bmatrix} = \begin{bmatrix} \mathbf{a}_1^* \cdot \mathbf{a}_1 - 1 \\ \mathbf{a}_1 \cdot \mathbf{a}_2 \\ \mathbf{A}_1 \cdot \mathbf{A}_2' - \mathbf{a}_1^* \cdot \mathbf{a}_2' \end{bmatrix} \qquad \mathbf{D} = \begin{bmatrix} EA & 0 & 0 \\ 0 & GA & 0 \\ 0 & 0 & EI \end{bmatrix}. \tag{5.19}$$

The external virtual work is expressed as

$$\begin{aligned} \delta\Pi_{\text{ext}} = \int_0^l (\mathbf{f}^{\text{T}}\delta\mathbf{u}_0 + m\delta\theta)\mathrm{d}S + \mathbf{F}^{\text{T}}(0)\delta\mathbf{u}_0(0) + M(0)\delta\theta(0) \\ + \mathbf{F}^{\text{T}}(l)\delta\mathbf{u}_0(l) + M(l)\delta\theta(l). \end{aligned} \tag{5.20}$$

Here, $\mathbf{f} = [f_X \quad f_Y]^{\text{T}}$ and m are the distributed force vector and the distributed moment, respectively. Meanwhile, $\mathbf{F} = [F_X \quad F_Y]^T$ and M are, respectively, the concentrated force vector and the concentrated moment, which are applied to the beam axis at $S = 0$ or $S = l$. Moreover, $\mathbf{u}_0 = [u_{0X} \quad u_{0Y}]^{\text{T}}$ is the vector of translational displacements of the beam axis, determined from Equation (4.1), whereas θ is the cross-sectional rotation.

5.2 Finite element equation system

5.2.1 Field approximations by planar NURBS representations

The initial and deformed beam axes can parameterized in terms of the parametric dimension ξ using NURBS basis functions, denoted as $\mathbf{R}_0(\xi)$ and $\mathbf{r}_0(\xi)$, respectively, are determined in Equations (4.44) and (4.45). Accordingly, the displacement vector of the beam axis can be parameterized in terms of ξ, denoted as $\mathbf{u}_0(\xi)$, is specified in Equation (4.46). Assuming the zero cross-sectional rotation of the initial beam axis, the rotational displacement of a cross-section is subsequently the cross-sectional rotation of the deformed beam axis. Thus, the rotational displacement can be parameterized as

$$\theta(\xi) = \sum_{i=1}^{n} r_{i,p}(\xi)\theta_i \tag{5.21}$$

where θ_i denotes the rotation of i-th control point in the deformed configuration.

As stated in CHAPTER 3, this study employs quadratic and cubic NURBS representations, and $\xi \in [0, 1]$. Specifically, the quadratic NURBS ($p = 2$) with three control points ($n = 3$) is defined over a knot vector $\Xi = \Xi_{\mathrm{q}} = \{0, 0, 0, 1, 1, 1\}$. There are three quadratic B-spline basis functions which are determined in Equation (3.3). In addition, the cubic NURBS ($p = 3$) with four control points ($n = 4$) is defined over a knot vector $\Xi = \Xi_{\mathrm{c}} = \{0, 0, 0, 0, 1, 1, 1, 1\}$. There are four cubic B-spline basis functions which are determined in Equations (3.4) and (3.5).

5.2.2 Degrees of freedom

Stem from (5.21), the fields are discretized in terms of $\mathbf{C}_i = [X_i \quad Y_i]^{\mathrm{T}}$, $\mathbf{c}_i = [x_i \quad y_i]^{\mathrm{T}}$, and θ_i. Since $\mathbf{C}_i$ is associated with the initial configuration, which is unchanged during the deformation, X_i and Y_i are fixed. Therefore, only x_i, y_i, and θ_i are variables which can be directly treated as DOFs. Remind that $i = 1, 2, 3$ in quadratic elements, $i = 1, 2, 3, 4$ in cubic elements.

NURBS has an edge over the B-spline in terms of approximation capacity because of its weights which can be adjusted. Typically, in NURBS-based studies, these weights are set initially and remain constant during deformation. This yields optimal NURBS representation for the initial beam axis. However, while deformed beam axis can differ significantly from the initial beam axis under large displacements, the initial setup of NURBS may not hold optimal representation for the substantially deformed beam axes. Therefore, to better facilitate the NURBS adaptation to the deformation, and then enhance the approximation accuracy, NURBS weights are further exploited. This study treats some weights of control points as additional DOFs. Specifically, the weights of the first and the last control points are constant, while those of the other control points are treated as additional DOFs. Consequently, in quadratic NURBS, only w_2 serves as additional DOFs. Meanwhile, in cubic NURBS, w_2 and w_3 are additional DOFs.

Following this, the DOFs can be gathered into the vectors as

$$\mathbf{U}_{\mathrm{q}} = [x_1 \quad y_1 \quad \theta_1 \quad x_2 \quad y_2 \quad \theta_2 \quad w_2 \quad x_3 \quad y_3 \quad \theta_3]^{\mathrm{T}} \tag{5.22}$$

$$\mathbf{U}_{\mathrm{c}} = [x_1 \quad y_1 \quad \theta_1 \quad x_2 \quad y_2 \quad \theta_2 \quad w_2 \quad x_3 \quad y_3 \quad \theta_3 \quad w_3 \quad x_4 \quad y_4 \quad \theta_4]^{\mathrm{T}}. \tag{5.23}$$

where $\mathbf{U}_{\mathrm{q}}$ and $\mathbf{U}_{\mathrm{c}}$ are the DOF vectors for quadratic and cubic elements, respectively.

Discretizing the beam kinematics with weight DOFs highlights a key distinction between the proposed elements and conventional elements. In this study, conventional elements, which employs only x_i, y_i and θ_i as DOFs, are referred to as constant-weight elements. In contrast, the proposed elements, which incorporate not only x_i, y_i and θ_i but also certain NURBS weights as DOFs (as shown in Equations (5.22) and (5.23)), are termed varying-weight elements.

5.2.3 Discretizing the beam kinematics

The discretization process for quadratic and cubic elements shares similarities. In this manuscript, the discretization of cubic elements is detailed. Such a process can be easily adapted for quadratic elements.

Recall the DOFs vector $\mathbf{U}_{\mathrm{c}}$ for cubic elements in Equation (5.23). Additionally, define the vector of nodal forces and moments as

$$\mathbf{P} = [F_X(0) \quad F_Y(0) \quad M(0) \quad 0 \quad 0 \quad 0 \quad 0 \quad 0 \quad 0 \quad 0 \quad 0 \quad F_X(l) \quad F_Y(l) \quad M(l)]^{\mathrm{T}}. \tag{5.24}$$

From the relations in Equations (4.44) and (4.46) for cubic elements, $\mathbf{r}_0(\xi)$, $\mathbf{u}_0(\xi)$ and $\theta(\xi)$ are interpreted in terms of the DOFs in $\mathbf{U}_{\mathrm{c}}$. Consequently, $\Gamma_{11}(\xi)$, $\Gamma_{12}(\xi)$, $K_{11}(\xi)$ are also expressed in terms of the DOFs in $\mathbf{U}_{\mathrm{c}}$. These facilitate the calculation of the partial derivatives of $\Gamma_{11}(\xi)$, $\Gamma_{12}(\xi)$, $K_{11}(\xi)$, $u_{0X}(\xi)$, $u_{0Y}(\xi)$, and $\theta(\xi)$ with respect to these DOFs. For conciseness, ξ is omitted in the later function notations.

Define the matrix $\mathbf{B}$ as

$$\mathbf{B} = \begin{bmatrix} \frac{\partial \Gamma_{11}}{\partial x_1} & \frac{\partial \Gamma_{11}}{\partial y_1} & \frac{\partial \Gamma_{11}}{\partial \theta_1} & \frac{\partial \Gamma_{11}}{\partial x_2} & \frac{\partial \Gamma_{11}}{\partial y_2} & \frac{\partial \Gamma_{11}}{\partial \theta_2} & \frac{\partial \Gamma_{11}}{\partial w_2} & \frac{\partial \Gamma_{11}}{\partial x_3} & \frac{\partial \Gamma_{11}}{\partial y_3} & \frac{\partial \Gamma_{11}}{\partial \theta_3} & \frac{\partial \Gamma_{11}}{\partial w_3} & \frac{\partial \Gamma_{11}}{\partial x_4} & \frac{\partial \Gamma_{11}}{\partial y_4} & \frac{\partial \Gamma_{11}}{\partial \theta_4} \\ \frac{\partial \Gamma_{12}}{\partial x_1} & \frac{\partial \Gamma_{12}}{\partial y_1} & \frac{\partial \Gamma_{12}}{\partial \theta_1} & \frac{\partial \Gamma_{12}}{\partial x_2} & \frac{\partial \Gamma_{12}}{\partial y_2} & \frac{\partial \Gamma_{12}}{\partial \theta_2} & \frac{\partial \Gamma_{12}}{\partial w_2} & \frac{\partial \Gamma_{12}}{\partial x_3} & \frac{\partial \Gamma_{12}}{\partial y_3} & \frac{\partial \Gamma_{12}}{\partial \theta_3} & \frac{\partial \Gamma_{12}}{\partial w_3} & \frac{\partial \Gamma_{12}}{\partial x_4} & \frac{\partial \Gamma_{12}}{\partial y_4} & \frac{\partial \Gamma_{12}}{\partial \theta_4} \\ \frac{\partial K_{11}}{\partial x_1} & \frac{\partial K_{11}}{\partial y_1} & \frac{\partial K_{11}}{\partial \theta_1} & \frac{\partial K_{11}}{\partial x_2} & \frac{\partial K_{11}}{\partial y_2} & \frac{\partial K_{11}}{\partial \theta_2} & \frac{\partial K_{11}}{\partial w_2} & \frac{\partial K_{11}}{\partial x_3} & \frac{\partial K_{11}}{\partial y_3} & \frac{\partial K_{11}}{\partial \theta_3} & \frac{\partial K_{11}}{\partial w_3} & \frac{\partial K_{11}}{\partial x_4} & \frac{\partial K_{11}}{\partial y_4} & \frac{\partial K_{11}}{\partial \theta_4} \end{bmatrix} \tag{5.25}$$

The variation of $\mathbf{\Gamma}$ is expressed as

$$\delta\mathbf{\Gamma} = \mathbf{B}\delta\mathbf{U}_{\mathrm{c}}. \tag{5.26}$$

The internal virtual work in Equation (5.18) is identified as

$$\delta\Pi_{int} = \delta\mathbf{U}_{\mathrm{c}}^{\mathrm{T}}\int_{0}^{l}\mathbf{B}^{\mathrm{T}}\mathbf{D}\mathbf{\Gamma}\mathrm{d}S. \tag{5.27}$$

Introduce the matrix $\mathbf{H}_{XY}$ and the vector $\mathbf{H}_{\theta}$ as

$$\mathbf{H}_{XY} = \begin{bmatrix} \frac{\partial u_{0X}}{\partial x_1} & \frac{\partial u_{0X}}{\partial y_1} & \frac{\partial u_{0X}}{\partial \theta_1} & \frac{\partial u_{0X}}{\partial x_2} & \frac{\partial u_{0X}}{\partial y_2} & \frac{\partial u_{0X}}{\partial \theta_2} & \frac{\partial u_{0X}}{\partial w_2} & \frac{\partial u_{0X}}{\partial x_3} & \frac{\partial u_{0X}}{\partial y_3} & \frac{\partial u_{0X}}{\partial \theta_3} & \frac{\partial u_{0X}}{\partial w_3} & \frac{\partial u_{0X}}{\partial x_4} & \frac{\partial u_{0X}}{\partial y_4} & \frac{\partial u_{0X}}{\partial \theta_4} \\ \frac{\partial u_{0Y}}{\partial x_1} & \frac{\partial u_{0Y}}{\partial y_1} & \frac{\partial u_{0Y}}{\partial \theta_1} & \frac{\partial u_{0Y}}{\partial x_2} & \frac{\partial u_{0Y}}{\partial y_2} & \frac{\partial u_{0Y}}{\partial \theta_2} & \frac{\partial u_{0Y}}{\partial w_2} & \frac{\partial u_{0Y}}{\partial x_3} & \frac{\partial u_{0Y}}{\partial y_3} & \frac{\partial u_{0Y}}{\partial \theta_3} & \frac{\partial u_{0Y}}{\partial w_3} & \frac{\partial u_{0Y}}{\partial x_4} & \frac{\partial u_{0Y}}{\partial y_4} & \frac{\partial u_{0Y}}{\partial \theta_4} \end{bmatrix} \tag{5.28}$$

$$\mathbf{H}_{\theta} = \begin{bmatrix} \frac{\partial \theta}{\partial x_1} & \frac{\partial \theta}{\partial y_1} & \frac{\partial \theta}{\partial \theta_1} & \frac{\partial \theta}{\partial x_2} & \frac{\partial \theta}{\partial y_2} & \frac{\partial \theta}{\partial \theta_2} & \frac{\partial \theta}{\partial w_2} & \frac{\partial \theta}{\partial x_3} & \frac{\partial \theta}{\partial y_3} & \frac{\partial \theta}{\partial \theta_3} & \frac{\partial \theta}{\partial w_3} & \frac{\partial \theta}{\partial x_4} & \frac{\partial \theta}{\partial y_4} & \frac{\partial \theta}{\partial \theta_4} \end{bmatrix}. \tag{5.29}$$

The variations of $\mathbf{u}_0$ and θ are determined as

$$\delta\mathbf{u}_0 = \mathbf{H}_{XY}\delta\mathbf{U}_{\mathrm{c}} \qquad \delta\theta = \mathbf{H}_{\theta}\delta\mathbf{U}_{\mathrm{c}}. \tag{5.30}$$

The external virtual work in Equation (5.20) is then expressed as

$$\delta\Pi_{ext} = \delta\mathbf{U}_{\mathrm{c}}^{\mathrm{T}}\int_{0}^{l}(\mathbf{H}_{XY}^{\mathrm{T}}\mathbf{f} + \mathbf{H}_{\theta}^{\mathrm{T}}m)\mathrm{d}S + \delta\mathbf{U}_{\mathrm{c}}^{\mathrm{T}}\mathbf{P}. \tag{5.31}$$

In the above equation, the first term on the right-hand side reveals that the effect of distributed loads depends on the deformation.

Eventually, the equation system is obtained from Equations (5.15), (5.27), and (5.31) as

$$\mathbf{\Phi} - \mathbf{p} - \mathbf{P} = \mathbf{0} \tag{5.32}$$

where

$$\mathbf{\Phi} = \int_0^l \mathbf{B}^{\mathrm{T}}\mathbf{D}\mathbf{\Gamma}\mathrm{d}S \qquad \mathbf{p} = \int_0^l \left(\mathbf{H}_{XY}^{\mathrm{T}}\mathbf{f} + \mathbf{H}_{\theta}^{\mathrm{T}}m\right)\mathrm{d}S. \tag{5.33}$$

The equation system in Equation (5.32) is inherently nonlinear in terms of the DOFs in $\mathbf{U}_{\mathrm{C}}$. Therefore, linearization is required to enable the use of iterative methods, such as the Newton-Raphson methods (Torkamani & Sonmez, 2008). As stated in CHAPTER 4, determining the derivatives for the linearization can be complex and time-consuming. Within the use of quadratic and cubic NURBS, this task can be efficiently handled by using the symbolic computing capabilities of commercial software. In this study, MATLAB is employed for this purpose.

5.3 Numerical examples

The proposed Timoshenko-Ehrenfest beam elements are appraised through solving four beam problems undergoing large and complex deformations. The beam's cross-sections are rectangular and constant across the lengths, with b and h denoting the cross-sectional width and height, respectively. Additionally, E denotes Young's modulus, Poisson's ratio is set equal to 0.3, and $I = bh^3/12$ is the cross-sectional moment of inertia. In problem 5.3.1, analytical solutions are available and serve as the reference solutions. In the subsequent problems, the reference solutions are converged solutions obtained using fine meshes of the Timoshenko-Ehrenfest beam element presented in the study of Vo and Nanakorn (2020). Moreover, problem 5.3.1 is solved with quadratic and cubic elements, while the other problems are solved with only cubic elements.

Performances of the proposed varying-weight elements and the constant-weight elements are rigorously compared, always entailing the use of three cubic models in each problem, i.e., VW, CW1, and CW2. Concretely, model VW consists of a minimum number of cubic varying-weight elements, necessary for achieving accurate solutions.

Model CW1 includes cubic constant-weight elements, with an approximate DOF number to VW, ensuring a fair comparison. Given that CW1 always yields solutions with lower accuracy than VW in the considered problems, the number of cubic constant-weight elements increases until the accuracy level of VW is reached, resulting in model CW2. In addition, as quadratic elements are used in problem 5.3.1, there are three additional quadratic models designated in a similar manner, signified as QVW, QCW1, and QCW2. Furthermore, the comparisons to the $\overline{\mathrm{B}}$ elements introduced by Vo, Nanakorn, Bui and Rungamornrat (2022) are made in all problems. These $\overline{\mathrm{B}}$ elements effectively address locking effects and improve the accuracy, however, require significantly more computational effort. In problem 5.3.1, their performances are exhibited in the convergence graphs. Meanwhile, in problems 5.3.2 to 5.3.4, their performances are exhibited with model BB, consisting of the minimum number of cubic $\overline{\mathrm{B}}$ elements to achieve the accuracy level of VW.

These model details are shown in Table 5.1 for quadratic elements, and Table 5.2 for cubic elements.

Table 5.1 Details of quadratic models.

Problem	No. of elements (No. of DOFs)			DOF ratio of QCW2 / QVW
	QVW Quadratic Varying-weight elements	QCW1 Quadratic Constant-weight elements	QCW2 Quadratic Constant-weight elements	
5.3.1 – A circular cantilever arch subjected to a uniformly distributed moment	20 (140)	24 (144)	110 (660)	4.7

Table 5.2 Details of cubic models.

Problem	No. of elements (No. of DOFs)				DOF ratio of CW2 / VW
	VW Cubic Varying-weight elements	CW1 Cubic Constant-weight elements	CW2 Cubic Constant-weight elements	BB Cubic $\overline{\text{B}}$ elements (2022)	
5.3.1 – A circular cantilever arch subjected to a uniformly distributed moment	5 (55)	6 (54)	17 (153)	–	2.8
5.3.2 – A zigzag beam	10 (110)	12 (108)	34 (306)	10 (90)	2.8
5.3.3 – The snap behaviors of an S-shaped beam subjected to a downwardly concentrated force	8 (87)	10 (89)	36 (323)	10 (89)	3.7
5.3.4 – A spring in watches undergoing multiple snap phenomena	26 (284)	32 (286)	104 (934)	34(304)	3.3

5.3.1 A circular cantilever arch subjected to a uniformly distributed moment

As described in Figure 5.2, this problem involves a circular cantilever arch, with a span angle of $\pi/2$ and is subjected to a uniformly distributed moment m along the arch's length. Let R represent the radius of the arch, the arch's length (denoted by L) is calculated as $L = \pi R/2$.

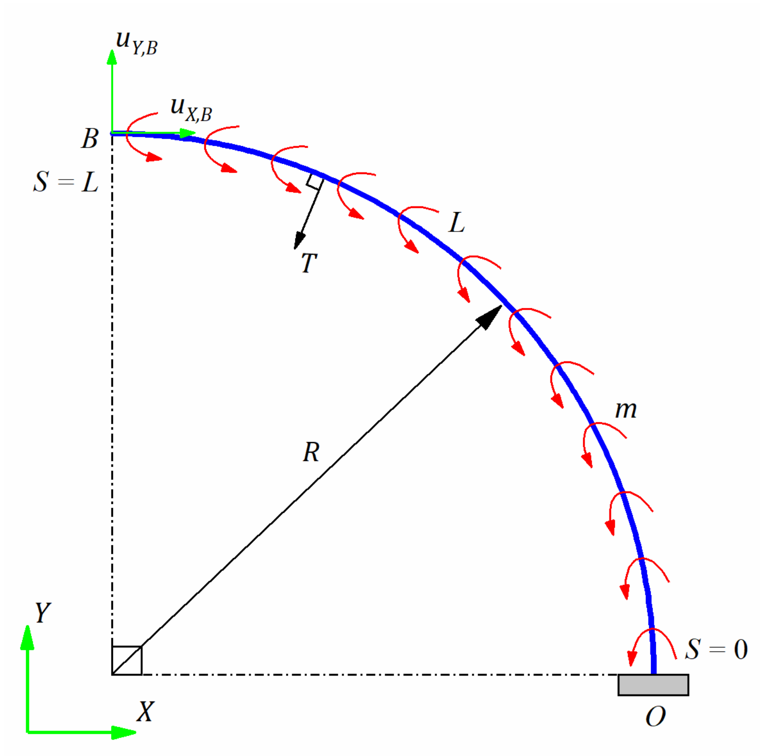

Figure 5.2 Problem 5.3.1: A circular cantilever arch subjected to a uniformly distributed moment.

As the deformation is pure bending, the analytical solutions are obtainable and serve as reference solutions. In this problem, let S denote the arc-length variable, i.e., $S \in [0, L]$. The curvature of the undeformed arch, denoted by k_0, is uniform along the arch's length and is specified as

$$k_0(S) = \frac{1}{R}. \tag{5.34}$$

In Figure 5.2, point O is on the arch axis at the clamped support, i.e., $S = 0$. Let $\begin{bmatrix} 0 \\ 0 \end{bmatrix}$ be the coordinates of O, the coordinates of the undeformed arch axis, $\mathbf{R}_0(S) = \begin{bmatrix} X(S) \\ Y(S) \end{bmatrix}$, can be determined as

$$X(S) = -\int_0^S \sin\alpha(S)\,\mathrm{d}S \qquad Y(S) = \int_0^S \cos\alpha(S)\,\mathrm{d}S \tag{5.35}$$

where

$$\alpha(S) = \int_0^S k_0(S)\mathrm{d}S = \frac{S}{R}. \tag{5.36}$$

Subsequently, the coordinates of the undeformed arch axis in Equation (5.35) become

$$X(S) = R\left(\cos\left(\frac{S}{R}\right) - 1\right) \qquad Y(S) = R\sin\left(\frac{S}{R}\right). \tag{5.37}$$

Additionally, since the shear effect does not exist, $K_{11}(S)$ in Equation (5.12) exactly represents the absolute change of curvature due to bending, specified from the internal resultant moment M^{11} in Equation (5.17) as

$$K_{11}(S) = \frac{m(L - S)}{EI}. \tag{5.38}$$

Hence, the curvature of the deformed arch, denoted by k, is obtained as

$$k(S) = k_0(S) + K_{11}(S). \tag{5.39}$$

Similarly, the coordinates of the deformed arch axis, $\mathbf{r}_0(S) = \begin{bmatrix} x(S) \\ y(S) \end{bmatrix}$, can be determined as

$$x(S) = -\int_0^S \sin\beta(S)\,\mathrm{d}S \qquad\qquad y(S) = \int_0^S \cos\beta(S)\,\mathrm{d}S \tag{5.40}$$

where

$$\beta(S) = \int_0^S k(S)\mathrm{d}S = \frac{m(LS - 0.5S^2)}{EI} + \frac{S}{R}. \tag{5.41}$$

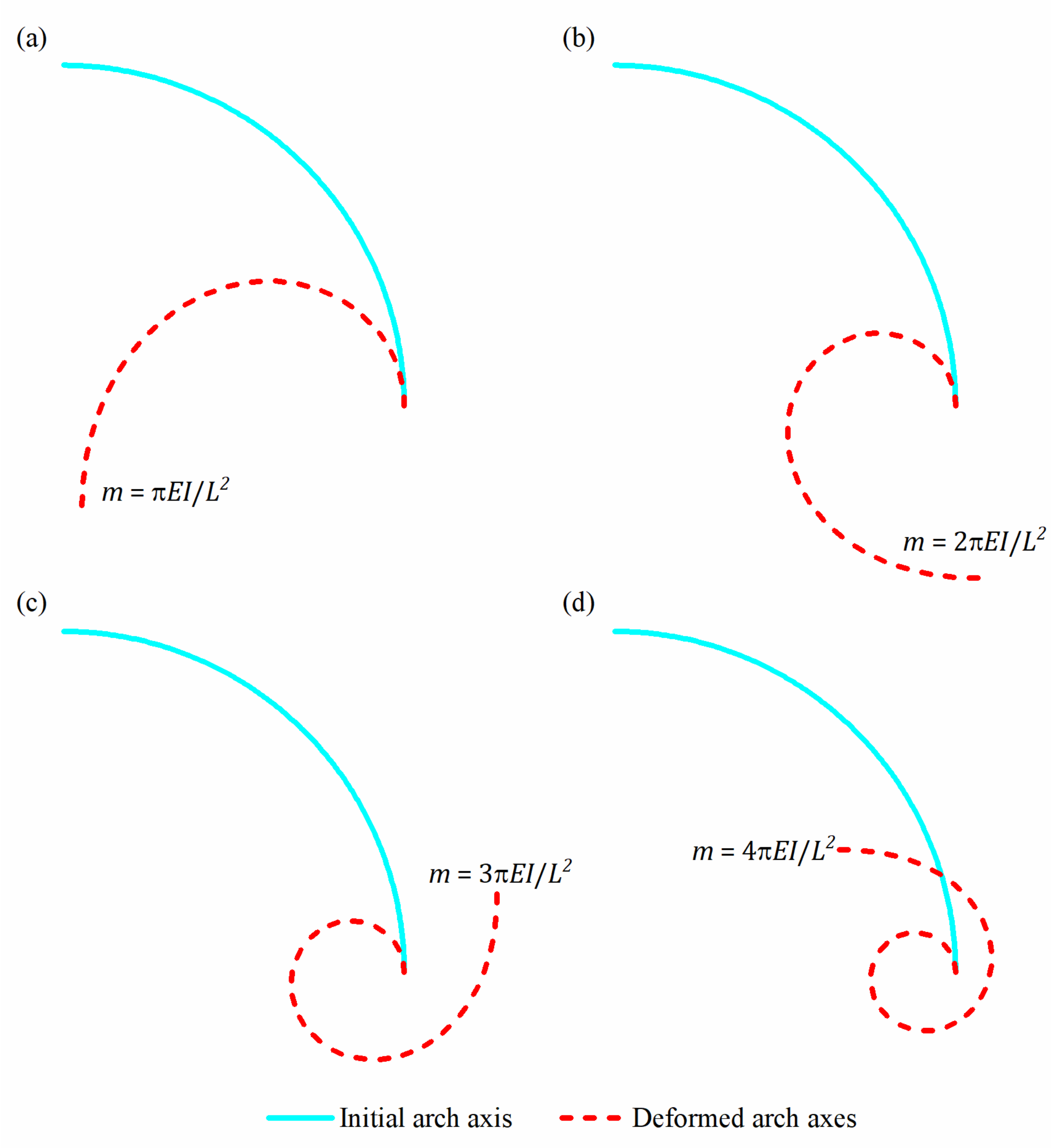

Figure 5.3 Problem 5.3.1: Several analytical deformed configurations of the arch.

With the aids of Equations (5.40) and (5.41), in Figure 5.3, the analytical deformations with respect to $m = \pi EI/L^2$, $2\pi EI/L^2$, $3\pi EI/L^2$, $4\pi EI/L^2$ are depicted. Initially, the undeformed arch exhibits a uniform curvature along the entire length. However, upon the application of the uniformly distributed moment m, the arch undergoes large deformations and loses its uniform curvature. At the final deformation stage with $m = 4\pi EI/L^2$, it is bent into a spiral-like curve, as unveiled in Figure 5.3d.

From Equations (4.1), (5.35), and (5.40), the translational displacements of the beam axis, denoted by $u_{X,B}$ and $u_{Y,B}$, are specified as

$$\begin{bmatrix} u_{0X}(S) \\ u_{0Y}(S) \end{bmatrix} = \mathbf{u}_0(S) = \mathbf{r}_0(S) - \mathbf{R}_0(S) = \begin{bmatrix} x(S) - X(S) \\ y(L) - Y(L) \end{bmatrix}. \tag{5.42}$$

Subsequently, accuracy tests are conducted to assess the performances of the constant-weight and varying-weight elements. In these tests, cross-sectional height of the arch h is set equal to $0.01R$. In addition, six models of the two variants are considered, i.e., QVW, QCW1, and QCW2 with quadratic elements are detailed in Table 5.1, and VW, CW1, and CW2 with cubic elements are detailed in Table 5.2. Firstly, the accuracy test involves translational displacements of the arch axis at the free end B, i.e., $u_{0X,B}$ and $u_{0Y,B}$. The analytical solutions for these displacements are specified in Equation (5.42) with $S = L$ at point B. Figure 5.4 unveils the curves of normalized load and displacements of the arch axis at the free end B obtained by the quadratic models, while those obtained by the cubic models are shown in Figure 5.5. Regardless of whether the quadratic or cubic elements are employed, the superiority of varying-weight elements over constant-weight elements is exhibited.

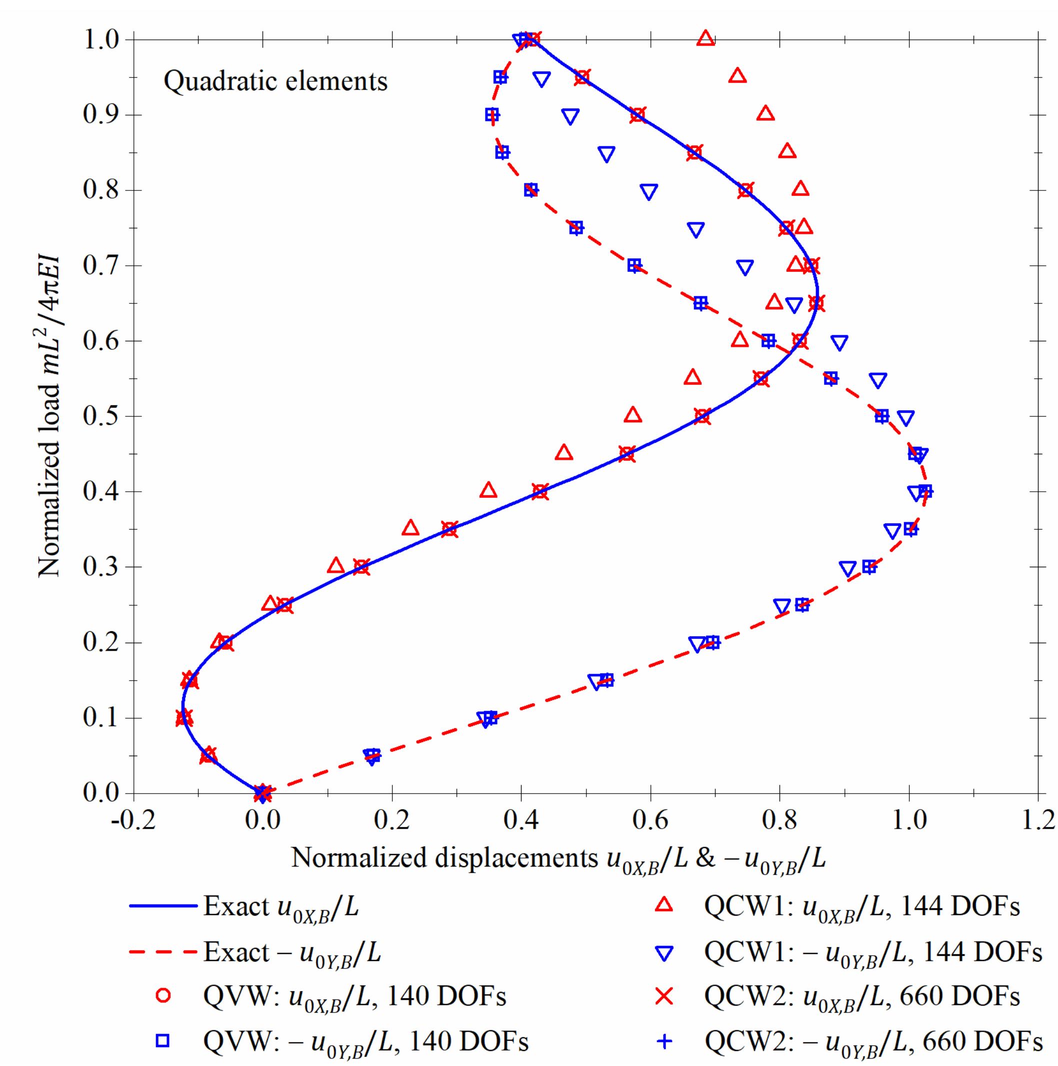

Figure 5.4 Problem 5.3.1: Normalized load-displacement curves of the arch axis at the free end B, using quadratic models.

In Figure 5.4, model QVW of quadratic varying-weight elements with 140 DOFs results in closely matched solutions with the analytical solutions, while QCW1 of quadratic constant-weight elements with a similar DOF number cannot predict well the solutions. To achieve the accuracy level of model QVW, the quadratic constant-weight element necessitates QCW2 with 660 DOFs, about 4.7 times higher than those of QVW. Similarly, in Figure 5.5, model VW of cubic varying-weight elements and model CW1 of cubic constant-weight elements consume similar DOF numbers, however, only VW provides accurate solutions. Model CW2 of cubic constant-weight elements can yield accurate results but consumes about 2.8 times more DOFs than VW.

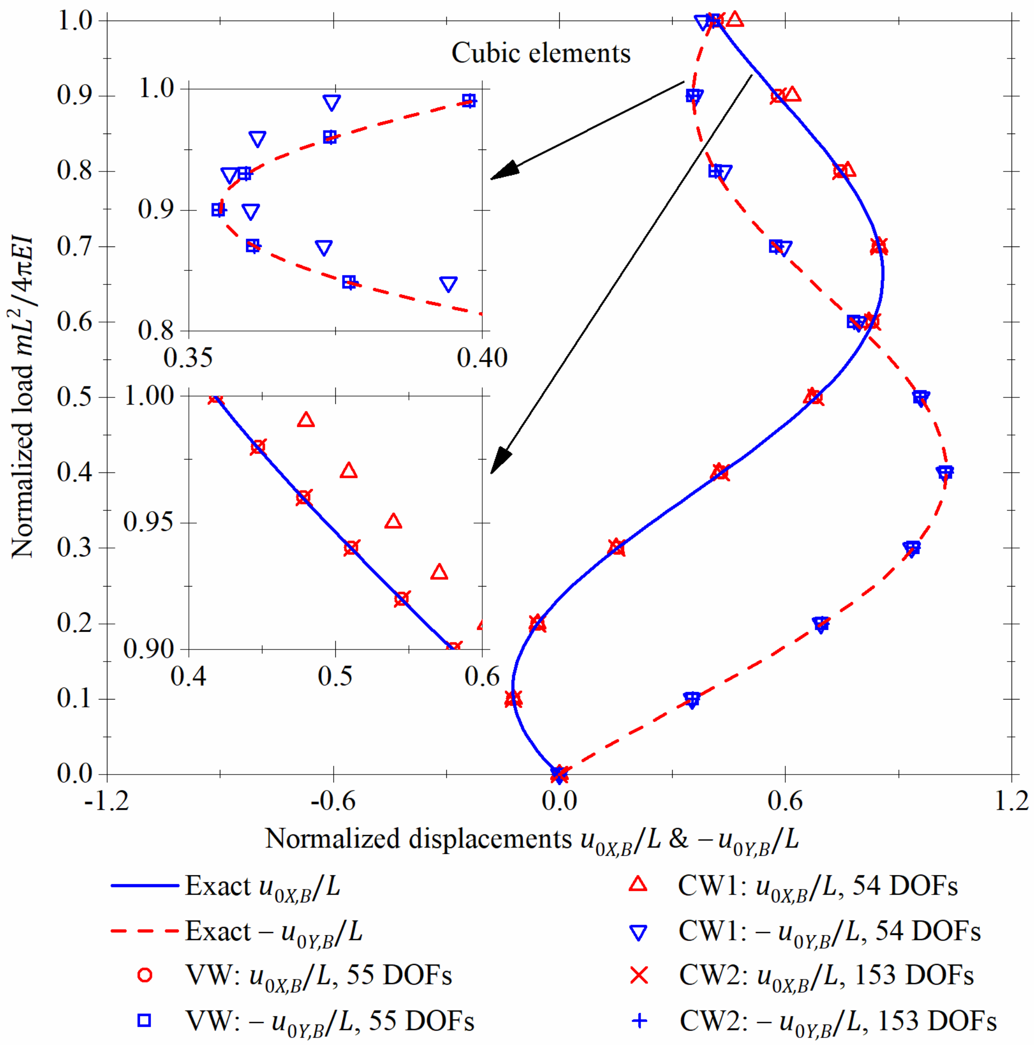

Figure 5.5 Problem 5.3.1: Normalized load-displacement curves of the arch axis at the free end B, using cubic models.

This trend is repeated in Figure 5.6, where final deformed arch axes, given by these models, are depicted. The reference deformed arch axis is derived analytically in Equation (5.40) with $m = 4\pi EI/L^2$. In Figure 5.6a with the quadratic elements, the deformed axes given by QVW and QCW2 are indistinguishable from the analytical one, whereas that of QCW1 shows a remarkable difference. Similarly, in Figure 5.6b with the cubic elements, VW and CW2 can yield precise deformed arch axes, while CW1 cannot.

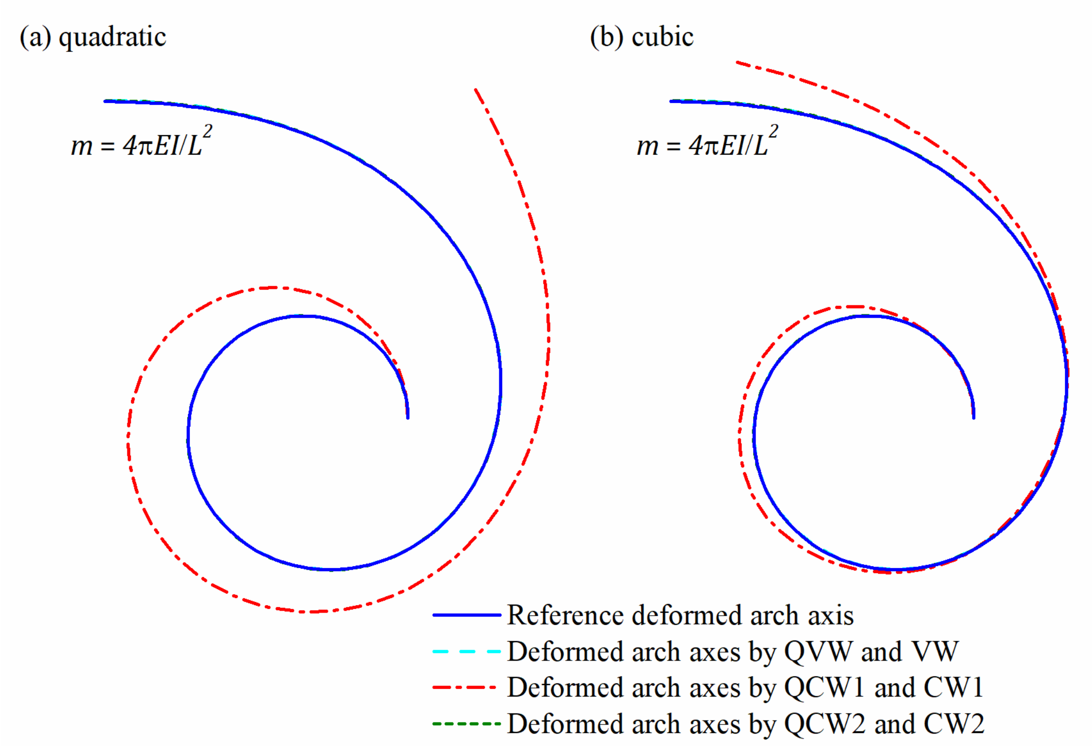

Figure 5.6 Problem 5.3.1: Final deformed arch axes given by using the six models.

Elucidating further the accuracy of the proposed elements, convergences of the relative errors in the deformed arch axes are examined. Convergences indicate how well the obtained solutions approach the reference one as increasing the DOF numbers. In this test, relative errors, denoted by RE, in the deformed arch axes are calculated as

$$RE = \sqrt{\frac{\int_0^L \left(\mathbf{r}_{0,num} - \mathbf{r}_{0,ref}\right)^2 \mathrm{d}S}{\int_0^L \left(\mathbf{r}_{0,ref}\right)^2 \mathrm{d}S}}. \tag{5.43}$$

Here, $\mathbf{r}_{0,ref} = [x \quad y]^{\mathrm{T}}$ is the reference deformed arch axis, which is derived analytically in Equation (5.40). Meanwhile, $\mathbf{r}_{0,num}$ represents the deformed arch axis obtained using the proposed elements. Additionally, as stated earlier, L is the arch's length and S is the arc-length variables. Accordingly, a small relative error indicates that the obtained deformed arch axis is closely aligned to the reference one, and vice versa. This test considers the final deformed arch axes, i.e., $m = 4\pi EI/L^2$.

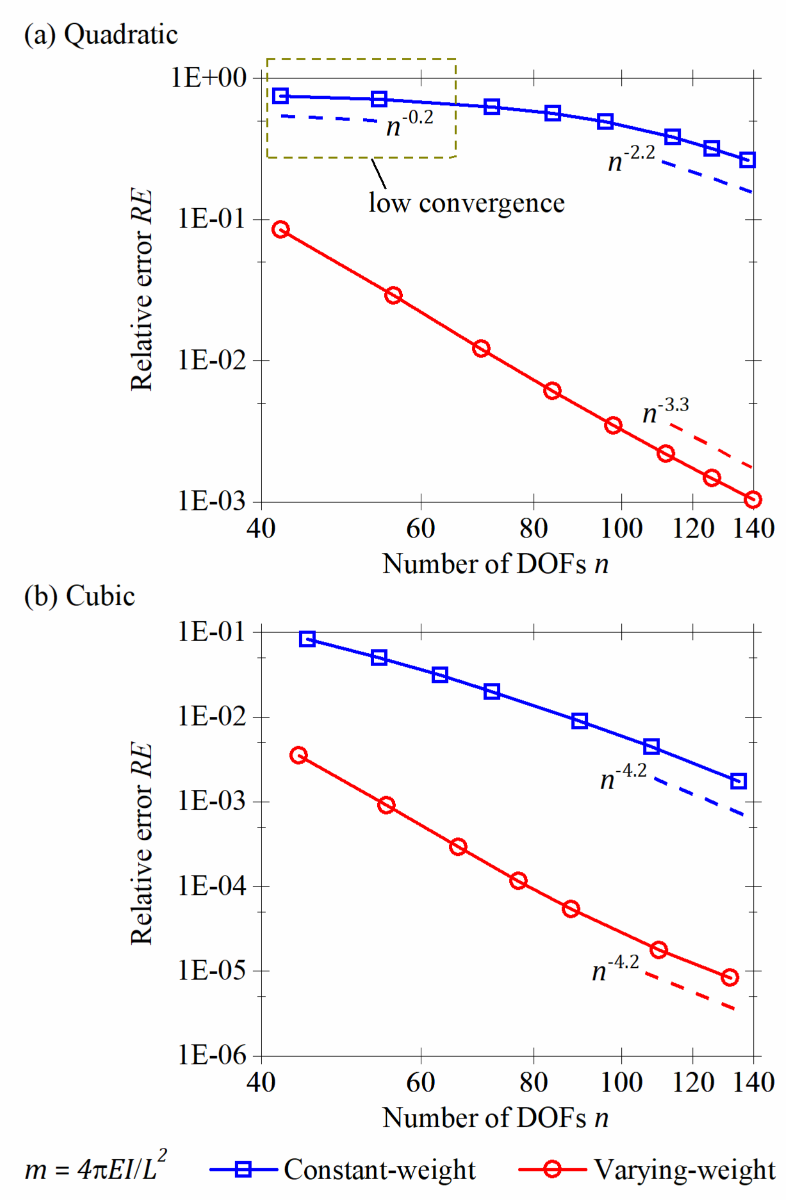

Figure 5.7 Problem 5.3.1: Convergences of the relative errors in the final deformed arch axes.

The convergence graphs are plotted in Figure 5.7. Across the DOF ranges, the varying-weight elements consistently produce smaller relative errors than the constant-weight counterparts. In Figure 5.7a with quadratic elements, the varying-weight element reaches the convergence order of 3.3 by the end of the DOF range, while the constant-weight element only achieves the order of 2.2. In Figure 5.7b with cubic elements, both end up with the same convergence order of 4.2. It is crucial to highlight that while the constant-weight elements yield good convergence with cubic order, its convergence with quadratic order is noticeably low, particularly at the beginning of the DOF range (coarse meshes) as exhibited in Figure 5.7a. This observation raises a suspicion of locking effects, which are subsequently investigated.

Locking effects, i.e., membrane locking and shear locking in Timoshenko-Ehrenfest beams, are well-known phenomena in FEA and IGA of thin beams. These effects cause the spurious stiffening of thin beams, leading to smaller displacements and increased errors. To tackle these challenges, various techniques have been introduced, i.e., elevating the order of interpolations, using different interpolations for different kinematic unknowns, reduced and selective integration techniques, mixed methods, $\overline{\mathrm{B}}$-projection methods, and discrete strain gap methods (Bletzinger, Bischoff & Ramm, 2000; Ishaquddin, Raveendranath & Reddy, 2012; Nukala & White, 2004; Vo & Nanakorn, 2020; Vo, Nanakorn, Bui & Rungamornrat, 2022). However, these techniques often require additional complexities or costs. Consequently, the utilization of naturally locking-free elements is paid more interest, in this regard, varying-weight elements emerge as potential candidates.

To expose locking effects in this problem, three thicknesses of the arch are considered, i.e., $R/h = 100$, $R/h = 1000$, and $R/h = 10000$, which represent a very thin arch to an extremely thin arch. The convergences of relative errors in the final deformed arch axes, i.e., $m = 4\pi EI/L^2$, are examined and depicted in Figure 5.8. Moreover, these outcomes are compared to those obtained using the $\overline{\mathrm{B}}$ Timoshenko-Ehrenfest beam element introduced by Vo, Nanakorn, Bui and Rungamornrat (2022).

In Figure 5.8a, employing quadratic elements, the constant-weight element exhibits a noticeable loss of accuracy as the thickness decreases. The relative errors corresponding to $R/h = 1000$ and $R/h = 10000$ shows little to no convergence across the DOF range, which sharply contrasts to the outcome with $R/h = 100$. This clearly demonstrates the severe locking phenomena. Conversely, the varying-weight element does not exhibit locking phenomena, as similar relative errors are observed regardless of thickness. Furthermore, the solutions obtained using the $\overline{\mathrm{B}}$ element reveals no locking effect. While these solutions provide smaller relative errors than those of the varying-weight variant, they consume approximately 4 to 7 times more computational effort.

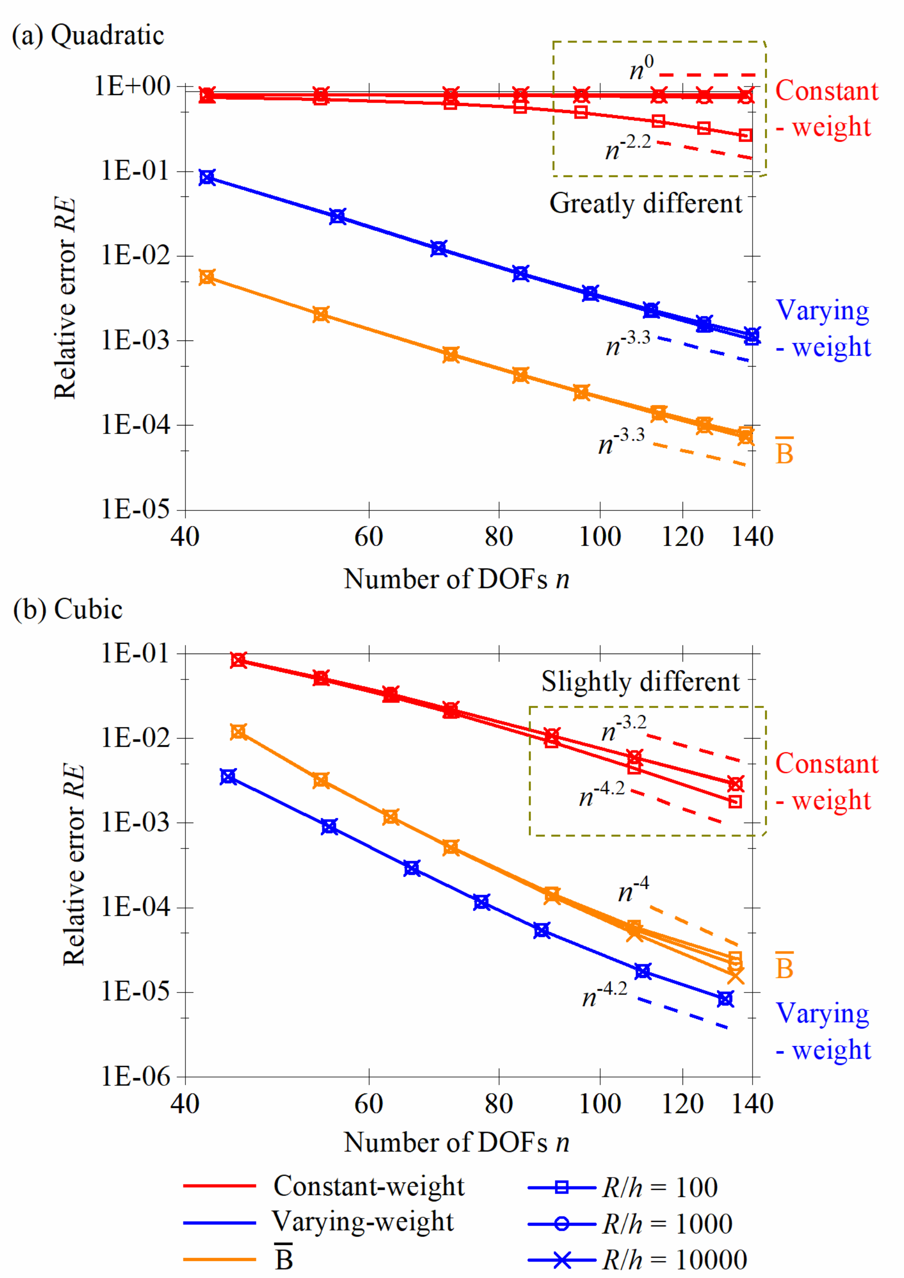

Figure 5.8 Problem 5.3.1: Convergences of the relative errors in the final deformed arch axes, for different R/h ratios.

In Figure 5.8b, employing cubic elements, none of the variants exhibit severe locking phenomena, as there is no notable loss in accuracy with decreasing thickness. Although a slight difference is observed with the constant-weight variant, it is insignificant. Moreover, despite consuming more than 7 times of computational cost, the $\overline{\mathrm{B}}$ element still yields higher relative errors than the varying-weight element.

In this problem, varying-weight elements are locking-free regardless of the order. In addition, it is important to note that locking mitigation exhibited in Figure 5.8b is primarily attributed to the increase of the order (from quadratic to cubic) of the constant-weight elements, rather than their inherent robust locking-free feature. Moreover, the quadratic constant-weight element easily experiences locking effects, even with $R/h = 100$ as very low convergence is exhibited at the beginning of the DOF range (coarse meshes), as highlighted in Figure 5.7a. Therefore, in the subsequent problems, only cubic elements are employed.

5.3.2 A zigzag frame

This problem is a zigzag frame, assembled by 10 straight segments, as shown in Figure 5.9. One end of the frame, i.e., end O, is affixed by a roller support restricting the vertical movement, and subjected to a horizontal force P with the maximum magnitude of $14.5EI/L^2$. The other end of the frame, i.e., end B, is constrained by a pinned support. In the undeformed configuration, any two adjacent segments of the frame form a right angle. In addition, the lengths of the first and the last segments are half the length of the other segments. As mentioned earlier, for this problem, the reference solutions are converged solutions obtained using a fine mesh of the planar cubic curved Timoshenko-Ehrenfest beam element proposed in the study of Vo and Nanakorn (2020). Specifically, 1,800 DOFs are used to obtain the reference solutions.

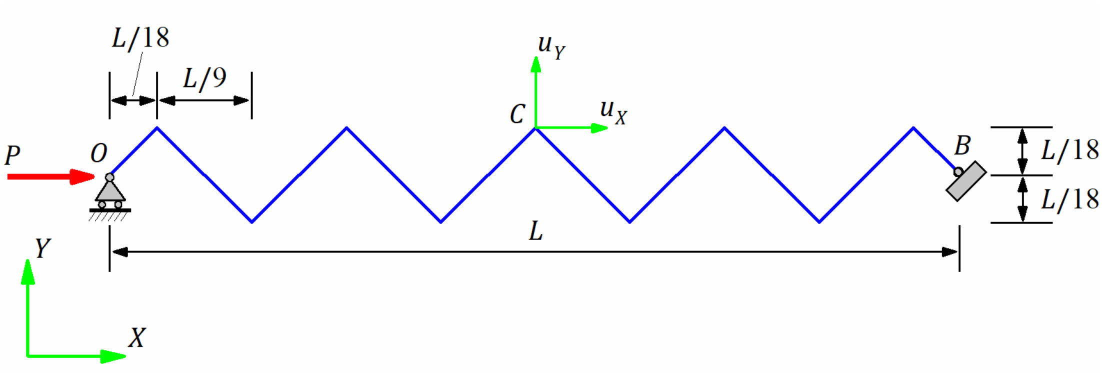

Figure 5.9 Problem 5.3.2: A zigzag frame.

In Figure 5.10, curves of normalized load and displacements of the frame axis at point C are exhibited. Here, $u_{0X,C}$ and $u_{0Y,C}$ represent the horizontal and the vertical displacements, respectively. The cross-sectional height h is set equal to $0.01L$. The performance of the varying-weight, constant-weight, and $\overline{\mathrm{B}}$ elements are compared by using four models detailed in Table 5.2. The magnified figures reveal that model VW of cubic varying-weight elements, provides accurate solutions, while CW1 employing cubic constant-weight elements with a comparable DOF number fails to achieve good solutions. The cubic constant-weight element needs at least model CW2, which consumes approximately 3 times more DOFs to reach the accuracy of VW. Furthermore, model BB of cubic $\overline{\mathrm{B}}$ elements consist of the same number of elements to model VW for a similar accuracy. While having smaller DOF number, BB consumes about 9 times more computational cost than VW.

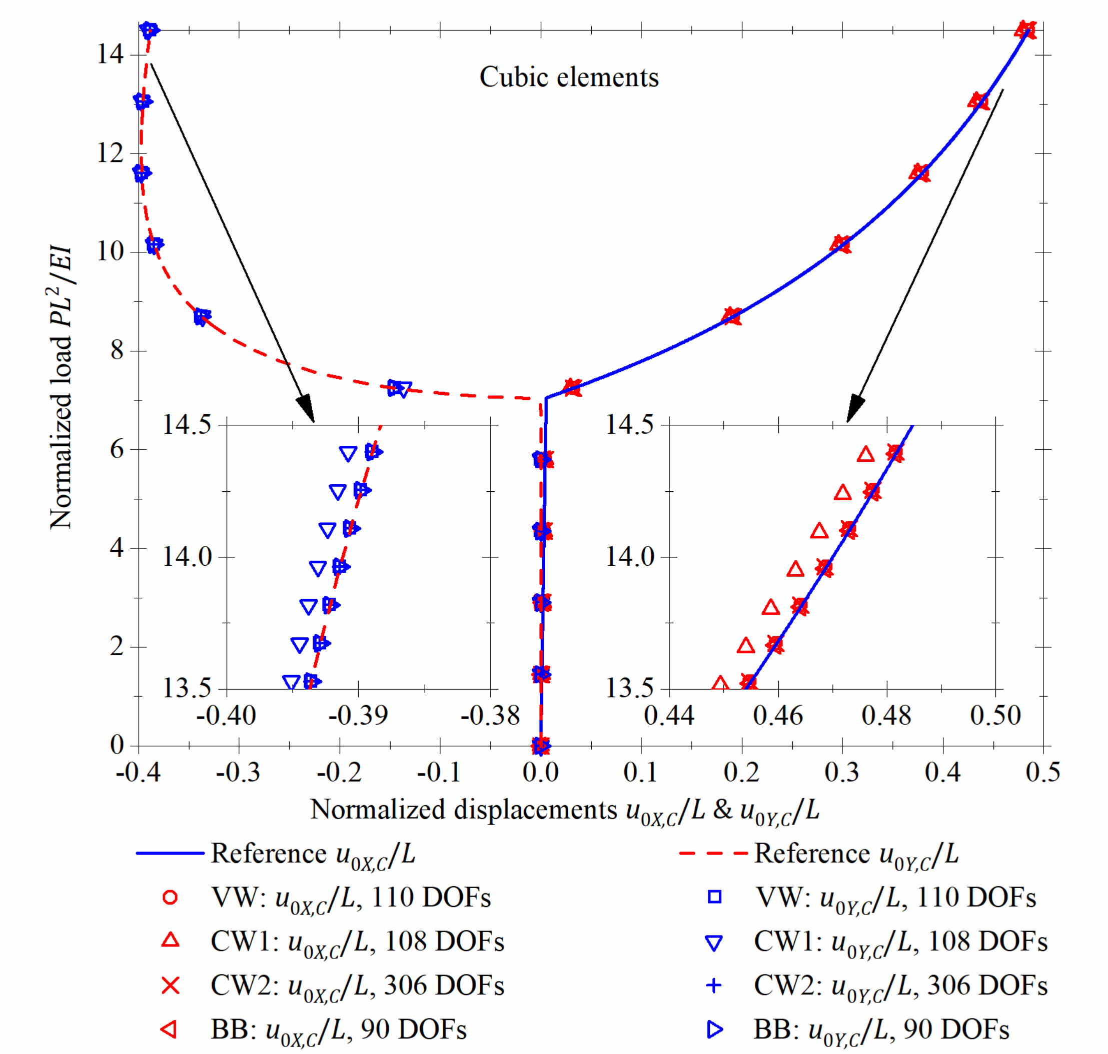

Figure 5.10 Problem 5.3.2: Normalized load-displacement curves of the beam axis at point C.

Several deformed configurations in response to different force magnitudes, yielded by using model VW, are illustrated in Figure 5.11. In Figure 5.11a-d, modest displacements are exhibited with the increase in applied force P. This underscores the substantial horizontal stiffness of the frame at this stage. However, in Figure 5.11d-h, the displacements amplify dramatically when P exceeds $7EI/L^2$. Indeed, this abrupt increase in displacements, as shown in Figure 5.10 and Figure 5.11d-h, is a consequence of exceeding a critical threshold of the applied force. At the beginning, i.e., $P < 7EI/L^2$, the force's orientation aligns with the frame's neutral line. Thus, the deformation at this stage resembles that of axial compression, which is typically proportional to the force's magnitude. When P exceeds $7EI/L^2$, significant vertical displacement occurs, leading to the asymmetry of deformed configurations. Consequently, the zigzag frame undergoes bucking and exhibits large displacements beyond those of a mere axial deformation.

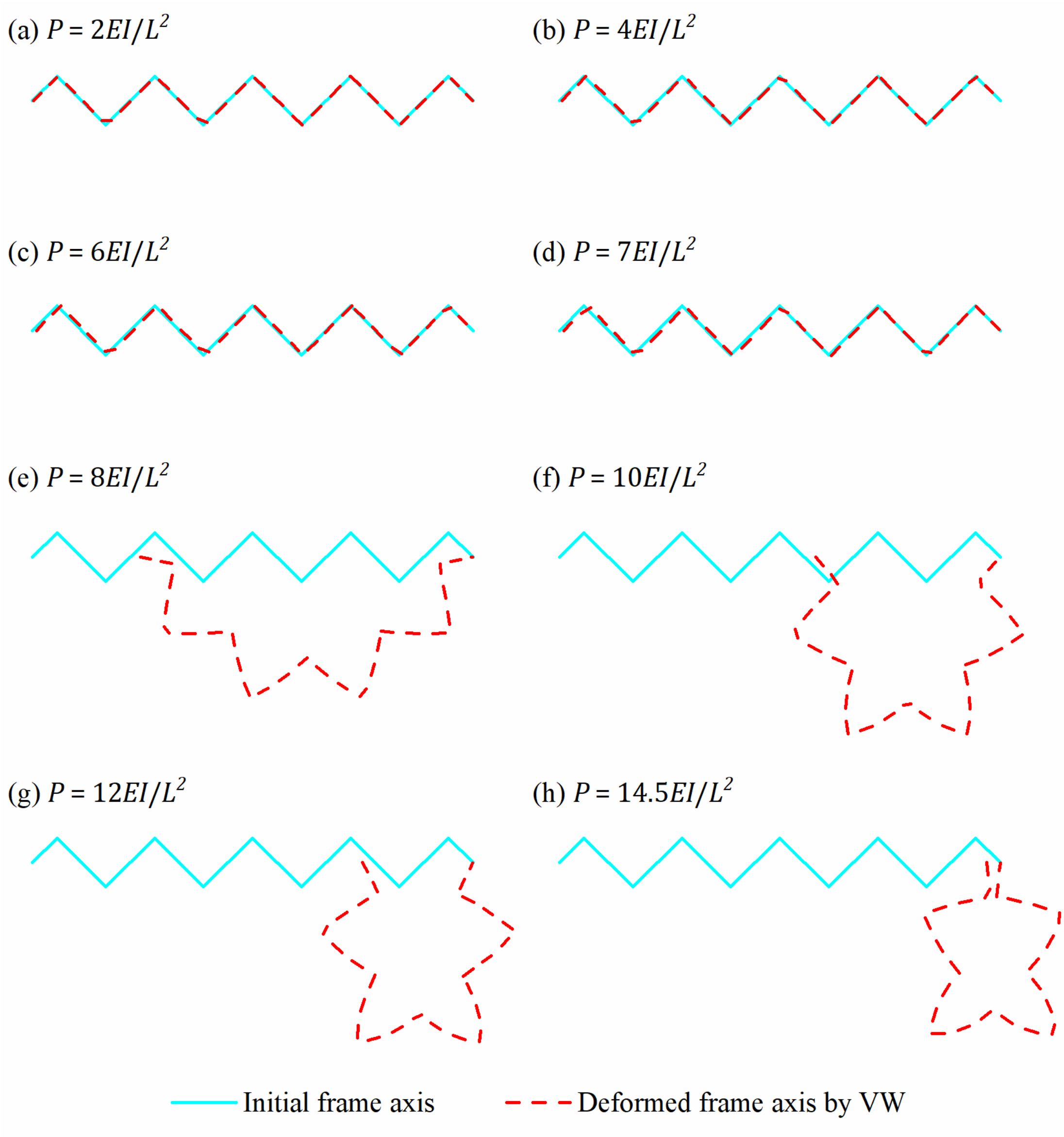

Figure 5.11 Problem 5.3.2: Deformed configurations of the zigzag frame corresponding to different magnitudes of P.

The final deformed frame axes, i.e., $P = 14.5EI/L^2$, given by the 4 models are sketched in Figure 5.12 where the superior accuracy of the varying-weight element over constant-weight element is again demonstrated. Evidently, the deformed frame axis obtained by CW1 is significantly different from the reference deformed frame axis. Conversely, the deformed axes produced by VW, CW2, and BB are visually indistinguishable from the reference one.

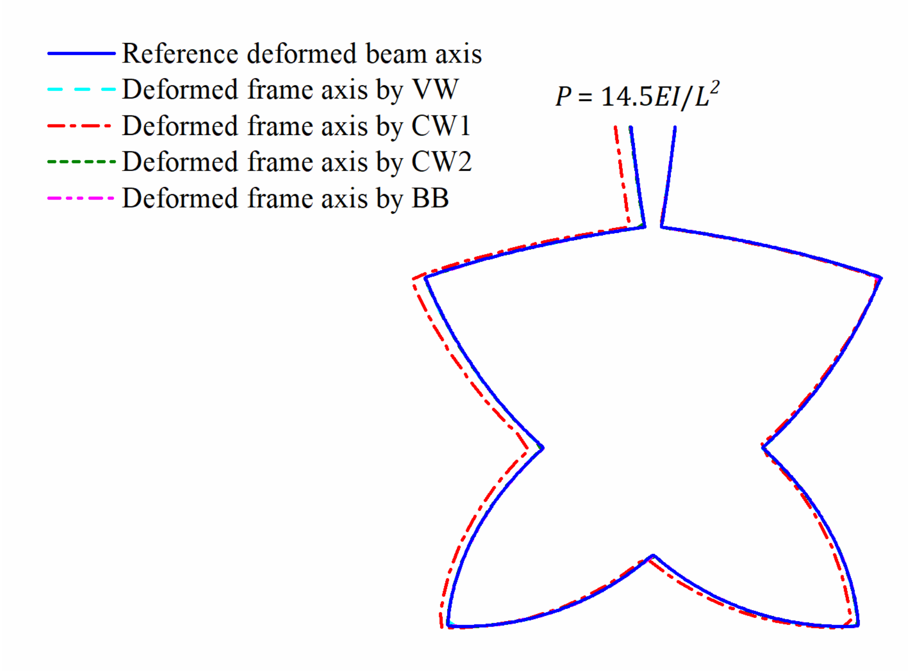

Figure 5.12 Problem 5.3.2: Final deformed frame axes given by using 4 models.

In the absence of analytical solutions, the convergence graphs are discouraged from examining the locking pathologies. It is crucial to recall that locking effects spuriously stiffen the elements, leading to failed representations of deformed kinematics and inaccurate solutions. Therefore, other manners of accuracy tests can be adopted for examining locking effects, such as utilizing deformed frame axes. Particularly, the final deformed frame axes, i.e., $P = 14.5EI/L^2$, given by the 4 models with different thickness values, i.e., $L/h = 100, 1000, 10000$ representing a very thin beam to an extremely thin beam, are considered and depicted in Figure 5.13. Note that the applied force $P = 14.5EI/L^2$ is a normalized value that yields the same displacements for different values of L/h. Therefore, for each model, the three deformed axes with respect to the three thickness values are compared for the difference. As evidenced in Figure 5.13a, model VW results in 3 identical deformed frame axes, implying no change in solutions due to the decrease in frame's thickness. Therefore, it unveils no locking effect. Conversely, in Figure 5.13b, CW1 totally fails to yield identical axes for different thickness values. The deformed frame axes with respect to $L/h = 1000$ and 10000 exhibit little deformations, which are remarkably different from the deformed axis corresponding to $L/h = 100$. In these two cases, little deformations imply great spurious stiffness of the frame and the severe locking effect. Moreover, locking effects turn lower when the number of cubic constant-weight elements increases, as revealed in Figure 5.13c with model CW2. Certainty, model BB of cubic $\overline{\mathrm{B}}$ elements addresses well locking effects, as shown in Figure 5.13d.

Different from the previous problem, the cubic constant-weight element cannot eliminate the locking pathologies in this problem with coarse meshes. Therefore, in this problem, using only cubic elements can effectively exhibit the superiority of the varying-weight element over the constant-weight element in mitigating the locking phenomena.

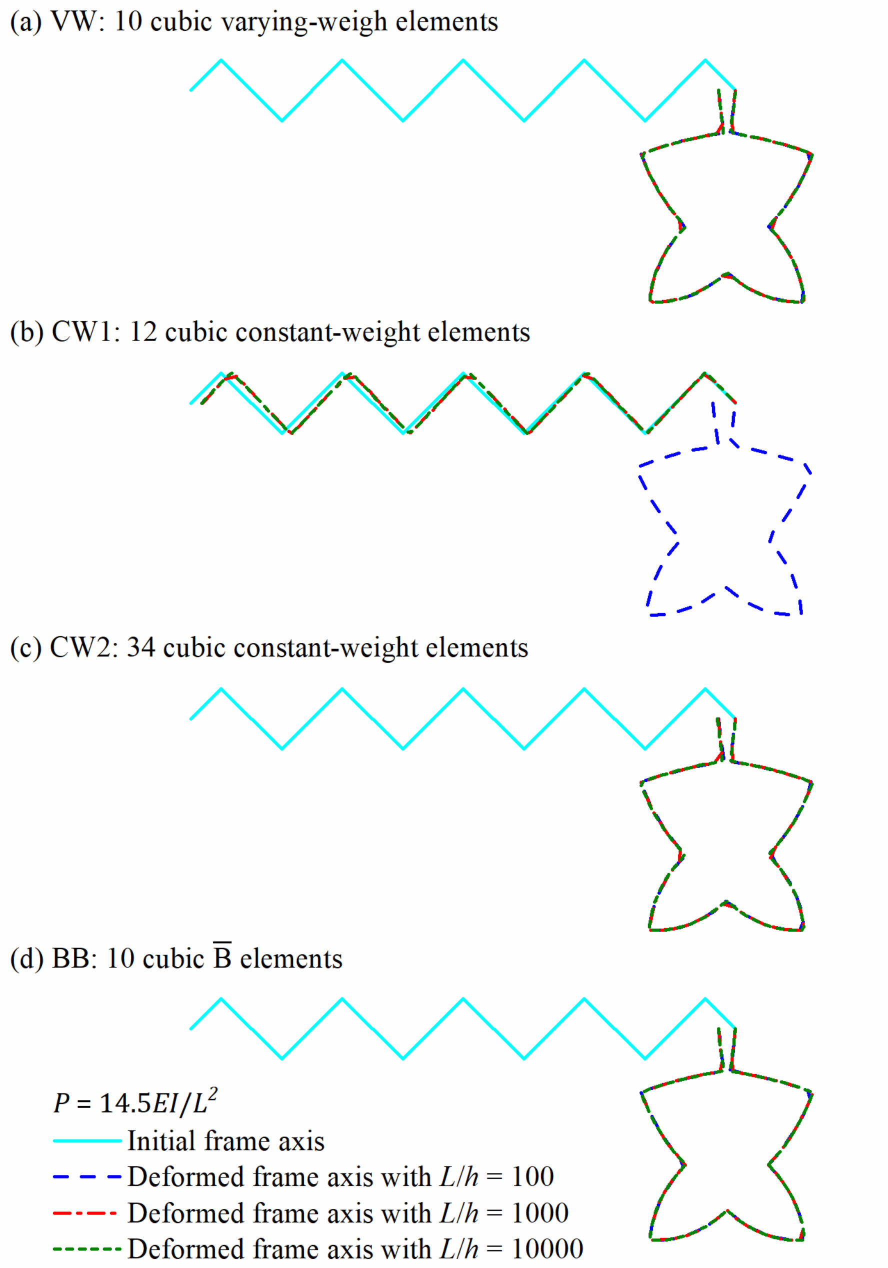

Figure 5.13 Problem 5.3.2: Final deformed frame axes given by using the 4 models with three different L/h ratios.

5.3.3 The snap behaviors of an S-shaped beam subjected to a downwardly concentrated force

The third problem involves an S-shaped beam applied by a downwardly concentrated force P, as shown in Figure 5.14. One end of the S-shaped beam (end O) is clamped, while the other end (end B) is assigned by a roller that constrains the horizontal movement. Additionally, a downwardly concentrated force P is applied at the end B.

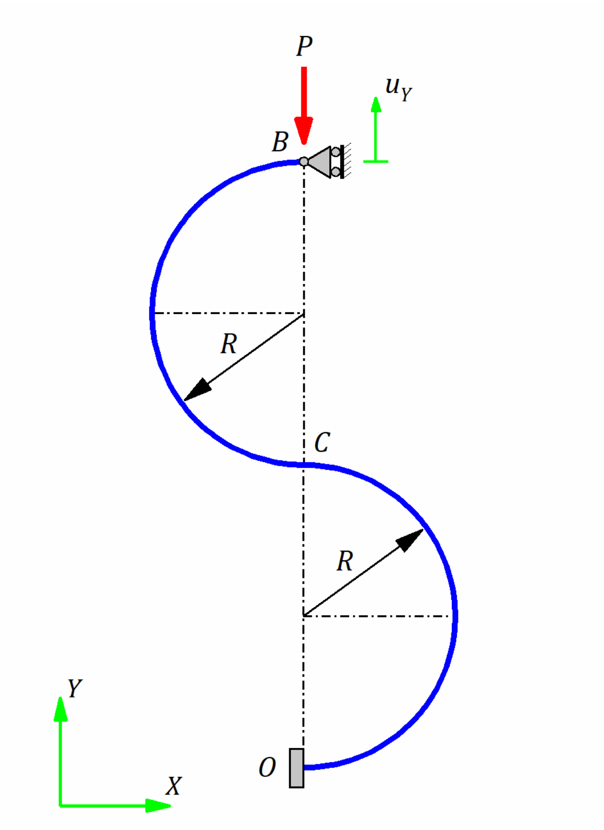

Figure 5.14 Problem 5.3.3: An S-shaped beam subjected to a downwardly concentrated force.

Four models of cubic elements, as detailed in Table 5.2, are employed to assess the performance of the varying-weight, constant-weight, and $\bar{\mathrm{B}}$ elements. The cross-sectional height h is set equal to $0.01R$. The appraisal focuses on the vertical displacement of the beam axis at the end B, denoted by $u_{0Y,B}$. Unlike the previous problem where buckling behavior occurs, this S-shape beam experiences the displacement snaps with several limit points. Consequently, solving this problem necessitates the utilization of the displacement control method to efficiently address these limit points, which is a difference from the force control method used in the previous two problems.

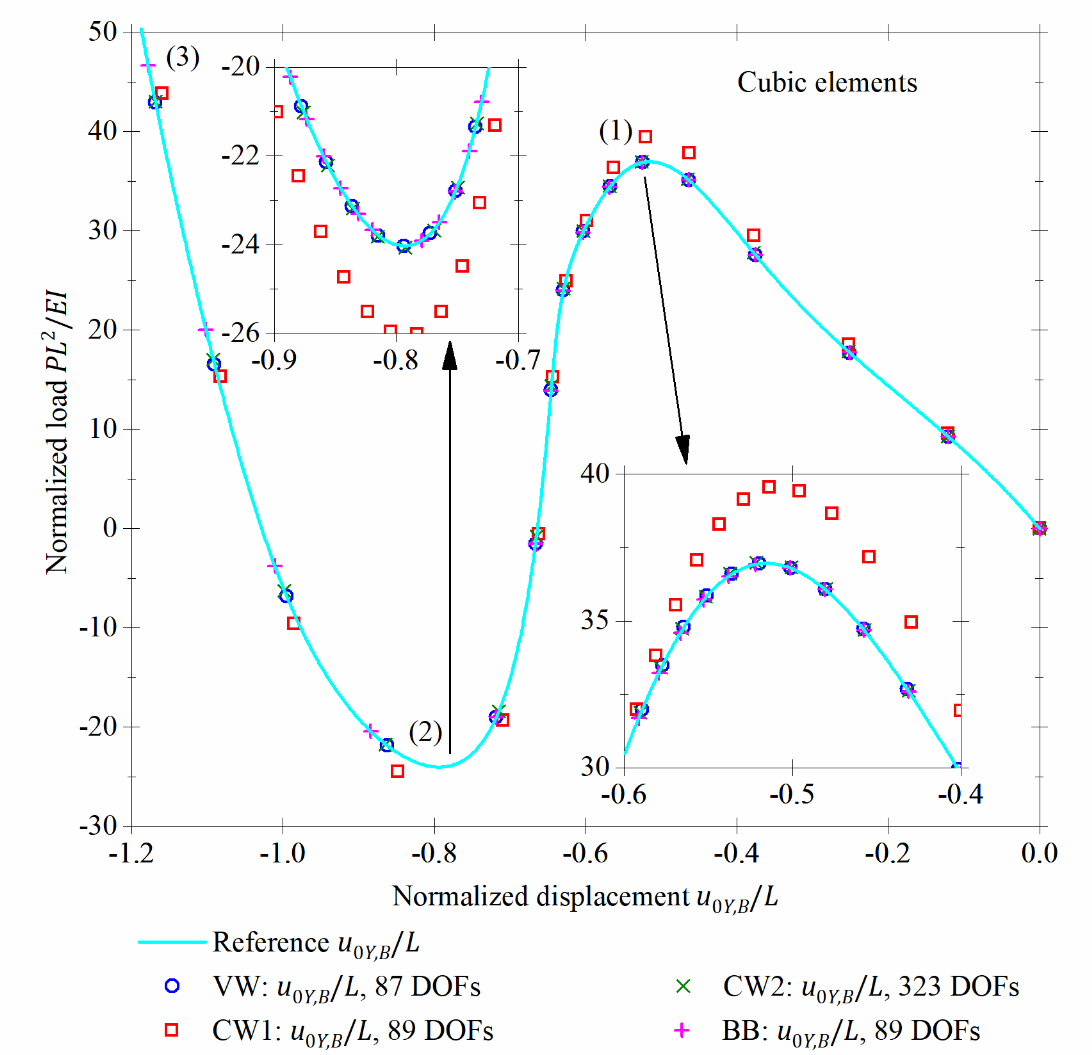

Figure 5.15 Problem 5.3.3: Normalized load-displacement curves of the beam axis at the end B.

In Figure 5.15, the curves depicting normalized load and displacement of the beam axis at the end B are presented. The reference solutions are obtained using the cubic planar curved Timoshenko-Ehrenfest beam element proposed in Vo and Nanakorn (2020) with 1,799 DOFs. From the enlarged figures, model VW of cubic varying-weight elements with 87 DOFs demonstrates remarkable accuracy as its solution strongly agrees with the reference solution. Conversely, despite consuming a similar DOF number, i.e., 89 DOFs, model CW1 of cubic constant-weight elements fails to accurately predict the solution, particularly in the vicinity of the limit points. Additionally, model CW2, also employing cubic constant-weight elements, achieves an accurate solution. However, CW2 consumes up to 323 DOFs, approximately 3.7 times higher than VW. Furthermore, upon achieving the accuracy level of VW with a similar DOF number, i.e., 89 DOFs, model BB consumes about 10 times more computational cost. The deformed configurations corresponding to the limit points (1) - (3), specified in Figure 5.15 and obtained by using model VW, are illustrated in Figure 5.16.

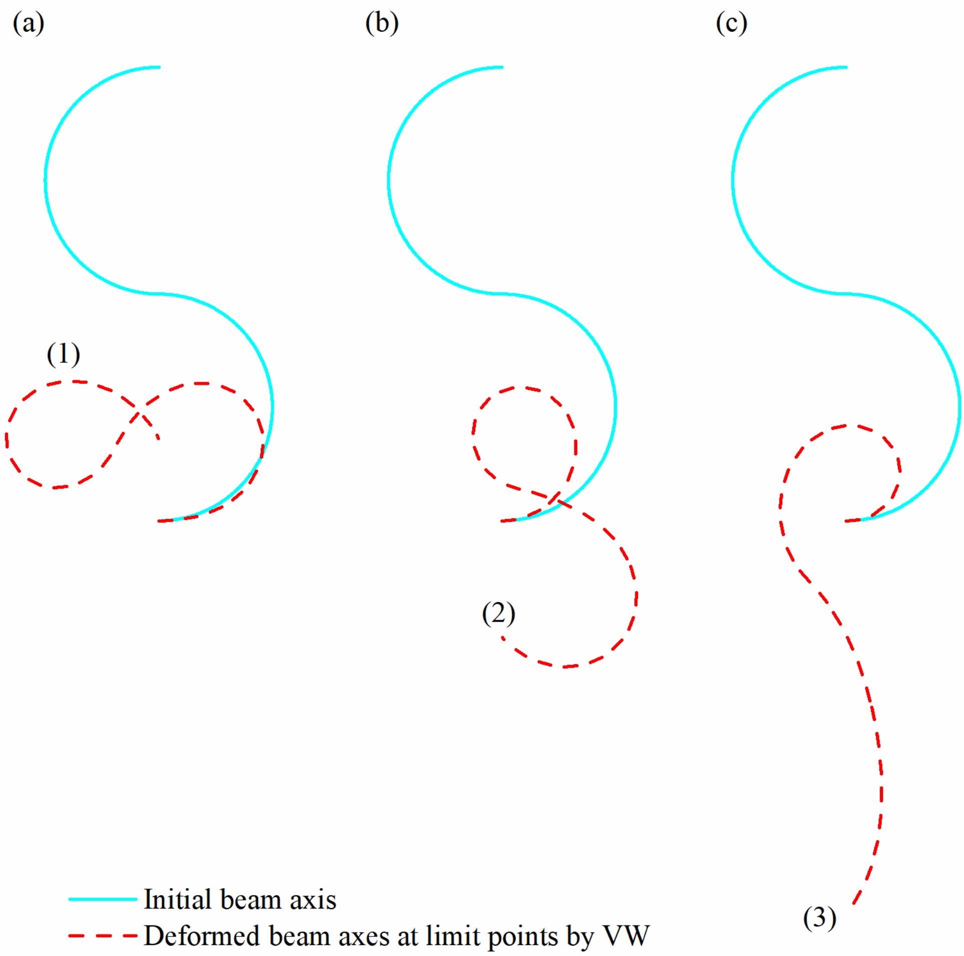

Figure 5.16 Problem 5.3.3: Deformed configurations at the limit points.

5.3.4 A spring in watches undergoing multiple snap behaviors

As unveiled in Figure 5.17, the last problem involves a spiral-like beam that is inspired by the torsion springs found in watches. The initial spiral axis is defined as

$$X(\phi) = R(1+\phi)\cos\phi \qquad\qquad Y(\phi) = R(1+\phi)\sin\phi. \tag{5.44}$$

Here, ϕ is set in the range from 0 to 4π, implying a two-cycle twist of the undeformed spiral. The cross-sectional height h is set equal to $0.1R$. Additionally, one end of the spiral (end O) is constrained by a pinned support, while the other end (end B) is fixed. End O is subjected to a concentrated moment M that induces the clockwise twist on the cross-section. Consequently, the cross-sectional rotation at O, denoted by θ_O, is examined to assess the elements. Four models of cubic elements are employed, as detailed in Table 5.2. Analogous to the previous problem, this problem undergoes snap behavior with multiple limit points, which require the utilization of the displacement control method.

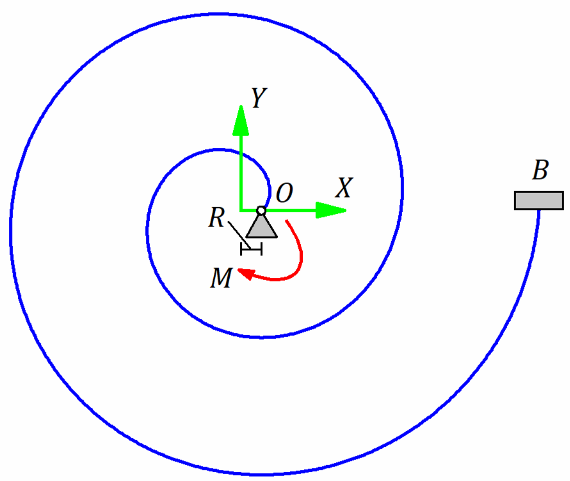

Figure 5.17 Problem 5.3.4: A spring in watches.

Figure 5.18 illustrates the curves of normalized load and cross-sectional rotation at O. The reference solution in the figure is obtained using the planar cubic curved Timoshenko-Ehrenfest beam element proposed in Vo and Nanakorn (2020) with 1,798 DOFs. The figure unveils displacement snaps, occurring at limit points, labeled as (1) - (7). The deformed configurations corresponding to some limit points, obtained using model VW, are depicted in Figure 5.19, showcasing the large and complex deformations. Moreover, in Figure 5.18, the superior accuracy of the varying-weight element over the constant-weight element is repeated. Concretely, model VW of cubic varying-weight elements with 284 DOFs yields a solution that closely matches the reference solution. Conversely, model CW1 of cubic constant-weight elements, with a comparable DOF number, fails to accurately predict the solution, particularly in the vicinity of the limit points. In this problem, for achieving the same accuracy level as VW, the cubic constant-weight element necessitates CW2 with up to 3.3 times more DOFs, while the cubic $\overline{\mathrm{B}}$ element needs model BB with slightly more DOFs but consuming about 8 times more computational cost.

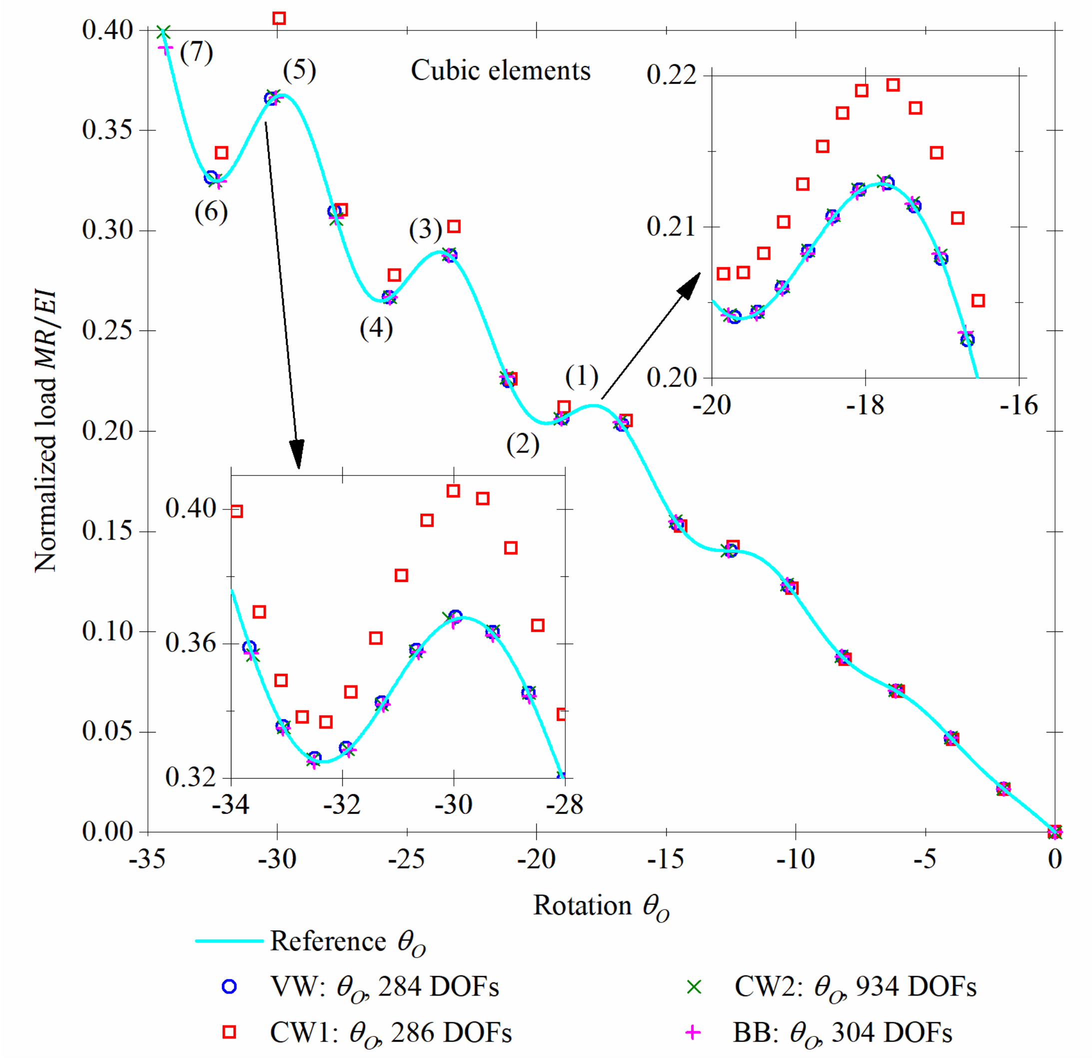

Figure 5.18 Problem 5.3.4: Curves of normalized load and cross-sectional rotation at O.

In contrast to problem 5.3.2, the other three problems demonstrate the superior accuracy of the cubic varying-weight element over the cubic $\overline{\mathrm{B}}$ element. Apparently, these three problems are initially curved structures, and undergo larger and more complex deformations than problem 5.3.2 having initially straight configuration. Generally, one can conclude that the accuracies of varying-weight elements and $\overline{\mathrm{B}}$ elements are comparable. Nonetheless, varying-weight elements are undoubtedly superior in terms of computational efficiency than $\overline{\mathrm{B}}$ elements. Therefore, in addition to the robust locking-free feature, varying-weight elements effectively address the trade-off between mitigating locking effects and maintaining computational efficiency, which is a significant challenge identified by Vo, Nanakorn, Bui and Rungamornrat (2022) in $\overline{\mathrm{B}}$ elements.

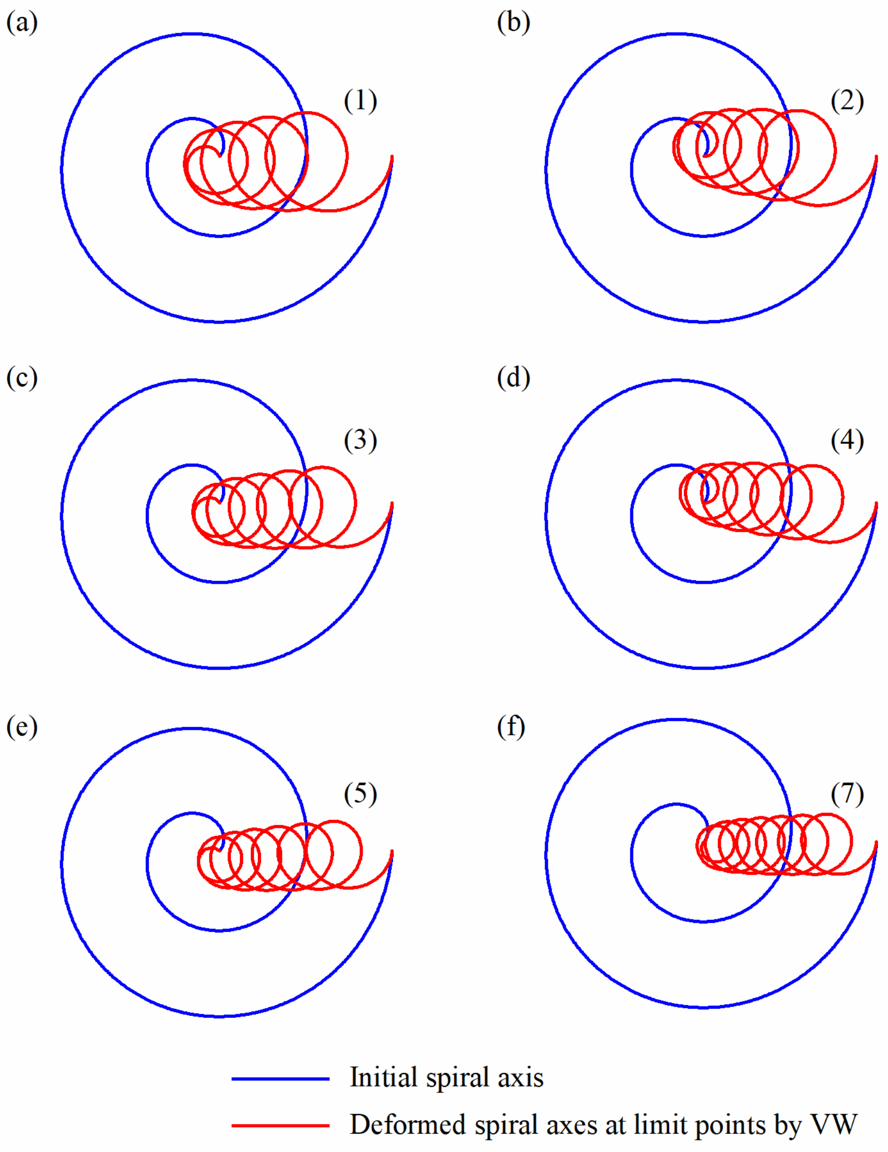

Figure 5.19 Problem 5.3.4: Deformed configurations at the limit points.

CHAPTER 6

CONCLUSIONS AND REMARKS

In this study, novel planar Euler-Bernoulli and Timoshenko-Ehrenfest beam elements are developed within curvilinear coordinate systems, for analyzing curved beam structures which undergo large displacements and small strains. Utilizing the total Lagrangian description, the kinematics are computed with respect to the initial configuration. In addition, the small-strain and thin-beam assumptions are employed that simplify the varied formulations. The kinematics of the beam elements are discretized using the isogeometric approach. Specifically, cubic NURBS representations are employed for the Euler-Bernoulli beam element, while quadratic and cubic NURBS representations are employed for Timoshenko-Ehrenfest beam elements.

The varying-weight concept is applied to enhance the approximation capacity of NURBS. Accordingly, weights of NURBS control points are selectively treated as DOFs, in such a way that weights of the first and the last control points are kept constant while weights of the other control points are relaxed. This new interpolation scheme highlights a key distinction between the proposed and conventional elements. The conventional elements, utilizing NURBS basis functions with constant weights, are referred to as constant-weight elements. Meanwhile, the proposed elements, incorporating some weights in NURBS as additional DOFs, are termed as varying-weight elements.

The efficiency of the proposed elements and the superiority of the proposed elements over the constant-weight elements are demonstrated by solving several beam problems. Specifically, five problems are solved with the Euler-Bernoulli beam elements, and four problems are solved with the Timoshenko-Ehrenfest beam elements. Overall, the solutions obtained demonstrate the efficiency of the proposed elements and underscore the robustness of the varying-weight concept. The varying-weight elements consistently outperform the constant-weight elements in terms of accuracy, particularly in extreme regions such as buckling points, limit points, or large displacements.

In Euler-Bernoulli beams, clear physical meanings of the derived strain components are provided. The cubic varying-weight element requires about 2.5 to 3 times fewer DOFs than the cubic constant-weight element to achieve accurate solutions. Its superiority is also evident in accurately yielding the strain measures. The cubic varying-weight element completely exhibits locking free. Conversely, the constant-weight counterpart occasionally shows a slight locking effect, as unveiled in problems 4.4.1 and 4.4.4.

In Timoshenko-Ehrenfest beams, the formulations with small-strain assumptions are simplified. Both the quadratic and cubic varying-weight elements require significantly fewer DOFs compared to their constant-weight counterparts for achieving accurate solutions. Additionally, these varying-weight elements effectively eliminate the locking pathologies giving them the eligibility to solve thin-beam problems. Furthermore, while exhibiting the locking-free characteristics but incurring many times lower computational costs, the accuracy of varying-weight elements is comparable to that of the locking-free $\overline{\mathrm{B}}$ elements. In particular, the cubic varying-weight element is found to consume equal to less DOFs to yield accurate solutions, when solving large and complex deformed problems such as problems 5.3.1, 5.3.3, and 5.3.4.

While the varying-weight concept in IGA has been exploited and shows its potential in producing higher accuracy of solutions compared to traditional IGA, so far, its applications are limited. To fully understand the potential of this concept on IGA, further research for 3D beams or other elements is promising.

REFERENCES

Adam, C., Bouabdallah, S., Zarroug, M., & Maitournam, H. (2014). Improved numerical integration for locking treatment in isogeometric structural elements, Part I: Beams. *Computer Methods in Applied Mechanics and Engineering*, 279, 1-28. https://doi.org/10.1016/j.cma.2014.06.023

Aköz, A. Y., Omurtag, M. H., & Doğruoğlu, A. N. (1991). The mixed finite element formulation for three-dimensional bars. *International Journal of Solids and Structures*, 28(2), 225-234. https://doi.org/10.1016/0020-7683(91)90207-V

Ashwell, D. G., & Gallagher, R. H. (1976). *Finite elements for thin shells and curved members*. Wiley.

Auricchio, F., Carotenuto, P., & Reali, A. (2008). On the geometrically exact beam model: A consistent, effective and simple derivation from three-dimensional finite-elasticity. *International Journal of Solids and Structures*, 45(17), 4766-4781. https://doi.org/10.1016/j.ijsolstr.2008.04.015

Babu, C. R., & Prathap, G. (1986). A linear thick curved beam element. *International Journal for Numerical Methods in Engineering*, 23(7), 1313-1328. https://doi.org/10.1002/nme.1620230709

Babu, C. R., Subramanian, G., & Prathap, G. (1987). Mechanics of field-consistency in finite element analysis—a penalty function approach. *Computers & Structures*, 25(2), 161-173. https://doi.org/10.1016/0045-7949(87)90139-8

Basar, Y., & Weichert, D. (2000). *Nonlinear continuum mechanics of solids: fundamental mathematical and physical concepts*. Springer Science & Business Media.

Bauchau, O. A., & Craig, J. I. (2009). *Euler-Bernoulli beam theory*. Springer.

Bauer, A., Breitenberger, M., Philipp, B., Wüchner, R., & Bletzinger, K.-U. (2016). Nonlinear isogeometric spatial Bernoulli beam. *Computer Methods in Applied Mechanics and Engineering*, 303, 101-127. https://doi.org/10.1016/j.cma.2015.12.027

Bauer, A. M., Wüchner, R., & Bletzinger, K. U. (2020). Weak coupling of nonlinear isogeometric spatial Bernoulli beams. *Computer Methods in Applied Mechanics and Engineering*, 361, 112747. https://doi.org/10.1016/j.cma.2019.112747

Bazilevs, Y., Beirao da Veiga, L., Cottrell, J. A., Hughes, T. J., & Sangalli, G. (2006). Isogeometric analysis: approximation, stability and error estimates for h-refined meshes. *Mathematical Models and Methods in Applied Sciences*, 16(07), 1031-1090. https://doi.org/10.1142/S0218202506001455

Belytschko, T., Liu, W. K., Moran, B., & Elkhodary, K. (2014). *Nonlinear finite elements for continua and structures*. John wiley & sons.

Benlemlih, A., & El Ferricha, M. E. A. (2002). A mixed finite element method for the arch problem. *Applied Mathematical Modelling*, 26(1), 17-36. https://doi.org/10.1016/S0307-904X(01)00039-7

Bergel, G. L., & Li, S. (2016). The total and updated Lagrangian formulations of state-based peridynamics. *Computational Mechanics*, 58(2), 351-370. https://doi.org/10.1007/s00466-016-1297-8

Biondi, B., & Caddemi, S. (2007). Euler–Bernoulli beams with multiple singularities in the flexural stiffness. *European Journal of Mechanics-A/Solids*, 26(5), 789-809. https://doi.org/10.1016/j.euromechsol.2006.12.005

Bletzinger, K.-U., Bischoff, M., & Ramm, E. (2000). A unified approach for shear-locking-free triangular and rectangular shell finite elements. *Computers & Structures*, 75(3), 321-334. https://doi.org/10.1016/S0045-7949(99)00140-6

Borković, A., Kovačević, S., Radenković, G., Milovanović, S., & Guzijan-Dilber, M. (2018). Rotation-free isogeometric analysis of an arbitrarily curved plane Bernoulli–Euler beam. *Computer Methods in Applied Mechanics and Engineering*, 334, 238-267. https://doi.org/10.1016/j.cma.2018.02.002

Borković, A., Kovačević, S., Radenković, G., Milovanović, S., & Majstorović, D. (2019). Rotation-free isogeometric dynamic analysis of an arbitrarily curved plane Bernoulli-Euler beam. *Engineering Structures*, 181, 192-215. https://doi.org/10.1016/j.engstruct.2018.12.003

Borković, A., Marussig, B., & Radenković, G. (2022). Geometrically exact static isogeometric analysis of an arbitrarily curved spatial Bernoulli–Euler beam.

Computer Methods in Applied Mechanics and Engineering, 390, 114447. https://doi.org/10.1016/j.cma.2021.114447

Borković, A., Marussig, B., & Radenković, G. (2022). Geometrically exact static isogeometric analysis of arbitrarily curved plane Bernoulli–Euler beam. *Thin-Walled Structures*, 170, 108539. https://doi.org/10.1016/j.tws.2021.108539

Bouclier, R., Elguedj, T., & Combescure, A. (2012). Locking free isogeometric formulations of curved thick beams. *Computer Methods in Applied Mechanics and Engineering*, 245, 144-162. https://doi.org/10.1016/j.cma.2012.06.008

Caillerie, D., Kotronis, P., & Cybulski, R. (2015). A Timoshenko finite element straight beam with internal degrees of freedom. *International Journal for Numerical and Analytical Methods in Geomechanics*, 39(16), 1753-1773. https://doi.org/10.1002/nag.2367

Carlson, N. (2009). NURBS surface fitting with Gauss-Newton. *Lulea University of Technology*

Cesnik, C. E. S., & Shin, S. (2001). On the modeling of integrally actuated helicopter blades. *International Journal of Solids and Structures*, 38(10), 1765-1789. https://doi.org/10.1016/S0020-7683(00)00135-9

Chad E, M., & Alex J, D. (2010). Accurate transfer maps for realistic beam-line elements: Straight elements. *Physical Review Accelerators and Beams*, 13(6), 064001. https://doi.org/10.1103/PhysRevSTAB.13.064001

Choi, M.-J., & Cho, S. (2019). Isogeometric configuration design sensitivity analysis of geometrically exact shear-deformable beam structures. *Computer Methods in Applied Mechanics and Engineering*, 351, 153-183. https://doi.org/10.1016/j.cma.2019.03.032

Choi, M.-J., & Cho, S. (2020). Isogeometric optimal design of compliant mechanisms using finite deformation curved beam built-up structures. *Journal of Mechanical Design*, 142(8), 081402. https://doi.org/10.1115/1.4043585

Choi, M.-J., Kang, S.-H., Oh, M.-H., & Cho, S. (2019). Controllable optimal design of auxetic structures for extremal Poisson's ratio of -2. *Composite Structures*, 226, 111215. https://doi.org/10.1016/j.compstruct.2019.111215

Choi, M.-J., Kim, J.-H., Koo, B., & Cho, S. (2021). Isogeometric configuration design optimization of three-dimensional curved beam structures for maximal fundamental frequency. *Structural and Multidisciplinary Optimization*, 63, 529-549. https://doi.org/10.1007/s00158-020-02803-0

Choi, M.-J., Sauer, R. A., & Klinkel, S. (2021). An isogeometric finite element formulation for geometrically exact Timoshenko beams with extensible directors. *Computer Methods in Applied Mechanics and Engineering*, 385, 113993. https://doi.org/10.1016/j.cma.2021.113993

Choit, J.-k., & Lim, J.-k. (1995). General curved beam elements based on the assumed strain fields. *Computers & Structures*, 55(3), 379-386. https://doi.org/10.1016/0045-7949(95)98865-N

Chorn, V., Vo, D., & Nanakorn, P. (2021). A total Lagrangian isogeometric Timoshenko beam formulation for large displacement analysis of 2D frames. *Proceeding of EASEC16* (pp. 961-968). Springer.

Cottrell, J. A., Hughes, T. J., & Bazilevs, Y. (2009). *Isogeometric analysis: toward integration of CAD and FEA*. John Wiley & Sons.

Da Veiga, L. B., Buffa, A., Sangalli, G., & Vázquez, R. (2014). Mathematical analysis of variational isogeometric methods. *Acta Numerica*, 23, 157-287. https://doi.org/10.1017/S096249291400004X

Davis, R., Henshell, R., & Warburton, G. (1972). A Timoshenko beam element. *Journal of Sound and Vibration*, 22(4), 475-487. https://doi.org/10.1016/0022-460X(72)90457-9

Dimas, E., & Briassoulis, D. (1999). 3D geometric modelling based on NURBS: a review. *Advances in Engineering Software*, 30(9-11), 741-751. https://doi.org/10.1016/S0965-9978(98)00110-0

Dimitri, R., De Lorenzis, L., Scott, M. A., Wriggers, P., Taylor, R. L., & Zavarise, G. (2014). Isogeometric large deformation frictionless contact using T-splines. *Computer Methods in Applied Mechanics and Engineering*, 269, 394-414. https://doi.org/10.1016/j.cma.2013.11.002

Doğruoğlu, A. N., & Kömürcü, S. (2019). Nonlinear mixed finite element formulations for the analysis of planar curved beams. *Computers & Structures*, 222, 63-81. https://doi.org/10.1016/j.compstruc.2019.06.001

Echter, R., & Bischoff, M. (2010). Numerical efficiency, locking and unlocking of NURBS finite elements. *Computer Methods in Applied Mechanics and Engineering*, 199(5-8), 374-382. https://doi.org/10.1016/j.cma.2009.02.035

Elishakoff, I. (2020). Who developed the so-called Timoshenko beam theory? *Mathematics and Mechanics of Solids*, 25(1), 97-116. https://doi.org/10.1177/1081286519856931

Elkaranshawy, H. A., Elerian, A. A., & Hussien, W. I. (2018). A corotational formulation based on Hamilton's principle for geometrically nonlinear thin and thick planar beams and frames. *Mathematical Problems in Engineering*, 2018, 2670462. https://doi.org/10.1155/2018/2670462

Farin, G. (1992). From conics to NURBS: A tutorial and survey. *IEEE Computer Graphics and Applications*, 12(5), 78-86.

Flanagan, D. P., & Belytschko, T. (1981). A uniform strain hexahedron and quadrilateral with orthogonal hourglass control. *International Journal for Numerical Methods in Engineering*, 17(5), 679-706. https://doi.org/10.1002/nme.1620170504

Fußeder, D., Simeon, B., & Vuong, A. V. (2015). Fundamental aspects of shape optimization in the context of isogeometric analysis. *Computer Methods in Applied Mechanics and Engineering*, 286, 313-331. https://doi.org/10.1016/j.cma.2014.12.028

Greco, L. (2020). An iso-parametric G1-conforming finite element for the nonlinear analysis of Kirchhoff rod. Part I: the 2D case. *Continuum Mechanics and Thermodynamics*, 1-24. https://doi.org/10.1007/s00161-020-00861-9

Greco, L., & Cuomo, M. (2013). B-Spline interpolation of Kirchhoff-Love space rods. *Computer Methods in Applied Mechanics and Engineering*, 256, 251-269. https://doi.org/10.1016/j.cma.2012.11.017

Greco, L., & Cuomo, M. (2014). An implicit G1 multi patch B-spline interpolation for Kirchhoff–Love space rod. *Computer Methods in Applied Mechanics and Engineering*, 269, 173-197. https://doi.org/10.1016/j.cma.2013.09.018

Greco, L., Cuomo, M., Contrafatto, L., & Gazzo, S. (2017). An efficient blended mixed B-spline formulation for removing membrane locking in plane curved

Kirchhoff rods. *Computer Methods in Applied Mechanics and Engineering*, 324, 476-511. https://doi.org/10.1016/j.cma.2017.06.032

Greco, L., Scrofani, A., & Cuomo, M. (2021). A non-linear symmetric G1-conforming Bézier finite element formulation for the analysis of Kirchhoff beam assemblies. *Computer Methods in Applied Mechanics and Engineering*, 387, 114176. https://doi.org/10.1016/j.cma.2021.114176

Han, X.-A., Ma, Y., & Huang, X. (2008). A novel generalization of Bézier curve and surface. *Journal of Computational and Applied Mathematics*, 217(1), 180-193. https://doi.org/10.1016/j.cam.2007.06.027

Hartley, P., & Judd, C. (1980). Parametrization and shape of B-spline curves for CAD. *Computer-Aided Design*, 12(5), 235-238. https://doi.org/10.1016/0010-4485(80)90028-7

Higham, D. J., & Higham, N. J. (2016). *MATLAB guide*. SIAM.

Hodges, D. H. (2006). *Nonlinear composite beam theory*. American Institute of Aeronautics and Astronautics.

Hongsen, K. (2020). Comparison of isogeometric method and finite element analysis on beams over elastic foundations based on UI approach. *Proceeding of UI Proceedings on Science and Technology* (pp.

Hu, P., Hu, Q., & Xia, Y. (2016). Order reduction method for locking free isogeometric analysis of Timoshenko beams. *Computer Methods in Applied Mechanics and Engineering*, 308, 1-22. https://doi.org/10.1016/j.cma.2016.05.010

Hughes, T. J., Cottrell, J. A., & Bazilevs, Y. (2005). Isogeometric analysis: CAD, finite elements, NURBS, exact geometry and mesh refinement. *Computer Methods in Applied Mechanics and Engineering*, 194(39-41), 4135-4195. https://doi.org/10.1016/j.cma.2004.10.008

Hughes, T. J. R. (1980). Generalization of selective integration procedures to anisotropic and nonlinear media. *International Journal for Numerical Methods in Engineering*, 15(9), 1413-1418. https://doi.org/10.1002/nme.1620150914

Hughes, T. J. R. (2012). *The finite element method: Linear static and dynamic finite element analysis*. Dover Publications.

Hutchinson, J. (2001). Shear coefficients for Timoshenko beam theory. *J. Appl. Mech.*, 68(1), 87-92. https://doi.org/10.1115/1.1349417

Irschik, H., & Gerstmayr, J. (2009). A continuum mechanics based derivation of Reissner's large-displacement finite-strain beam theory: the case of plane deformations of originally straight Bernoulli–Euler beams. *Acta Mechanica*, 206(1-2), 1-21. https://doi.org/10.1007/s00707-008-0085-8

Ishaquddin, M., Raveendranath, P., & Reddy, J. N. (2012). Flexure and torsion locking phenomena in out-of-plane deformation of Timoshenko curved beam element. *Finite Elements in Analysis and Design*, 51, 22-30. https://doi.org/10.1016/j.finel.2011.11.002

Ishaquddin, M., Raveendranath, P., & Reddy, J. N. (2013). Coupled polynomial field approach for elimination of flexure and torsion locking phenomena in the Timoshenko and Euler–Bernoulli curved beam elements. *Finite Elements in Analysis and Design*, 65, 17-31. https://doi.org/10.1016/j.finel.2012.10.005

Jočković, M. M. (2021). Isogeometric approach in dynamic analysis of spatial curved beams. *Univerzitet u Beogradu-Građevinski fakultet*

Júnior, C. J. F., Cardozo, A. C. P., Júnior, V. M., & Neto, A. G. (2019). Modeling wind turbine blades by geometrically-exact beam and shell elements: A comparative approach. *Engineering Structures*, 180, 357-378. https://doi.org/10.1016/j.engstruct.2018.09.032

Kacprzyk, Z., & Ostapska-Łuczkowska, K. (2014). Isogeometric analysis as a new FEM formulation-simple problems of steady state thermal analysis. *Procedia Engineering*, 91, 87-92. https://doi.org/10.1016/j.proeng.2014.12.018

Karamanlidis, D., & Jasti, R. (1987). Curved mixed beam elements for the analysis of thin-walled free-form arches. *Ingenieur-Archiv*, 57(5), 361-367. https://doi.org/10.1007/BF00533948

Kiendl, J., Auricchio, F., Hughes, T. J. R., & Reali, A. (2015). Single-variable formulations and isogeometric discretizations for shear deformable beams. *Computer Methods in Applied Mechanics and Engineering*, 284, 988-1004. https://doi.org/10.1016/j.cma.2014.11.011

Kiendl, J., Auricchio, F., & Reali, A. (2018). A displacement-free formulation for the Timoshenko beam problem and a corresponding isogeometric collocation approach. *Meccanica*, 53, 1403-1413. https://doi.org/10.1007/s11012-017-0745-7

Kim, D.-S., & Kang, S.-H. (2011). A characterization of conic sections. *Honam Mathematical Journal*, 33(3), 335-340. https://doi.org/10.5831/HMJ.2011.33.3.335

Kim, J. G., & Kim, Y. Y. (1998). A new higher-order hybrid-mixed curved beam element. *International Journal for Numerical Methods in Engineering*, 43(5), 925-940. https://doi.org/10.1002/(SICI)1097-0207(19981115)43:5%3C925::AID-NME457%3E3.0.CO;2-M

Kim, N.-I. (2010). Shear and membrane locking-free thin-walled curved beam element based on assumed strain fields#. *Mechanics Based Design of Structures and Machines*, 38(3), 273-299. https://doi.org/10.1080/15397731003670576

Kopmaz, O., & Gündoğdu, Ö. (2003). On the curvature of an Euler–Bernoulli beam. *International Journal of Mechanical Engineering Education*, 31(2), 132-142. https://doi.org/10.7227/IJMEE.31.2.5

Koschnick, F., Bischoff, M., Camprubí, N., & Bletzinger, K.-U. (2005). The discrete strain gap method and membrane locking. *Computer Methods in Applied Mechanics and Engineering*, 194(21-24), 2444-2463. https://doi.org/10.1016/j.cma.2004.07.040

Labuschagne, A., van Rensburg, N. J., & Van der Merwe, A. (2009). Comparison of linear beam theories. *Mathematical and Computer Modelling*, 49(1-2), 20-30. https://doi.org/10.1016/j.mcm.2008.06.006

Lebedev, L. P., Cloud, M. J., & Eremeyev, V. A. (2010). *Tensor analysis with applications in mechanics*. World Scientific.

Li, X., & Sederberg, T. W. (2019). S-splines: A simple surface solution for IGA and CAD. *Computer Methods in Applied Mechanics and Engineering*, 350, 664-678. https://doi.org/10.1016/j.cma.2019.03.035

Lian, H., Kerfriden, P., & Bordas, S. (2017). Shape optimization directly from CAD: An isogeometric boundary element approach using T-splines. *Computer Methods in Applied Mechanics and Engineering*, 317, 1-41. https://doi.org/10.1016/j.cma.2016.11.012

Ma, W., & Kruth, J.-P. (1998). NURBS curve and surface fitting for reverse engineering. *The International Journal of Advanced Manufacturing Technology*, 14(12), 918-927. https://doi.org/10.1007/BF01179082

Magisano, D., Leonetti, L., & Garcea, G. (2021). Isogeometric analysis of 3D beams for arbitrarily large rotations: Locking-free and path-independent solution without displacement DOFs inside the patch. *Computer Methods in Applied Mechanics and Engineering*, 373, 113437. https://doi.org/10.1016/j.cma.2020.113437

Magisano, D., Leonetti, L., Madeo, A., & Garcea, G. (2020). A large rotation finite element analysis of 3D beams by incremental rotation vector and exact strain measure with all the desirable features. *Computer Methods in Applied Mechanics and Engineering*, 361, 112811. https://doi.org/10.1016/j.cma.2019.112811

Marino, E. (2016). Isogeometric collocation for three-dimensional geometrically exact shear-deformable beams. *Computer Methods in Applied Mechanics and Engineering*, 307, 383-410. https://doi.org/10.1016/j.cma.2016.04.016

Marino, E. (2017). Locking-free isogeometric collocation formulation for three-dimensional geometrically exact shear-deformable beams with arbitrary initial curvature. *Computer Methods in Applied Mechanics and Engineering*, 324, 546-572. https://doi.org/10.1016/j.cma.2017.06.031

Meck, H. R. (1980). An accurate polynomial displacement function for unite ring elements. *Computers & Structures*, 11(4), 265-269. https://doi.org/10.1016/0045-7949(80)90076-0

Miao, D., Borden, M. J., Scott, M. A., & Thomas, D. C. (2018). Bézier $\bar{B}$ projection. *Computer Methods in Applied Mechanics and Engineering*, 335, 273-297. https://doi.org/10.1016/j.cma.2018.02.019

Nagy, A. P., Abdalla, M. M., & Gürdal, Z. (2010). Isogeometric sizing and shape optimisation of beam structures. *Computer Methods in Applied Mechanics and Engineering*, 199(17-20), 1216-1230. https://doi.org/10.1016/j.cma.2009.12.010

Nagy, A. P., Abdalla, M. M., & Gürdal, Z. (2010). On the variational formulation of stress constraints in isogeometric design. *Computer Methods in Applied Mechanics and Engineering*, 199(41-44), 2687-2696. https://doi.org/10.1016/j.cma.2010.05.012

Nagy, A. P., Abdalla, M. M., & Gürdal, Z. (2011). Isogeometric design of elastic arches for maximum fundamental frequency. *Structural and Multidisciplinary Optimization*, 43, 135-149. https://doi.org/10.1007/s00158-010-0549-z

Nagy, A. P., IJsselmuiden, S. T., & Abdalla, M. M. (2013). Isogeometric design of anisotropic shells: optimal form and material distribution. *Computer Methods in Applied Mechanics and Engineering*, 264, 145-162. https://doi.org/10.1016/j.cma.2013.05.019

Nanakorn, P., & Vu, L. (2006). A 2D field-consistent beam element for large displacement analysis using the total Lagrangian formulation. *Finite Elements in Analysis and Design*, 42(14-15), 1240-1247. https://doi.org/10.1016/j.finel.2006.06.002

Nguyen, V. P., Anitescu, C., Bordas, S. P., & Rabczuk, T. (2015). Isogeometric analysis: an overview and computer implementation aspects. *Mathematics and Computers in Simulation*, 117, 89-116. https://doi.org/10.1016/j.matcom.2015.05.008

Noguchi, H., & Hisada, T. (1995). Integrated FEM formulation for total/updated-lagrangian method in geometrically nonlinear problems. *JSME International Journal. Ser. A, Mechanics and Material Engineering*, 38(1), 23-29. https://doi.org/10.1299/jsmea1993.38.1_23

Noor, A. K., & Peters, J. M. (1981). Mixed models and reduced/selective integration displacement models for nonlinear analysis of curved beams. *International Journal for Numerical Methods in Engineering*, 17(4), 615-631. https://doi.org/10.1002/nme.1620170409

Nukala, P. K. V. V., & White, D. W. (2004). A mixed finite element for three-dimensional nonlinear analysis of steel frames. *Computer Methods in Applied Mechanics and Engineering*, 193(23), 2507-2545. https://doi.org/10.1016/j.cma.2004.01.029

Pai, P. F., Anderson, T. J., & Wheater, E. A. (2000). Large-deformation tests and total-Lagrangian finite-element analyses of flexible beams. *International Journal of Solids and Structures*, 37(21), 2951-2980. https://doi.org/10.1016/S0020-7683(99)00115-8

Piegl, L. (1991). On NURBS: a survey. *IEEE Computer Graphics and Applications*, 11(01), 55-71. https://doi.org/10.1109/38.67702

Piegl, L., & Tiller, W. (1996). *The NURBS book*. Springer Science & Business Media.

Prathap, G. (1985). The curved beam/deep arch/finite ring element revisited. *International Journal for Numerical Methods in Engineering*, 21(3), 389-407. https://doi.org/10.1002/nme.1620210302

Prathap, G., & Bhashyam, G. R. (1982). Reduced integration and the shear-flexible beam element. *International Journal for Numerical Methods in Engineering*, 18(2), 195-210. https://doi.org/10.1002/nme.1620180205

Prathap, G., & Naganarayana, B. P. (1990). Analysis of locking and stress oscillations in a general curved beam element. *International Journal for Numerical Methods in Engineering*, 30(1), 177-200. https://doi.org/10.1002/nme.1620300111

Prautzsch, H., Boehm, W., & Paluszny, M. (2002). *Bézier and B-spline techniques*. Springer.

Qian, X. (2010). Full analytical sensitivities in NURBS based isogeometric shape optimization. *Computer Methods in Applied Mechanics and Engineering*, 199(29-32), 2059-2071. https://doi.org/10.1016/j.cma.2010.03.005

Radenković, G., & Borković, A. (2018). Linear static isogeometric analysis of an arbitrarily curved spatial Bernoulli–Euler beam. *Computer Methods in Applied Mechanics and Engineering*, 341, 360-396. https://doi.org/10.1016/j.cma.2018.07.010

Reddy, J. N. (2017). *Energy principles and variational methods in applied mechanics*. John Wiley & Sons.

Reissner, E. (1972). On one-dimensional finite-strain beam theory: the plane problem. *Zeitschrift Für Angewandte Mathematik und Physik ZAMP*, 23(5), 795-804. https://doi.org/10.1007/BF01602645

Ren, H., Shou, H., & Lin, H. (2022). A Review of T-spline Surfaces. *Recent Patents on Engineering*, 16(5), 67-75. https://doi.org/10.2174/1872212115666210707110158

Rogers, D. F. (2001). *An introduction to NURBS: with historical perspective*. Morgan Kaufmann.

Routh, O. U. (2016). *Matrix Algorithms in MATLAB*. Academic Press.

Rust, W. (2015). *Non-linear finite element analysis in structural mechanics*. Springer.

Sabale, A., & Gopal, K. V. N. (2019). Nonlinear aeroelastic response of wind turbines using Simo-Vu-Quoc rods. *Applied Mathematical Modelling*, 65, 696-716. https://doi.org/10.1016/j.apm.2018.09.003

Sederberg, T. W., Zheng, J., Bakenov, A., & Nasri, A. (2003). T-splines and T-NURCCs. *ACM Transactions on Graphics*, 22(3), 477-484. https://doi.org/10.1145/882262.882295

Simo, J., & Vu-Quoc, L. (1986). On the dynamics of flexible beams under large overall motions—The plane case: Part I. *Journal of Applied Mechanics*, 53(4), 849-854. https://doi.org/10.1115/1.3171870

Simo, J., & Vu-Quoc, L. (1986). On the dynamics of flexible beams under large overall motions—The plane case: Part II. *Journal of Applied Mechanics*, 53(4), 855-863. https://doi.org/10.1115/1.3171871

Simo, J. C. (1985). A finite strain beam formulation. The three-dimensional dynamic problem. Part I. *Computer Methods in Applied Mechanics and Engineering*, 49(1), 55-70. https://doi.org/10.1016/0045-7825(85)90050-7

Simo, J. C., & Hughes, T. J. R. (1986). On the variational foundations of assumed strain methods. *Journal of Applied Mechanics*, 53(1), 51-54. https://doi.org/10.1115/1.3171737

Stolarski, H., & Belytschko, T. (1982). Membrane locking and reduced integration for curved elements. *Journal of Applied Mechanics*, 49(1), 172-176. https://doi.org/10.1115/1.3161961

Taheri, A. H., Abolghasemi, S., & Suresh, K. (2020). Generalizations of non-uniform rational B-splines via decoupling of the weights: theory, software and applications. *Engineering with Computers*, 36(4), 1831-1848. https://doi.org/10.1007/s00366-019-00799-w

Taheri, A. H., & Suresh, K. (2020). Adaptive w-refinement: A new paradigm in isogeometric analysis. *Computer Methods in Applied Mechanics and Engineering*, 368, 113180. https://doi.org/10.1016/j.cma.2020.113180

Taheri, A. H., & Suresh, K. (2022). Surface approximations using generalized NURBS. *Engineering with Computers*, 38(5), 4221-4239. https://doi.org/10.1007/s00366-021-01483-8

Ten Thije, R., Akkerman, R., & Huétink, J. (2007). Large deformation simulation of anisotropic material using an updated Lagrangian finite element method. *Computer Methods in Applied Mechanics and Engineering*, 196(33-34), 3141-3150. https://doi.org/10.1016/j.cma.2007.02.010

Thomas, D., Wilson, J., & Wilson, R. (1973). Timoshenko beam finite elements. *Journal of Sound and Vibration*, 31(3), 315-330. https://doi.org/10.1016/0022-460X(72)90457-9

Thomas, D. C., Engvall, L., Schmidt, S. K., Tew, K., & Scott, M. A. (2022). U-splines: Splines over unstructured meshes. *Computer Methods in Applied Mechanics and Engineering*, 401, 115515. https://doi.org/10.1016/j.cma.2022.115515

Thompson, J. F. (1982). General curvilinear coordinate systems. *Applied Mathematics and Computation*, 10, 1-30. https://doi.org/10.1016/0096-3003(82)90185-0

Timoshenko, S. P. (1958). *Strength of materials. Part 1: Elementary theory and problems*. New York: Van Nostrand Company Inc.

Torkamani, M. A., & Sonmez, M. (2008). Solution techniques for nonlinear equilibrium equations. *Proceeding of Structures Congress 2008: 18th Analysis and Computation Specialty Conference* (pp. 1-17).

Urthaler, Y., & Reddy, J. (2005). A corotational finite element formulation for the analysis of planar beams. *Communications in Numerical Methods in Engineering*, 21(10), 553-570. https://doi.org/10.1002/cnm.773

Vo, D., Borković, A., Nanakorn, P., & Bui, T. Q. (2020). Dynamic multi-patch isogeometric analysis of planar Euler–Bernoulli beams. *Computer Methods in Applied Mechanics and Engineering*, 372, 113435. https://doi.org/10.1016/j.cma.2020.113435

Vo, D., Duong, N. H., Rungamornrat, J., & Nanakorn, P. (2022). A 2D field-consistent beam element for large displacement analysis using a rational Bézier representation with varying weights. *Applied Mathematical Modelling*, 104, 806-825. https://doi.org/10.1016/j.apm.2021.12.022

Vo, D., Li, X., Nanakorn, P., & Bui, T. Q. (2021). An efficient isogeometric beam formulation for analysis of 2D non-prismatic beams. *European Journal of Mechanics - A/Solids*, 89, 104280. https://doi.org/10.1016/j.euromechsol.2021.104280

Vo, D., Li, X., Nanakorn, P., & Bui, T. Q. (2021). An efficient isogeometric beam formulation for analysis of 2D non-prismatic beams. *European Journal of Mechanics-A/Solids*, 89, 104280. https://doi.org/10.1016/j.euromechsol.2021.104280

Vo, D., & Nanakorn, P. (2019). Large displacement analysis of pinned-fixed circular arches with different rise-to-span ratios using an isogeometric approach. *Proceeding of The 16th East Asian-Pacific Conference on Structural Engineering and Construction* (pp. 951-960). Brisbane, Australia: Springer.

Vo, D., & Nanakorn, P. (2020). Geometrically nonlinear multi-patch isogeometric analysis of planar curved Euler–Bernoulli beams. *Computer Methods in Applied Mechanics and Engineering*, 366, 113078. https://doi.org/10.1016/j.cma.2020.113078

Vo, D., & Nanakorn, P. (2020). A total Lagrangian Timoshenko beam formulation for geometrically nonlinear isogeometric analysis of planar curved beams. *Acta Mechanica*, 231(7), 2827-2847. https://doi.org/10.1007/s00707-020-02675-x

Vo, D., Nanakorn, P., & Bui, T. Q. (2019). Multi-patch geometrically nonlinear isogeometric analysis of spatial beams with additive rotation updates. *Proceeding of International Conference on Sustainable Civil Engineering and Architecture* (pp. 1129-1136). Springer.

Vo, D., Nanakorn, P., & Bui, T. Q. (2020). Multi-patch geometrically nonlinear isogeometric analysis of spatial beams with additive rotation updates. Reddy, J. N., Wang, C. M., Luong, V. H., & Le, A. T., *Proceeding of ICSCEA 2019* (pp. 1129-1136). Singapore: Springer Singapore.

Vo, D., Nanakorn, P., & Bui, T. Q. (2020). A total Lagrangian Timoshenko beam formulation for geometrically nonlinear isogeometric analysis of spatial beam structures. *Acta Mechanica*, 231(9), 3673-3701. https://doi.org/10.1007/s00707-020-02723-6

Vo, D., Nanakorn, P., & Bui, T. Q. (2021). Geometrically nonlinear multi-patch isogeometric analysis of spatial Euler–Bernoulli beam structures. *Computer Methods in Applied Mechanics and Engineering*, 380, 113808. https://doi.org/10.1016/j.cma.2021.113808

Vo, D., Nanakorn, P., Bui, T. Q., & Rungamornrat, J. (2022). Locking-free isogeometric Timoshenko-Ehrenfest beam formulations for geometrically nonlinear analysis of planar beam structures. *Mechanics of Advanced Materials and Structures*, 1-22. https://doi.org/10.1080/15376494.2022.2114044

Voruganti, H., & Gondegaon, S. (2016). Comparative study of isogeometric analysis with finite element analysis. *In Proceeding of International Conference on Recent Trends in Engineering, Science and Technology*. Hyderabad, India.

Wall, W. A., Frenzel, M. A., & Cyron, C. (2008). Isogeometric structural shape optimization. *Computer Methods in Applied Mechanics and Engineering*, 197(33-40), 2976-2988. https://doi.org/10.1016/j.cma.2008.01.025

Wang, C. M. (1995). Timoshenko beam-bending solutions in terms of Euler-Bernoulli solutions. *Journal of Engineering Mechanics*, 121(6), 763-765. https://doi.org/10.1061/(ASCE)0733-9399(1995)121:6(763)

Warren, J., & Weimer, H. (2001). *Subdivision methods for geometric design: A constructive approach*. Elsevier.

Weeger, O., Yeung, S.-K., & Dunn, M. L. (2017). Isogeometric collocation methods for Cosserat rods and rod structures. *Computer Methods in Applied Mechanics and Engineering*, 316, 100-122. https://doi.org/10.1016/j.cma.2016.05.009

Weeger, O., Yeung, S.-K., & Dunn, M. L. (2018). Fully isogeometric modeling and analysis of nonlinear 3D beams with spatially varying geometric and material parameters. *Computer Methods in Applied Mechanics and Engineering*, 342, 95-115. https://doi.org/10.1016/j.cma.2018.07.033

Zhang, Y., Zhu, C.-G., & Guo, Q.-J. (2017). On the limits of non-uniform rational B-spline surfaces with varying weights. *Advances in Mechanical Engineering*, 9(5), 1-16. https://doi.org/10.1177/1687814017700547

APPENDICES

APPENDIX A

The demonstration for the expression of tensor $\mathbf{L}$ in Equation (5.5)

From Equations (4.11) and (5.4), it gives as

$$
\begin{aligned}
\boldsymbol{\Lambda}^{\mathrm{T}}(\theta)\mathbf{F} &= \left(\frac{\mathbf{G}_1}{G_1} \otimes \frac{\mathbf{g}_1^*}{G_1} + \mathbf{G}_2 \otimes \mathbf{g}_2\right)(\mathbf{g}_1 \otimes \mathbf{G}^1 + \mathbf{g}_2 \otimes \mathbf{G}^2) \\
&= \left(\frac{\mathbf{G}_1}{G_1} \otimes \frac{\mathbf{g}_1^*}{G_1}\right)(\mathbf{g}_1 \otimes \mathbf{G}^1) + \left(\frac{\mathbf{G}_1}{G_1} \otimes \frac{\mathbf{g}_1^*}{G_1}\right)(\mathbf{g}_2 \otimes \mathbf{G}^2) + (\mathbf{G}_2 \otimes \mathbf{g}_2)(\mathbf{g}_1 \otimes \mathbf{G}^1) \\
&\qquad + (\mathbf{G}_2 \otimes \mathbf{g}_2)(\mathbf{g}_2 \otimes \mathbf{G}^2) \\
&= \frac{\mathbf{g}_1^* \cdot \mathbf{g}_1}{(G_1)^2}\mathbf{G}_1 \otimes \mathbf{G}^1 + \frac{\mathbf{g}_1^* \cdot \mathbf{g}_2}{(G_1)^2}\mathbf{G}_1 \otimes \mathbf{G}^2 + (\mathbf{g}_1 \cdot \mathbf{g}_2)\mathbf{G}_2 \otimes \mathbf{G}^1 + (\mathbf{g}_2 \cdot \mathbf{g}_2)\mathbf{G}_2 \otimes \mathbf{G}^2.
\end{aligned}
\tag{6.1}
$$

Recall Equation (4.9) to obtain the relations as $\mathbf{G}^1 = \mathbf{G}_1/(G_1)^2$ and $\mathbf{G}^2 = \mathbf{G}_2$. In addition, $\mathbf{g}_1^* \cdot \mathbf{g}_2 = 0$, $\mathbf{g}_1 \cdot \mathbf{g}_2 = \mathbf{a}_1 \cdot \mathbf{a}_2$, and $\mathbf{g}_2 \cdot \mathbf{g}_2 = 1$ since $\mathbf{g}_2$ is a unit vector. Consequently,

$$
\begin{aligned}
&\boldsymbol{\Lambda}^{\mathrm{T}}(\theta)\mathbf{F} = \\
&= \frac{\mathbf{g}_1^* \cdot \mathbf{g}_1}{(G_1)^2}\mathbf{G}_1 \otimes \mathbf{G}^1 + \frac{\mathbf{g}_1^* \cdot \mathbf{g}_2}{(G_1)^2}\mathbf{G}_1 \otimes \mathbf{G}^2 + (\mathbf{g}_1 \cdot \mathbf{g}_2)\mathbf{G}_2 \otimes \mathbf{G}^1 + (\mathbf{g}_2 \cdot \mathbf{g}_2)\mathbf{G}_2 \otimes \mathbf{G}^2 \\
&= (\mathbf{g}_1^* \cdot \mathbf{g}_1)\mathbf{G}^1 \otimes \mathbf{G}^1 + (\mathbf{g}_1^* \cdot \mathbf{g}_2)\mathbf{G}^1 \otimes \mathbf{G}^2 + (\mathbf{g}_1 \cdot \mathbf{g}_2)\mathbf{G}^2 \otimes \mathbf{G}^1 + (\mathbf{g}_2 \cdot \mathbf{g}_2)\mathbf{G}^2 \otimes \mathbf{G}^2 \\
&= (\mathbf{g}_1^* \cdot \mathbf{g}_1)\mathbf{G}^1 \otimes \mathbf{G}^1 + (\mathbf{a}_1 \cdot \mathbf{a}_2)\mathbf{G}^2 \otimes \mathbf{G}^1 + \mathbf{G}^2 \otimes \mathbf{G}^2.
\end{aligned}
\tag{6.2}
$$

Utilizing Equations (6.2) and (4.12) yields

$$
\begin{aligned}
\mathbf{L} = \boldsymbol{\Lambda}^{\mathrm{T}}(\theta)\mathbf{F} - \mathbf{G} &= (\mathbf{g}_1^* \cdot \mathbf{g}_1)\mathbf{G}^1 \otimes \mathbf{G}^1 + (\mathbf{a}_1 \cdot \mathbf{a}_2)\mathbf{G}^2 \otimes \mathbf{G}^1 + \mathbf{G}^2 \otimes \mathbf{G}^2 \\
&\qquad - (\mathbf{G}_1 \cdot \mathbf{G}_1)\mathbf{G}^1 \otimes \mathbf{G}^1 - \mathbf{G}^2 \otimes \mathbf{G}^2 \\
&= (\mathbf{g}_1^* \cdot \mathbf{g}_1 - (G_1)^2)\mathbf{G}^1 \otimes \mathbf{G}^1 + (\mathbf{a}_1 \cdot \mathbf{a}_2)\mathbf{G}^2 \otimes \mathbf{G}^1.
\end{aligned}
\tag{6.3}
$$

APPENDIX B

Explicit expression of the quadratic term of $\mathbf{L}$

From the expression of tensor $\mathbf{L}$ in Equation (5.9), it follows as

$$
\begin{aligned}
\mathbf{L}^{\mathrm{T}}\mathbf{L} = {} & \big[\big(\mathbf{a}_1 \cdot\ \mathbf{a}_1^* - 1 - T(\mathbf{A}_1 \cdot \mathbf{A}_2' - \mathbf{a}_1^* \cdot \mathbf{a}_2')\big)\mathbf{G}^1 \otimes \mathbf{G}^1 + (\mathbf{a}_1 \cdot \mathbf{a}_2)\mathbf{G}^1 \\
& \otimes \mathbf{G}^2\big]\big[\big(\mathbf{a}_1 \cdot\ \mathbf{a}_1^* - 1 - T(\mathbf{A}_1 \cdot \mathbf{A}_2' - \mathbf{a}_1^* \cdot \mathbf{a}_2')\big)\mathbf{G}^1 \otimes \mathbf{G}^1 \\
& + (\mathbf{a}_1 \cdot \mathbf{a}_2)\mathbf{G}^2 \otimes \mathbf{G}^1\big] \\
= {} & \Big(\big(\mathbf{a}_1 \cdot\ \mathbf{a}_1^* - 1 - T(\mathbf{A}_1 \cdot \mathbf{A}_2' - \mathbf{a}_1^* \cdot \mathbf{a}_2')\big)\mathbf{G}^1 \\
& \otimes \mathbf{G}^1\Big)\Big(\big(\mathbf{a}_1 \cdot\ \mathbf{a}_1^* - 1 - T(\mathbf{A}_1 \cdot \mathbf{A}_2' - \mathbf{a}_1^* \cdot \mathbf{a}_2')\big)\mathbf{G}^1 \otimes \mathbf{G}^1\Big) \\
& + \Big(\big(\mathbf{a}_1 \cdot\ \mathbf{a}_1^* - 1 - T(\mathbf{A}_1 \cdot \mathbf{A}_2' - \mathbf{a}_1^* \cdot \mathbf{a}_2')\big)\mathbf{G}^1 \otimes \mathbf{G}^1\Big)(\mathbf{a}_1 \cdot \mathbf{a}_2)\mathbf{G}^2 \otimes \mathbf{G}^1 \\
& + \big((\mathbf{a}_1 \cdot \mathbf{a}_2)\mathbf{G}^1 \otimes \mathbf{G}^2\big)\Big(\big(\mathbf{a}_1 \cdot\ \mathbf{a}_1^* - 1 - T(\mathbf{A}_1 \cdot \mathbf{A}_2' - \mathbf{a}_1^* \cdot \mathbf{a}_2')\big)\mathbf{G}^1 \otimes \mathbf{G}^1\Big) \\
& + \big((\mathbf{a}_1 \cdot \mathbf{a}_2)\mathbf{G}^1 \otimes \mathbf{G}^2\big)\big((\mathbf{a}_1 \cdot \mathbf{a}_2)\mathbf{G}^2 \otimes \mathbf{G}^1\big) \\
= {} & (I) + (II) + (III) + (IV).
\end{aligned}
\tag{6.4}
$$

The above equation consists of four terms, i.e.,

$$(I) = \big(\mathbf{a}_1 \cdot\ \mathbf{a}_1^* - 1 - T(\mathbf{A}_1 \cdot \mathbf{A}_2' - \mathbf{a}_1^* \cdot \mathbf{a}_2')\big)^2(\mathbf{G}^1 \cdot \mathbf{G}^1)\mathbf{G}^1 \otimes \mathbf{G}^1 \tag{6.5}$$

$$(II) = \big(\mathbf{a}_1 \cdot\ \mathbf{a}_1^* - 1 - T(\mathbf{A}_1 \cdot \mathbf{A}_2' - \mathbf{a}_1^* \cdot \mathbf{a}_2')\big)(\mathbf{a}_1 \cdot \mathbf{a}_2)(\mathbf{G}^1 \cdot \mathbf{G}^2)\mathbf{G}^1 \otimes \mathbf{G}^1 = 0 \tag{6.6}$$

$$(III) = (\mathbf{a}_1 \cdot \mathbf{a}_2)\big(\mathbf{a}_1 \cdot\ \mathbf{a}_1^* - 1 - T(\mathbf{A}_1 \cdot \mathbf{A}_2' - \mathbf{a}_1^* \cdot \mathbf{a}_2')\big)(\mathbf{G}^2 \cdot \mathbf{G}^1)\mathbf{G}^1 \otimes \mathbf{G}^1 = 0 \tag{6.7}$$

$$(IV) = (\mathbf{a}_1 \cdot \mathbf{a}_2)^2(\mathbf{G}^2 \cdot \mathbf{G}^2)\mathbf{G}^1 \otimes \mathbf{G}^1 = (\mathbf{a}_1 \cdot \mathbf{a}_2)^{\mathbf{2}}\mathbf{G}^1 \otimes \mathbf{G}^1. \tag{6.8}$$

Note that

$$\mathbf{G}^1 \cdot \mathbf{G}^2 = \mathbf{G}^2 \cdot \mathbf{G}^1 = 0 \qquad\qquad \mathbf{G}^2 \cdot \mathbf{G}^2 = 1. \tag{6.9}$$

Recall that $(\mathbf{a}_1 \cdot \mathbf{a}_1^* - 1)$, $T(\mathbf{A}_1 \cdot \mathbf{A}_2' - \mathbf{a}_1^* \cdot \mathbf{a}_2')$, and $(\mathbf{a}_1 \cdot \mathbf{a}_2)$ are small under small-strain assumption. Consequently, the higher-order terms $\left(\mathbf{a}_1 \cdot \mathbf{a}_1^* - 1 - T(\mathbf{A}_1 \cdot \mathbf{A}_2' - \mathbf{a}_1^* \cdot \mathbf{a}_2')\right)^2$ in (I) and $(\mathbf{a}_1 \cdot \mathbf{a}_2)^2$ in (IV) are sufficiently small and negligible. As a result, $\mathbf{L}^{\mathrm{T}}\mathbf{L}$ in Equation (4.16) is discarded.

BIOGRAPHY

Name:	Mr. Nghi Huu Duong
Education:	2016: Bachelor of Engineering (Civil Engineering), Ho Chi Minh City University of Technology (HCMUT), Vietnam
	2020: Master of Science (Engineering and Technology), Sirindhorn International Institute of Technology, Thammasat University, Thailand

Publications:

Duong, N. H., Vo, D., Matsumoto, T., & Nanakorn, P. (2025). A locking-free Timoshenko-Ehrenfest planar straight beam element for geometrically nonlinear analysis using rational Bézier representations with varying weights. *Mathematics and Mechanics of Solids.* https://doi.org/10.1177/10812865241303088

Duong, N. H., Nanakorn, P., & Matsumoto, T. (2023). Different weight-related interpolation schemes for isogeometric analysis of geometrically nonlinear beams. *Proceeding of the 26th Symposium on Applied Mechanics (22007-12-02).* Tokyo, Japan.

Duong, N. H., Vo, D., Matsumoto, T., & Nanakorn, P. (2023). Isogeometric analysis of planar curved Euler-Bernoulli beams having large displacements and small strains. *Proceeding of the Hokkaido Branch - Japan Society of Civil Engineers 2023 Annual Meeting, 79 (A-34).* Hokkaido, Japan.

Duong, N. H., Vo, D., & Nanakorn, P. (2022). Geometrically nonlinear behavior of L-Shaped frames under forces applied at different positions. *Proceeding of the 17th East Asian-Pacific Conference on Structural Engineering and Construction (pp. 837-842).* Singapore: Springer.

Duong, N. H., Vo, D., & Nanakorn, P. (2019). Design of two-dimensional trusses by an improved firefly algorithm. *Proceeding of the 12th Pacific Structural Steel Conference.* Tokyo, Japan.

Duong, N. H. (2019). Truss topology optimization by a statistical firefly algorithm. *Sirinhorn International Institute of Technology, Thammasat University.* Thailand.

Vo, D., Duong, N. H., Rungamornrat, J., & Nanakorn, P. (2022). A 2D field-consistent beam element for large displacement analysis using a rational Bézier representation with varying weights. *Applied Mathematical Modelling, 104, 806-825.* https://doi.org/10.1016/j.apm.2021.12.022

Afifah, R. A., Khaliq, N., Duong, N. H., Vo, D., & Nanakorn, P. (2024). Determination of Bending Rigidities of Beams Using Physics-Informed Neural Networks. *Proceeding of the 18th East Asian-Pacific Conference on Structural Engineering and Construction*. Chiang Mai, Thailand.

Presentation:

Duong, N. H. (2022). Isogeometric analysis of beams undergoing large deformations. *Presentation at AUN/SEED-Net CEP Joint Graduate Research Seminar in Civil Engineering: Sustainable Technologies for a Responsible Growth*. Phnom Penh, Cambodia.